

https://dspace.org/

Searches for scalar resonances using diphotons in association with leptons with the ATLAS detector at the LHC

Makgetha, Kutlwano Chongo

2026

University of the Witwatersrand, Johannesburg

https://hdl.handle.net/10539/50283

Makgetha, Kutlwano Chongo. (2026). Searches for scalar resonances using diphotons in association with leptons with the ATLAS detector at the LHC [Master's dissertation, University of the Witwatersrand, Johannesburg]. WIReDSpace. https://hdl.handle.net/10539/50283

Downloaded from a DSpace repository. https://dspace.org/

Searches for scalar resonances using diphotons in association with leptons with the ATLAS detector at the LHC

Kutlwano Chongo Makgetha

Supervisor:
Prof. Bruce Mellado
Co-supervisor:
Dr. Mukesh Kumar



WITS
UNIVERSITY

A dissertation submitted to the Faculty of Science, University of the Witwatersrand, Johannesburg, in fulfillment of the requirements for the degree of:
Master of Science in Physics
26 January 2026

Declaration

I, Kutlwano Chongo Makgetha, declare that this dissertation is my original work, and that all sources have been properly acknowledged and cited according to the Faculty of Science's guidelines at the University of the Witwatersrand, Johannesburg.



Kutlwano Chongo Makgetha

26 January 2026

Abstract

In the first project, we examine recent studies that have identified growing excesses in scalar resonances with diphoton ($\gamma\gamma$) final states at the Large Hadron Collider (LHC). These results suggest the presence of scalar particles beyond the Standard Model (BSM), motivated by multi-lepton anomalies observed in Run 2 data from the ATLAS and CMS experiments. Phenomenological studies of the Higgs spectrum sidebands have indicated the presence of a new scalar S with a mass of 152 ± 1 GeV, originating from a heavier scalar H, with a global significance of 5.3σ. ATLAS has launched a new analysis using the `easyjet` analysis framework with Run 3 data. This analysis searches for scalar resonances produced via $\gamma\gamma$ channels in association with leptons, inspired by the Two-Higgs Doublet with a Singlet (2HDM+S) and triplet models. Given the complexity of the signal, we carefully account for the dominant background processes, including $\gamma\gamma$ + multijets, $V\gamma\gamma$ and $t\bar{t}\gamma\gamma$ production. The study uses Monte Carlo (MC) samples corresponding to the 2022 ATLAS Run 3 data, with an integrated luminosity of 35.7 fb^{-1} at $\sqrt{s} = 13.6$ TeV. The objective is to provide a comprehensive analysis of the significance of this channel, to develop and implement advanced multivariate analysis techniques including deep neural networks, and to contribute to the understanding of potential new scalar particles and their implications for physics beyond the SM.

In the second project, we build upon the ATLAS and CMS discovery of the Higgs boson (h) decaying into a Z boson and a photon (γ), a rare process within SM that occurs at next-to-leading order (NLO) with a 3.4σ significance. Even with NLO quantum chromodynamics (QCD) corrections and signal-background interference, SM predictions exceed the observed signal rate by $2.2\sigma \pm 0.7$, indicating possible new physics effects or systematic uncertainties that validate further investigation. We investigate this rare process using machine learning (ML) techniques. We use the XGBoost classifier to analyse the production modes of the $h \to Z\gamma$ process, particularly the gluon-gluon fusion (ggF). We use the kernel density estimation (KDE) technique to visualise and

compare the probability density functions of the classification scores for the generated signal and background events. This provides insights into their separation and overlap within the framework of the Standard Model Effective Field Theory (SMEFT). We aim to constrain the six-dimensional Wilson coefficients and shed light on potential deviations from SM prediction. These methodological innovations demonstrate the effective integration of advanced ML techniques in precision Higgs physics and BSM searches.

Keywords: ATLAS, Large Hadron Collider, scalar resonances, diphoton final states, Higgs boson, machine learning, Deep neural networks, XGBoost, kernel density estimation, SMEFT, physics beyond the Standard Model.

Acknowledgements

I acknowledge the financial support of the National Research Foundation (iThemba LABS) through the SA-CERN Excellence Bursary for this research. The opinions and conclusions expressed are solely those of the author and do not necessarily reflect the views of the National Research Foundation (iThemba LABS).

I thank my supervisor, Prof. Bruce Mellado, for his exceptional guidance, support, and encouragement throughout my research. His insights, feedback, and dedication to excellence were instrumental in shaping my work and enabling my academic achievements.

I am thankful to the Institute for Collider Particle Physics (ICPP) members for their invaluable knowledge, resources, and opportunities, which have been crucial for my research pursuits. I appreciate Dr. Mukesh Kumar, Dr. Rachid Mazini, Dr. Phuti Rapheeha, and Dr. Srimoy Bhattacharya for their thoughtful discussions, insightful feedback, and valuable suggestions, which significantly enhanced the quality of this dissertation.

I extend my heartfelt appreciation to my friends and family, whose emotional support and encouragement have been a source of strength throughout the challenges and triumphs of this journey, giving me the self-belief to overcome adversity. A special thanks goes to my best friend, Ms. Andile Ndlovu, for her encouragement and belief in my potential, which motivated me to persevere.

Furthermore, I wish to acknowledge the contributions of everyone who generously shared their time to make this study possible. Their cooperation and engagement were essential to the success of this research.

To everyone who has contributed to this journey in countless ways, thank you for your support and encouragement.

Publications

Conferences:

1. **Kutlwano Makgetha**, Njokweni Mbuyiswa, Srimoy Bhattacharya, Abduluazem Fadol, Nidhi Tripati, Mukesh Kumar and Bruce Mellado. The use of Machine Learning techniques to analyse the gg $\rightarrow$ h $\rightarrow$ Zγ process within the SMEFT framework at the Large Hadron Collider (LHC), in The Proceedings of SAIP2024, the 68th Annual Conference of the South African Institute of Physics pp. 341 – 346. ISBN: 978-1-0370-2645-4.
   Available online at: https://events.saip.org.za/event/246/attachments/3748/5416/SAIP%202024%20Proceedings%20978-1-0370-2645-4.pdf.

2. **Kutlwano Makgetha**, Njokweni Mbuyiswa, Srimoy Bhattacharya, Abduluazem Fadol, Mukesh Kumar and Bruce Mellado. The use of Machine Learning techniques to analyse the gg $\rightarrow$ h $\rightarrow$ Zγ process within the SMEFT framework at the Large Hadron Collider (LHC), in The Proceedings of SAIP2025, the 69th Annual Conference of the South African Institute of Physics - Submitted and accepted.

3. **Kutlwano Makgetha**, Vuyolwethu Kakancu, Njokweni Mbuyiswa, Kgothatso Ntumbe, Paballo Ndhlovu, Phuti Rapheeha, Reda Mekouar, Rachid Mazini, Mukesh Kumar and Bruce Mellado. Searches for scalar resonances with diphoton in association with leptons and taus using the `easyjet` analysis framework in ATLAS detector at the LHC, in The Proceedings of SAIP2025, the 69th Annual Conference of the South African Institute of Physics - Submitted and accepted.

4. Njokweni Mbuyiswa, **Kutlwano Makgetha**, Srimoy Bhattacharya, Abdualazem Fadol, Katlego Machete, Mukesh Kumar and Bruce Mellado. Analysing $gg \rightarrow h \rightarrow Z\gamma$ decay at the LHC using SMEFT, in The Proceedings of SAIP2025, the

69th Annual Conference of the South African Institute of Physics - Submitted and accepted.

5. Kgothatso Ntumbe, Baballo-Victor Ndhlovu, **Kutlwano Makgetha**, Njokweni Mbuyiswa, Vuyolwethu Kakancu, Thabo Pilusa, Phuti Rapheeha, Reda Mekouar, Rachid Mazini, Mukesh Kumar and Bruce Mellado. Prepating for Diphoton Resonance Searches in the Leptonic, 0-τ Final States: Event Selection and Background Characterization Using ATLAS Run Data, in The Proceedings of SAIP2025, the 69th Annual Conference of the South African Institute of Physics - Submitted and accepted.

6. Njokweni Mbuyiswa, **Kutlwano Makgetha**, Vuyolwethu Kakancu, Paballo Ndhlovu, Kgothatso Ntumbe, Reda Mekouar, Phuti Rapheeha, Mukesh Kumar, Rachid Mazini and Bruce Mellado. Monte Carlo Generation Involving Searches for Diphoton Resonances in Association with $\tau^+\tau^-$ or b-jets at the Electroweak Scale in the ATLAS Detector at the LHC, in The Proceedings of SAIP2025, the 69th Annual Conference of the South African Institute of Physics - Submitted and accepted.

Contents

Declaration i

Abstract ii

Acknowledgments iv

Publications v

List of Figures x

List of Tables xiii

List of Symbols xv

List of Abbreviations xvii

1 The Standard Model of Particle Physics and Beyond 1

1.1 Introduction . . . 1
1.2 Fundamental Particles and Interactions . . . 2
1.2.1 Elementary SM Particle Content . . . 3
1.2.2 Gauge transformations and Quantum Electrodynamics . . . 6
1.2.3 Quantum Chromodynamics . . . 8
1.3 Higgs Boson . . . 9
1.3.1 Higgs Boson Production . . . 10
1.3.2 Decay Modes of the Higgs Boson . . . 10
1.4 The Shortcomings of the Standard Model . . . 12
1.5 Multi-lepton anomalies at the LHC . . . 14
1.5.1 The Simplified Model . . . 14
1.5.2 The 2HDM+S Model . . . 16
1.5.3 The Multi-lepton Anomalies . . . 18

1.5.4 The 152 GeV Scalar Candidate . . . 19
1.5.5 The Triplet Model . . . 22

2 The Large Hadron Collider and the ATLAS Experiment 25
2.1 The Large Hadron Collider . . . 25
2.2 The ATLAS Experiment . . . 28
2.2.1 The Inner Detector . . . 31
2.2.2 The Calorimeter System . . . 32
2.2.3 Muon Spectrometer . . . 34
2.2.4 Forward Detectors . . . 36
2.2.5 The ATLAS Magnetic System . . . 37
2.2.6 Trigger System . . . 38

3 Object Reconstruction 41
3.1 Photons and Electrons . . . 41
3.2 Hadronically decaying taus . . . 42
3.3 Muons . . . 43
3.4 Jets and b-jets . . . 43
3.5 Missing Transverse Momentum . . . 44

4 Diphoton studies in association with leptons 45
4.1 Data samples . . . 45
4.1.1 Signal Sample . . . 45
4.1.2 MC Background Samples . . . 47
4.1.3 Overlap removal . . . 48
4.1.4 Object Selection . . . 48
4.2 Multivariate Analysis Strategies . . . 50
4.3 Estimation of Statistical Significance . . . 52

5 Constraining SMEFT Wilson Coefficients in the $h \to Z\gamma$ decay at the LHC 55
5.1 Model independent analysis in SMEFT . . . 56
5.2 Signal and Background Simulation . . . 58
5.3 Constraining SMEFT Wilson Coefficients . . . 59
5.4 Signal and Background Discrimination using Machine Learning . . . 62

6 Summary and Outlook **67**
6.1 Summary 67
6.2 Future Work 68

A Diphoton studies in association with leptons **70**
A.1 MC Event Weighting 70
A.2 Correlation Matrices 71
A.3 Input Features for DNN 72

B Applications of Machine Learning Techniques in $h \to Z\gamma$ **74**
B.1 Cross-sections and weights 74
B.2 Feature Importance and Correlation Matrices 75
B.3 XGboost training and Normalised Distributions 81

Bibliography **85**

List of Figures

1.1 Schematic representation of SM, illustrating the fundamental particles. The first three columns correspond to the three fermion generations, followed by a column depicting the gauge bosons responsible for mediating fundamental interactions, while the final entry denotes the Higgs boson. The illustration also includes the hypothetical graviton, a BSM particle postulated as the carrier of the gravitational interaction [28]. . 4
1.2 Feynman diagrams for the production of the SM Higgs boson at leading order via: (a) ggF, (b) VBF, (c) VH and (d) $t\bar{t}H$ [39]. 11
1.3 An overview of the chronological development of the multi-lepton anomalies, which ultimately led to the prediction of a narrow resonance with a mass of $m_S = 150 \pm 5$ GeV. The figure also contains a table summarising the corresponding final states, their main features, the dominant SM backgrounds, and the respective significances of the observed anomalies [14]. 19
1.4 The p-values of the individual channels, together with their combined result and the corresponding local significance, are presented. The best-fit value is found at 152 GeV, corresponding to a global (local) significance of 5.33σ (5.6σ). 21

2.1 Sketch of CERN accelerator complex in 2022. Light (dark) grey arrows indicate the typical flight direction of protons (heavy ions) through the complex [87]. 26
2.2 The mean number of interactions per bunch crossing for $\sqrt{s} = 13.6$ TeV pp collisions data from 2022–2024, weighted by luminosity [88]. 27
2.3 The layout of the ATLAS Experiment [90]. 29
2.4 Sketch of the coordinate system used in ATLAS [91]. 30
2.5 The Inner Detector of the ATLAS experiment [90]. 32

2.6 Cut away sketch of the ATLAS Calorimeter [90]. 34
2.7 Cut away sketch of the ATLAS Muon system [90]. 36
2.8 The ATLAS magnet configuration, displaying the central solenoid together with the barrel and end-cap toroids. 38
2.9 The ATLAS Trigger Systems with its interfaces to the detector and readout systems [90]. 40

4.1 The $H \to SS'$ decay Feynman diagram, H $[250-400]$, S $[150-270]$ and S' $[95-125]$ GeV. 46
4.2 Event Filtering Histogram for $\gamma\gamma\tau^+\tau^-$ signal. Total Filter Efficiency = 0.187. 47
4.3 DNN response for the $\gamma\gamma + 0\ell 1\tau_{\text{had}}$ channel. 53
4.4 DNN response for the $\gamma\gamma + 1\ell 1\tau_{\text{had}}$ channel. 53
4.5 ROC curves for the $\gamma\gamma + 1\ell 1\tau_{\text{had}}$ (left) and $\gamma\gamma + 0\ell 1\tau_{\text{had}}$ (right) channels. 54

5.1 Feynman diagrams for the $h \to Z\gamma$ decay [75]. 56
5.2 Two-dimensional 95% CL contours for the Wilson coefficients $C_{\phi W}$, $C_{\phi WB}$, and $C_{\phi B}$ obtained from the $\ell\ell\gamma$ channel using the dominant observable p_T^{γ}. The red regions correspond to the inclusive analysis, while the blue regions represent the multi-bin approach. 60
5.3 Two-dimensional 95% CL contours for the Wilson coefficients $C_{\phi W}$, $C_{\phi WB}$, and $C_{\phi B}$ obtained from the $jj\gamma$ channel using the dominant observable p_T^{γ}. The red regions correspond to the inclusive analysis, while the blue regions represent the multi-bin approach. 61
5.4 Two-dimensional 95% CL contours for the Wilson coefficients $C_{\phi W}$, $C_{\phi WB}$, and $C_{\phi B}$ obtained from the $\nu\bar{\nu}\gamma$ channel using the dominant observable $m_T^{(\gamma,\text{MET})}$. The red regions correspond to the inclusive analysis, while the blue regions represent the multi-bin approach. 62
5.5 Comparison of the ROC Curve with its associated AUC score (left), and a KDE plot with XGBoost classification score (right) for the ggF production ($jj\gamma$) channel. 64
5.6 Comparison of the ROC Curve with its associated AUC score (left), XGBoost classification score (right) for ggF production ($\nu\bar{\nu}\gamma$) channel. . 64

5.7 Comparison of the ROC Curve with its associated AUC score (left), and a KDE plot with XGBoost classification score (right) for the ggF production ($\ell^+\ell^-\gamma$) channel. 65

A.1 Signal and Background correlation matrices for the $\gamma\gamma + 1\ell 1\tau_{\text{had}}$ channel. 71
A.2 Signal and Background correlation matrices for the $\gamma\gamma + 0\ell 1\tau_{\text{had}}$ channel. 72
A.3 Normalised distributions of key kinematic observables used in the $\gamma\gamma + 0\ell 1\tau_{\text{had}}$ channel. 73
A.4 Normalised distributions of key kinematic observables used in the $\gamma\gamma + 1\ell 1\tau_{\text{had}}$ channel. 73

B.1 Feature importance for ggF production ($\ell^+\ell^-\gamma$) channel. 78
B.2 Feature importance for ggF production ($jj\gamma$) channel. 79
B.3 Feature importance for ggF production ($\nu\bar{\nu}\gamma$) channel. 79
B.4 Signal and Background correlation matrix of the ggF production ($\nu\bar{\nu}\gamma$) channel. 80
B.5 Signal and Background correlation matrix of the ggF production ($jj\gamma$) channel. 80
B.6 Signal and Background correlation matrix of the ggF production ($\ell^+\ell^-\gamma$) channel. 81
B.7 Normalised distributions of key kinematic observables used in the ggF production ($\ell^+\ell^-\gamma$) channel to distinguish signal from background events. 82
B.8 Normalised distributions of key kinematic observables used in the ggF production ($jj\gamma$) channel to distinguish signal from background events. 83
B.9 Normalised distributions of key kinematic observables used in the ggF production ($\nu\bar{\nu}\gamma$) channel to distinguish signal from background events. 84

List of Tables

1.1 Summary of the gauge boson properties in SM. J^P indicates the particle's spin J and parity P. The listed force strengths of the vector bosons are given relative to the strong interaction and should be regarded as order-of-magnitude estimates, not fixed ratios. These approximate values (e.g, $\sim 10^{-3}$ for electromagnetism and $\sim 10^{-8}$ for the weak force) depend on the energy scale and the coupling constants α. The value for gravity ($\sim 10^{-37}$) makes it weaker than the weak interaction. Values are taken from [29]. 5
1.2 Cross-section summary for primary Higgs productions at $\sqrt{s} = 13$ TeV [29, 40]. 12
1.3 Summary of the branching ratios of the Higgs boson decay channels [29, 42]. 12
1.4 List of final states predicted by the simplified model used to interpret the corresponding experimental results. The initial combination performed in 2021 incorporated all channels belonging to Group 1. The subsequent combination in 2023 extended to include channels from both Groups 1 and 2. The most recent combination in 2025 includes all channels from Groups 1, 2, and 3. 21

4.1 Summary of the simulation parameters for different scalar masses and cross-sections for the $\gamma\gamma\tau^+\tau^-$ signal. 46
4.2 The photon and tau Filters used in event pre-selection for the signal. . 47
4.3 Number of events generated for the $V\gamma\gamma$, $\gamma\gamma t\bar{t}$, and $\gamma\gamma +$ multijets background samples. 48
4.4 The $\gamma\gamma + 1\ell 1\tau_{\text{had}}$ channel event selection for $\gamma\gamma t\bar{t}$, $\gamma\gamma +$ multijets, $V\gamma\gamma$ background and the $\gamma\gamma\tau^+\tau^-$ signal samples. 49

4.5 The $\gamma\gamma + 0\ell 1\tau_{\text{had}}$ channel event selection for $\gamma\gamma t\bar{t}$, $\gamma\gamma$ + multijets, $V\gamma\gamma$ background and the $\gamma\gamma\tau^+\tau^-$ signal samples. 50
4.6 Input variables used for DNN training in the $\gamma\gamma + 1\ell 1\tau_{\text{had}}$ and $\gamma\gamma + 0\ell 1\tau_{\text{had}}$ channels. 51
4.7 The separation power of DNN variables for the $\gamma\gamma + 1\ell 1\tau_{\text{had}}$ and $\gamma\gamma + 0\ell 1\tau_{\text{had}}$ channels. 52
4.8 Weighted signal and background yields after event selection and DNN response cut for the $\gamma\gamma + 1\ell 1\tau_{\text{had}}$ channel. 53
4.9 Weighted signal and background yields after event selection and DNN response cut for the $\gamma\gamma + 0\ell 1\tau_{\text{had}}$ channel. 54

5.1 The ggF production mode and its corresponding signal and background processes. 59
5.2 Summary of object selections for the three ggF channels. 63
5.3 The Z-scores for ggF production channels obtained using binned likelihoods with different binning choices, compared with the MLL+KDE approach. 66

B.1 Cross-section results for ggF production channels and their uncertainties. 75
B.2 Event counts, weights, and weighted event yields are summarised for the leptonic, jet and neutrino channels, with selection criteria detailed in Table 5.2. 75
B.3 Variables used as inputs to the XGBoost, with respect to Ref. [132] in $\ell^+\ell^-\gamma$ channel. 76
B.4 Variables used as XGboost inputs in $jj\gamma$ channel. 77
B.5 Variables used as XGboost inputs in $\nu\bar{\nu}\gamma$ channel. 78

List of Symbols

j	Jet
l	Lepton
p	Proton
t	Top quark
W	W Boson
Z	Z Boson
γ	Photon
S	152 GeV Scalar
S'	95 GeV Scalar
H	Heavy Scalar
R	Radius Parameter
m	Mass
η	Pseudorapidity
ϕ	Azimuthal angle
p_T	Transverse Momentum
$\sqrt{s}$	Center of Mass Energy
$\mathcal{L}$	Instantaneous Luminosity
fb^{-1}	Inverse femtobarn
λ	Lambda
δ	Delta
τ	Tau
x, y	Spatial coordinates
E_T	Transverse energy
E_T^{miss}	Missing Transverse energy
Q	Electric charge
u	Up quark
d	Down quark
c	Charm quark
s	Strange quark
t	Top quark
b	Bottom quark
e^-	Electron
e^+	positron
μ	Muon

ν	Neutrino
p	proton
h	Higgs boson

List of Abbreviations

2HDM	Two Higgs Doublet Model
ALFA	Absolute Luminosity For ATLAS
ALICE	A Large Ion Collider Experiment
ATLAS	A Toroidal LHC ApparatuS
AUC	Area Under the Curve
BDT	Boosted Decision Trees
BEH	Brout Englert Higgs
BSM	Beyond the Standard Model
CERN	European Organization for Nuclear Research
CL	Confidence Level
CMS	Compact Muon Solenoid
CP	Charge Parity
CSC	Cathode Strip Chambers
DNN	Deep Neural Networks
ECAL	Electromagnetic Calorimeter
ECT	End Cap Toroid
EF	Event Filter
EM	Electro Magnetic
EMB	Electro Magnetic Barrel
EMEC	Electro Magnetic End Cap
FCAL	Forward Calorimeter
FCNC	Flavour Changing Neutral Currents
HCAL	Hadronic Calorimeter
HECAL	Hadronic End Cap Calorimeter
HL-LHC	High Luminosity-LHC
HLT	High-Level Trigger
IBL	Insertable B-Layer
ID	Inner Detector
ICPP	Institute for Collider Particle Physics
KDE	Kernel Density Estimation
LAr	Liquid Argon
LEP	Large Electron Positron collider
LHC	Large Hadron Collider
LHCb	Large Hadron Collider beauty

LB	Long Barrel
LINAC	Linear Accelerator
LO	Leading Order
LUCID	Luminosity Cerenkov Integrating Detector
LS	Long Shutdown
MBTS	Minimum Bias Trigger Scintillators
MC	Monte Carlo
MCMC	Markov Chain Monte Carlo
MDT	Monitored Drift Tube Chambers
ML	Machine Learning
MLL	Machine-Learned Likelihood
MS	Muon Spectrometer
NLO	Next to Leading Order
NSW	New Small Wheel
PDGID	Particle Data Group identification number
Pflow	Particle Flow
PS	Proton Synchrotron
QCD	Quantum Chromodynamics
QED	Quantum Electrodynamics
QFT	Quantum Field Theory
RF	Radio Frequency
RHT	Real Higgs Triplet
ROI	Regions of Interest
ROC	Receiver Operating Characteristic curve
RPC	Resistive Plate Chambers
SCT	Semi Conductor Tracker
SM	Standard Model
SMEFT	Standard Model Effective Field Theory
SPS	Super Proton Synchrotron
SR	Signal Region
SUSY	Supersymmetry
TDAQ	Trigger Data AcQuisition
TGC	Thin Gap Chambers
TileCal	Tile Calorimeter
TRT	Transition Radiation Tracker
VEV	Vacuum Expection Value
WLS	Wavelength Shifting
WP	Working Point
ZDC	Zero-Degree Calorimeter

Chapter 1

The Standard Model of Particle Physics and Beyond

1.1 Introduction

Particle physics constitutes the study of the fundamental constituents of matter and the interactions that govern their behaviour at subatomic scales. Its primary objective is to elucidate the underlying structure of the universe, spanning from elementary particles to the fundamental forces that shape cosmic phenomena, with the Standard Model (SM) [1] providing the prevailing theoretical framework. A crowning achievement of the SM was the discovery of the Higgs boson (h) [2–4] in 2012 by the ATLAS [5] and CMS Collaborations [6] at the European Organization for Nuclear Research (CERN). This discovery completed the predicted spectrum of particles within the SM, marking a significant milestone in our understanding of particle physics. However, despite its remarkable success, the SM is not without its limitations. Experimental observations have shown deviations from its predictions, raising the possibility that there is more to the subatomic world than what the SM can account for. These include its inability to incorporate gravity and explain the evidence for non-baryonic dark matter.

The quest for answers has resulted in several theoretical frameworks, including supersymmetry (SUSY), extra spatial dimensions, and various dark matter candidates. Collectively, these theories seek to overcome the limitations of the SM and enhance our understanding of beyond the Standard Model (BSM) physics, sparking significant theoretical and experimental efforts in this field.

Within this broader context, multi-lepton anomalies have emerged as intriguing indications of potential new physics. They are statistically significant deviations from SM predictions in final states containing multiple leptons, missing transverse energy and possibly b-jets [7–14]. These anomalies predict the presence of a resonant scalar with a mass of 150 ± 5 GeV [8] and Refs. [15–17] found excesses in the sidebands of SM Higgs searches from ATLAS and CMS experiments [18–25]. These results suggest the presence of a resonance at 152 ± 1 GeV [26] with a global significance of 5.3σ [17]. Motivated by these results, this dissertation focuses on the study of Run 3 data since the 5σ observation was made using Run 2 data to explore the possible existence of such a scalar resonance.

In the coming years, the Large Hadron Collider (LHC) [27] at CERN is set to undergo substantial upgrades. These upgrades will enable the LHC to produce proton-proton (pp) collisions at higher energies and luminosities than ever before. This enhanced performance will significantly improve the data processing capabilities and elevate the precision of current and future physics measurements, paving the way for new discoveries in particle physics.

This dissertation is divided into five chapters. It begins with chapter 1, which introduces the SM and examines the study of multi-lepton anomalies. This is followed by chapter 2, which describes the ATLAS detector and its integration within the LHC environment. An overview of the object selections used in this study is provided in chapter 3. The first project, presented in chapter 4, focuses on diphoton studies in association with leptons and taus. The second project, discussed in chapter 5, presents an in-depth analysis involving Machine Learning (ML) techniques within the framework of the Standard Model Effective Field Theory (SMEFT). Finally, chapter 6 summarises the two studies, highlighting the key findings and broader implications of this work.

1.2 Fundamental Particles and Interactions

The SM provides a unified theoretical description of the known elementary particles and their interactions. It is formulated as a relativistic quantum field theory (QFT)

based on the gauge symmetry group $SU(3)_C \times SU(2)_L \times U(1)_Y$. This structure incorporates the strong, weak, and electromagnetic forces, each associated with its own set of gauge bosons. The photon mediates electromagnetic interactions; eight gluons, which carry color-anticolor combinations and are self-interacting, are responsible for the strong interaction, while the $W^{\pm}$ and Z bosons govern the weak force, shown in Figure 1.1.

This chapter provides a concise summary of the SM, its limitations and potential extensions. The SM's particles and interactions are described in subsection 1.2.1. The Higgs boson production and decay modes are outlined in subsection 1.3.1 and subsection 1.3.2. The shortcomings of the SM are explained in section 1.4, with section section 1.5 detailing multi-lepton anomalies at the LHC and sections subsection 1.5.1 and subsection 1.5.5 highlighting the simplified and triplet models as potential explanations of BSM phenomena.

1.2.1 Elementary SM Particle Content

Elementary particles are classified as either fermions, named after Enrico Fermi, or bosons, named after Satyendranath Bose, based on their spin quantum numbers. Fermions have half-integer spins and obey Fermi-Dirac statistics, while bosons have integer spins and obey Bose-Einstein statistics. According to the Pauli exclusion principle, fermions cannot occupy the same quantum state, whereas multiple bosons can. As a result, fermions constitute matter particles, while bosons act as force carriers. Fermions are grouped into leptons and quarks based on their interaction characteristics. The charged leptons: the electron ($e^{\pm}$), muon ($\mu^{\pm}$), and tau ($\tau^{\pm}$) each have an associated neutral partner: ν_e, ν_μ and ν_τ, respectively. Electrons and muons are stable within the LHC detectors, while tau leptons decay before they reach the detector. The tau lepton can decay into an electron or a muon, accompanied by their corresponding antineutrino, or into one or two pions.

In the minimal SM, neutrinos are treated as massless, non-decaying particles that interact only via the weak force. This was a valid assumption, but the observation of neutrino oscillations confirms that neutrinos have small, nonzero masses, requiring extensions of the SM such as the see-saw mechanism to account for them. The quarks

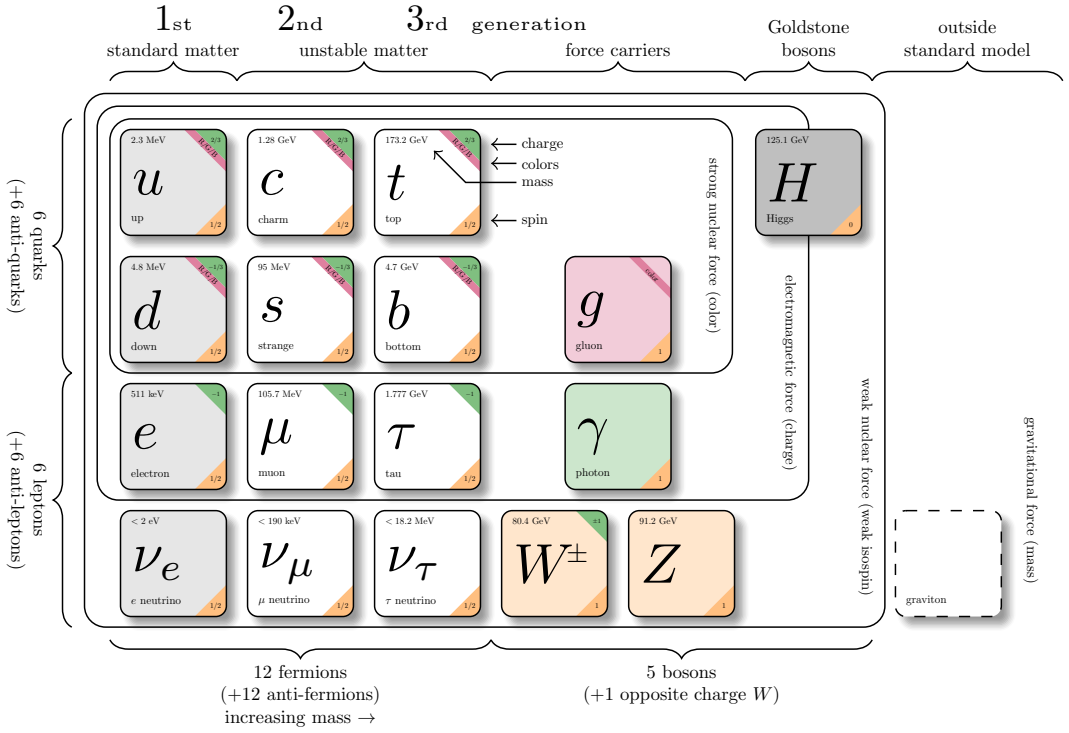


FIGURE 1.1: Schematic representation of SM, illustrating the fundamental particles. The first three columns correspond to the three fermion generations, followed by a column depicting the gauge bosons responsible for mediating fundamental interactions, while the final entry denotes the Higgs boson. The illustration also includes the hypothetical graviton, a BSM particle postulated as the carrier of the gravitational interaction [28].

carry a color charge and are the only fermions that participate in the strong interaction. They can carry one of three color charges: red, blue, or green, while antiquarks carry the corresponding anti-color charges. A combination of red, blue and green quarks, or a colored quark and its anti-colored quark, results in a color-neutral particle. Gluons carry both color and anti-color charges and mediate the strong interaction between quarks. Each fermion has a corresponding antiparticle, which is identical to the specific fermion except for opposite charge. Quarks are confined within hadrons, forming bound states with integral electric charge, whereas leptons occur as free elementary particles in nature (see subsection 1.2.3).

Force	Strength	Boson	J^P	Charge [e]	Mass [GeV]
Strong	1	Gluon ($\times 8$)	1^-	0	0
EM	$\sim 10^{-3}$	Photon (γ)	1^-	0	0
Weak	$\sim 10^{-8}$	$W^{\pm}$	1^-	± 1	80.4
		Z	1^-	0	91.2
		H	0^+	0	125.1

TABLE 1.1: Summary of the gauge boson properties in SM. J^P indicates the particle's spin J and parity P. The listed force strengths of the vector bosons are given relative to the strong interaction and should be regarded as order-of-magnitude estimates, not fixed ratios. These approximate values (e.g, $\sim 10^{-3}$ for electromagnetism and $\sim 10^{-8}$ for the weak force) depend on the energy scale and the coupling constants α. The value for gravity ($\sim 10^{-37}$) makes it weaker than the weak interaction. Values are taken from [29].

The electroweak interaction combines the weak and electromagnetic forces under gauge symmetry $SU(2)_L \times U(1)_Y$. In this framework, the subscript L signifies that the weak force acts exclusively on left-handed particles, which transform as doublets under the $SU(2)_L$ gauge symmetry. In contrast, right-handed fermions are singlets under $SU(2)_L$, hence not participate in weak interactions mediated by the $W^{\pm}$ and Z bosons. They interact only through the $U(1)_Y$ gauge symmetry, carrying weak hypercharge but no weak isospin. The symbol Y represents the weak hypercharge, which should not be confused with the Gell-Mann–Nishijima hypercharge (the latter differing by a factor of two). The weak hypercharge is defined through the fundamental relation: $Q = T^3 + \frac{1}{2}Y$, with Q electric charge operator and T^3 third term of weak isospin. A summary of all properties of the bosons in the SM and their associated forces is shown in Table 1.1.

The complete SM Lagrangian, incorporating the Higgs, gauge, fermionic and Yukawa sectors, is expressed as Equation 1.2.1:

$$\mathcal{L}_{SM} = \mathcal{L}_H + \mathcal{L}_G + \mathcal{L}_F + \mathcal{L}_Y, \tag{1.2.1}$$

where the components in Equation 1.2.1 can be written in full:

$$\mathcal{L}_{SM} = |D_\mu \phi|^2 - V(\phi) - \frac{1}{4} F_{\mu\nu} F^{\mu\nu} + i\bar{\psi} D\psi + h.c + \bar{\psi}^i y^{ij} \psi^j \phi + h.c. \tag{1.2.2}$$

The Higgs boson interactions are represented by the notation $\mathcal{L}_H$. In addition, the kinetic energies of the gauge fields are indicated by $\mathcal{L}_G$. For the fermion couplings, we use the notation $\mathcal{L}_F$, while the Yukawa couplings are denoted by $\mathcal{L}_Y$. Together, these various components form a crucial part of the SM Lagrangian. Equation 1.2.2 describes this Lagrangian. It is important to note that this Lagrangian is invariant under the gauge symmetry, which is expressed as the product of three groups: $U(1)_Y$, $SU(2)_L$ and $SU(3)_C$. The gauge symmetry group serves as the foundation for the SM Lagrangian. The $SU(3)_C$ symmetry group brings about the formation of gluons responsible for conveying the strong nuclear force. The $SU(2)_L$ symmetry group generates three gauge fields, W^1_μ, W^2_μ, and W^3_μ, while the $U(1)_Y$ group contributes the gauge field B_μ. After electroweak symmetry breaking, these fields mix to form the physical weak bosons W^+, W^-, and Z, which mediate the weak nuclear force, and the photon A_μ, associated with electromagnetism. The one notable absent force in nature is gravity, which is not included in the SM. This invariance is a fundamental feature that ensures consistency in the theoretical framework describing particle interactions.

1.2.2 Gauge transformations and Quantum Electrodynamics

Having introduced the particle content and gauge symmetry of the SM in subsection 1.2.1, we now turn to Quantum Electrodynamics (QED), the simplest case, to illustrate how gauge invariance dictates interaction structure. The QFT of electromagnetism serves as the archetype of Abelian gauge theories, and this subsection explores the mathematical structure underlying QED, namely, its foundation in local $U(1)_Y$ gauge invariance. The dynamics of spin-$\frac{1}{2}$ fermions are governed by the Dirac equation. The corresponding free-field Lagrangian density is:

$$\mathcal{L}_D = i\overline{\psi}\not{\partial}\psi - m\overline{\psi}\psi, \tag{1.2.3}$$

where $\psi(x)$ is the Dirac spinor field describing the fermion, $\overline{\psi} = \psi^\dagger\gamma^0$ is its Dirac adjoint, and m is the fermion's mass. The notation $\not{\partial} = \gamma^\mu\partial_\mu$ uses the Feynman slash convention, with $\partial_\mu = \partial/\partial x^\mu$ the spacetime derivative and γ^μ ($\mu = 0, 1, 2, 3$) the 4×4 gamma matrices, which satisfy the Clifford algebra $\{\gamma^\mu, \gamma^\nu\} = 2g^{\mu\nu}\mathbb{I}$; here $g^{\mu\nu} = \text{diag}(+1, -1, -1, -1)$ is the Minkowski metric and $\mathbb{I}$ the 4×4 identity matrix. This Lagrangian is invariant under global $U(1)_Y$ phase transformations $\psi(x) \to e^{iq\alpha}\psi(x)$, where q is a real constant interpreted as the particle's electric charge (in units of the

elementary charge e) and α is a spacetime-independent real parameter. By Noether's theorem, this symmetry implies conservation of electric charge. However, demanding invariance under local transformations $\psi(x) \to e^{iq\alpha(x)}\psi(x)$, with $\alpha(x)$ an arbitrary real function of spacetime, is essential for consistency with relativity and locality. Under such a transformation, the derivative term $\partial_\mu\psi$ acquires an extra contribution proportional to $\partial_\mu\alpha(x)$, which breaks invariance and necessitates the introduction of a real vector field $A_\mu(x)$, the electromagnetic four-potential, replacing the ordinary derivative with the covariant derivative:

$$D_\mu = \partial_\mu + iqA_\mu. \tag{1.2.4}$$

The gauge field $A_\mu(x)$ must transform as $A_\mu \to A_\mu - \partial_\mu\alpha(x)$ to cancel the unwanted term, ensuring the Lagrangian remains invariant. This procedure naturally introduces the photon as a massless, spin-1 gauge boson, the quantum excitation of the field A_μ. The complete QED Lagrangian is then:

$$\mathcal{L}_{\text{QED}} = i\overline{\psi}\not{D}\psi - m\overline{\psi}\psi - \frac{1}{4}F_{\mu\nu}F^{\mu\nu}, \tag{1.2.5}$$

where $\not{D} = \gamma^\mu D_\mu = \gamma^\mu(\partial_\mu + iqA_\mu)$ and $F_{\mu\nu} = \partial_\mu A_\nu - \partial_\nu A_\mu$ is the electromagnetic field tensor. The contraction $F^{\mu\nu} = g^{\mu\alpha}g^{\nu\beta}F_{\alpha\beta}$ ensures Lorentz invariance of the kinetic term for the photon field. Expanding the first term yields an interaction of the form $q\,\overline{\psi}\gamma^\mu\psi A_\mu$, where the coupling constant q, often denoted g_e or simply e for the electron, is identified with the particle's electric charge.

What distinguishes QED from non-Abelian gauge theories such as Quantum Chromo-Dynamics (QCD) or the electroweak sector is its simplicity: the $U(1)_Y$ gauge group is Abelian, so the photon is neutral and does not self-interact. Moreover, electric charges are not fixed by representation theory; they are free parameters that must be measured experimentally. In contrast, non-Abelian symmetries like $SU(2)_L$ or $SU(3)_C$ impose rigid relationships among couplings due to the non-commuting nature of their generators and the resulting self-interactions of their gauge bosons. Moreover, while QED appears as a standalone theory, it is actually embedded within the larger SM Lagrangian $\mathcal{L}_{SM}$ (Equation 1.2.2) as the unbroken $U(1)_{\text{EM}}$ subgroup that remains after spontaneous symmetry breaking of the electroweak gauge group $SU(2)_L \times U(1)_Y$.

Thus, QED is not merely a phenomenological description of electromagnetic interactions; it is the low-energy remnant of a deeper, unified gauge-invariant structure that unifies electromagnetism with the weak force.

This subsection reinforces a central theme of modern particle physics: "gauge symmetry dictates interaction structure". QED, as the simplest and most precisely tested gauge theory, provides the blueprint for understanding more complex forces in nature.

1.2.3 Quantum Chromodynamics

Having introduced quarks and gluons in subsection 1.2.1, we now turn to the underlying gauge theory of the strong interaction, QCD. Unlike QED, QCD is a non-Abelian gauge theory based on local $SU(3)_C$ symmetry, where the subscript C denotes color charge. This non-Abelian structure is encoded in eight massless gluon fields G^a_μ ($a = 1, \ldots, 8$), each associated with a generator $T_a = \frac{1}{2}\lambda_a$ of the $SU(3)_C$ Lie algebra, where λ_a are the Gell-Mann matrices and the structure constants f^{abc} defined by the commutation relations $[T_a, T_b] = if^{abc}T_c$ govern triple and quartic gluon vertices. The dynamics of quark fields q_i (with flavour index $i = 1, 2, 3$, color index and mass m_q) and gluons are governed by the QCD Lagrangian density:

$$\mathcal{L}_{\text{QCD}} = \bar{q}_i \left\{ i\gamma^\mu \left(D_\mu\right)_{ij} - m_q \delta_{ij} \right\} q_j - \frac{1}{4} G^a_{\mu\nu} G^{\mu\nu}_a, \tag{1.2.6}$$

where the covariant derivative $\left(D_\mu\right)_{ij} = \partial_\mu \delta_{ij} - ig_s (T_a)_{ij} G^a_\mu$ ensures local gauge invariance via the strong coupling constant g_s, and the gluon field strength tensor:

$$G^a_{\mu\nu} = \partial_\mu G^a_\nu - \partial_\nu G^a_\mu + g_s f^{abc} G^b_\mu G^c_\nu \tag{1.2.7}$$

contains a nonlinear term proportional to f^{abc} that directly reflects gluon self-interactions. As a consequence, the running coupling $g_s(\mu)$ is large at low energy scales (of order unity below $\sim 100\,\text{GeV}$), rendering perturbative methods ineffective in this regime. Yet, it becomes small at high momentum transfers, a property known as asymptotic freedom, enabling first-principles calculations in deep-inelastic scattering and jet production at the LHC. Conversely, at low energies, the strong interaction confines color-charged particles, quarks and gluons cannot exist as free asymptotic states but are permanently bound into color-singlet composite particles called hadrons. Quarks

achieve color neutrality in two primary ways: by forming quark–antiquark pairs known as mesons (with integer spin: 0 or ± 1), or by combining three quarks (or three antiquarks) with complementary color charges into baryons (with half-integer spin: $\pm\frac{1}{2}$ or $\pm\frac{3}{2}$); familiar examples include the proton (uud) and neutron (udd). This phenomenon, color confinement, arises non-perturbatively from the formation of a chromoelectric flux tube between separating quarks, whose energy grows linearly with distance until it becomes energetically favorable to produce a new $q\bar{q}$ pair, leading to hadronisation, where partons form observable jets of hadrons in collider experiments. Moreover, QCD Lagrangian admits topological θ:

$$\mathcal{L}_\theta = \theta \frac{g_s^2}{32\pi^2} \mathrm{Tr}(G_{\mu\nu}\tilde{G}^{\mu\nu}), \tag{1.2.8}$$

where $\tilde{G}^{\mu\nu} = \frac{1}{2}\epsilon^{\mu\nu\rho\sigma}G^a_{\rho\sigma}$ is the dual gluon field strength tensor and θ is a dimensionless parameter. Although this term vanishes for perturbative field configurations that decay at infinity, it contributes in topologically non-trivial sectors, such as instantons, and violates Charge Parity (CP) symmetry, potentially generating a measurable neutron electric dipole moment. The physical value of θ is constrained to be extremely small ($|\theta| < 10^{-10}$), a puzzle known as the strong CP problem. The θ-term is periodic under $\theta \to \theta + 2\pi n$ for integer n, and while a chiral rotation of massless quarks could in principle eliminate θ, the presence of quark masses in the SM ties θ to the complex phase of the quark mass matrix, rendering it a physical, observable parameter highlighting the deep interplay between symmetry, topology and phenomenology in QCD.

1.3 Higgs Boson

Hypothesised in 1964, discovered in 2012 at CERN by the ATLAS [30] and CMS [31] Collaborations. The Higgs boson the final particle predicted by the SM. The Higgs boson is a neutral scalar particle that explains how particles, such as fermions, $W^\pm$, and Z bosons, acquire mass through the Brout-Englert-Higgs (BEH) mechanism [32–34], and its properties remain consistent with the SM's predictions.

The BEH mechanism generates mass for fermions (quarks and leptons) through their interaction with the Higgs field, which emerges via spontaneous symmetry breaking.

However, the mass of everyday objects, such as protons and neutrons, is predominantly due to the binding energy of quarks and gluons, described by QCD. In popular culture, the Higgs boson is often referred to as the "God particle." This term originated when Leon Lederman humorously called it the "Goddamn Particle," which was later shortened [35].

As the only scalar boson (a particle with zero spin) in SM, it was introduced to reconcile the massless photon, responsible for the long-range electromagnetic force, with the massive W/Z bosons that mediate short-range weak force. This theoretical framework was developed independently by Peter Higgs [36, 37], François Englert, Robert Brout [32], Gerald Guralnik, Carl Hagen and Tom Kibble [33], drawing inspiration from the Anderson [38] mechanism for superconductivity.

1.3.1 Higgs Boson Production

The SM Higgs boson is produced through several mechanisms at the LHC, varying with the initial-state particles and center-of-mass ($\sqrt{s}$) energy. The four main production modes, shown in Figure 1.2, are gluon-gluon fusion (ggF), vector boson fusion (VBF), Higgs Strahlung (VH, where $V = W, Z$) and associated production with top quarks ($t\bar{t}H$).

Gluon-gluon fusion is the most dominant mode, driven by a high cross-section (σ) (see Table 1.2) from top quark loops that exploit the top quark's large mass. However, contributions from other quark loops are greatly suppressed. Vector boson fusion ranks second, producing a Higgs boson through quark scattering mediated by vector bosons. Higgs Strahlung, represented as $q\bar{q} \to ZH$ or WH, involves the production of a Higgs boson with a W or Z boson. Lastly, the $t\bar{t}H$ process generates a Higgs boson alongside a pair of top quarks, which is essential for examining the top Yukawa coupling. These mechanisms highlight the diverse interactions of the Higgs boson with gauge bosons and fermions in SM.

1.3.2 Decay Modes of the Higgs Boson

The Higgs boson, an unstable particle with an extremely short lifetime of $O(10^{-22})$ s, decays predominantly into fermions or gauge bosons. Its decay mechanisms and

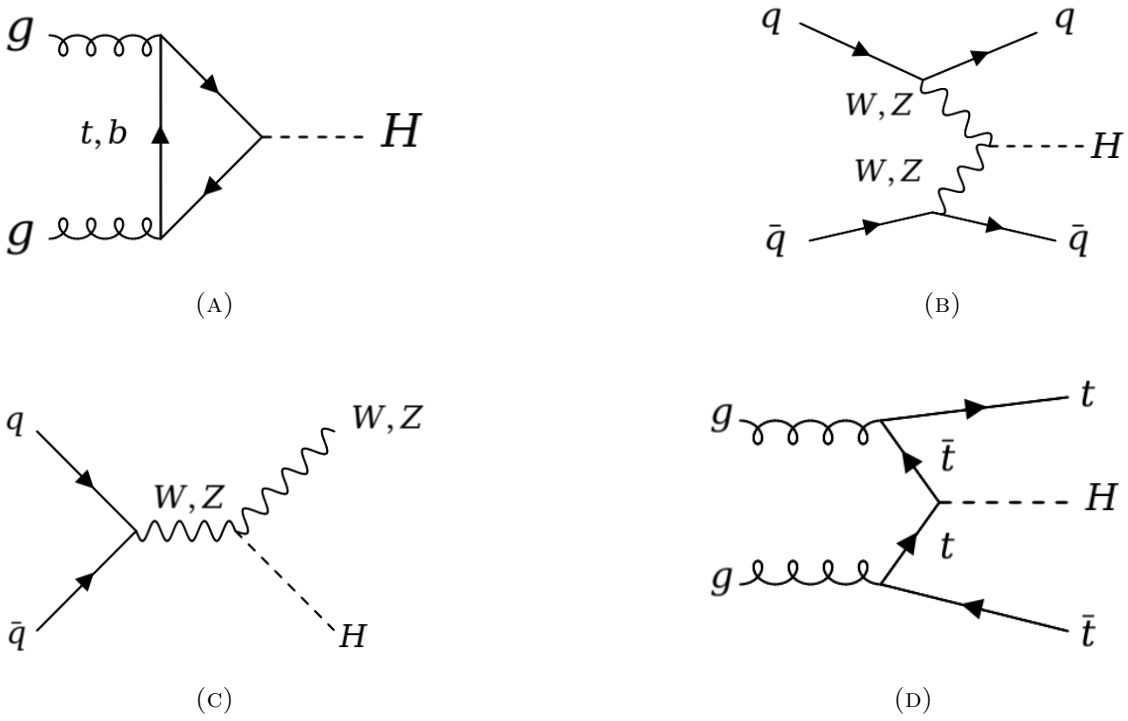


FIGURE 1.2: Feynman diagrams for the production of the SM Higgs boson at leading order via: (a) ggF, (b) VBF, (c) VH and (d) $t\bar{t}H$ [39].

branching ratios are governed by both the strength of its couplings and the kinematics of the final states. The leading decay modes are illustrated in Table 1.3. Even though the top quark having the strongest coupling to the Higgs boson, the decay $h \to t\bar{t}$ is kinematically forbidden when $m_h < 2m_t$, as it violates energy-momentum conservation. Instead, the Higgs boson predominantly decays into a $b\bar{b}$ pair, with a branching ratio of $\mathrm{Br}(h \to b\bar{b}) = 58.2 \pm 0.7\%$. This is followed by $\mathrm{Br}(h \to W^+W^-) = 21.4 \pm 0.3\%$. The third-most dominant decay channel is into gluons via top quark loops, yielding $\mathrm{Br}(h \to gg) = 8.53 \pm 0.85\%$.

Decays into off-shell gauge bosons, such as $h \to ZZ^*$, also play a significant role. These decays occur with branching ratios of $\mathrm{Br}(h \to ZZ^*) = 2.9\%$ and $\mathrm{Br}(h \to WW^*) = 22.1\%$, leading to final states like $h \to ZZ^* \to 4\ell$. Rare decays into photons and gluons are mediated by virtual particles (W bosons and top quarks), with $\mathrm{Br}(h \to \gamma\gamma) = 0.22\%$ and $\mathrm{Br}(h \to gg) = 8.5\%$, respectively [29, 41].

Production Mode	**Process**	σ @ 13 TeV pb
ggF	$(gg \to H)$	48.60 ± 2.40
VBF	$(qq' \to Hqq')$	3.78 ± 0.08
WH	$(qq' \to WH)$	1.37 ± 0.03
ZH	$(qq/gg \to ZH)$	0.88 ± 0.04
$t\bar{t}H$	$(qq/gg \to t\bar{t}H)$	0.51 ± 0.05
bbH	$(qq/gg \to bbH)$	0.49 ± 0.12
tH	$(qq/gg \to tH)$	0.09 ± 0.01
Total		55.10 ± 3.30

TABLE 1.2: Cross-section summary for primary Higgs productions at $\sqrt{s} = 13$ TeV [29, 40].

Decay Channel	**Br [%]**
$h \to b\bar{b}$	58.20 ± 0.70
$h \to WW^*$	21.40 ± 0.30
$h \to gg$	8.57 ± 0.85
$h \to \tau\tau$	6.27 ± 0.10
$h \to c\bar{c}$	2.89 ± 0.24
$h \to ZZ^*$	2.62 ± 0.04
$h \to \gamma\gamma$	0.23 ± 0.01
$h \to Z\gamma$	0.15 ± 0.01
$h \to \mu\mu$	0.02 ± 0.001

TABLE 1.3: Summary of the branching ratios of the Higgs boson decay channels [29, 42].

1.4 The Shortcomings of the Standard Model

Despite its tremendous success in describing fundamental particles and their interactions, the SM has several limitations. One key limitation lies in the mass hierarchies and parameters: the SM contains 24 free parameters, such as particle masses and couplings which must be experimentally determined rather than theoretically predicted. It fails to explain why particles have their observed masses, why there are three generations of fermions with increasing masses, and the hierarchy problem, which arises from the large difference between the electroweak scale and the Planck scale. This issue stems from the quadratic sensitivity of the Higgs boson mass to high-energy

corrections, meaning that maintaining its observed value requires an unnatural degree of fine-tuning. In other words, quantum corrections tend to drive the Higgs mass toward the cutoff scale, making the stability of the electroweak scale appear highly unnatural without additional theoretical mechanisms such as supersymmetry or other forms of new physics. Additionally, the SM does not incorporate gravity, since general relativity, which is our best theory of gravity, is fundamentally incompatible with the framework of QFT. Attempts to quantise gravity result in non-renormalisable theories, producing uncontrollable infinities that cannot be removed without introducing infinitely many parameters, making them unpredictable, leaving gravity unexplained within the SM.

Another limitation of the SM arises from its failure to incorporate dark matter and dark energy, which together constitute roughly 27% and 68% of the universe's total mass–energy content, respectively. These components are essential for understanding phenomena such as the universe's accelerated expansion and galactic rotation curves [43, 44]. The SM also cannot account for the observed matter-antimatter asymmetry in the universe. It incorporates CP violation but remains insufficient to account for the baryon asymmetry observed today [45]. Furthermore, the SM fails to achieve a Grand Unified Theory that unifies the strong, weak and electromagnetic forces, nor does it unify all fundamental forces at high energy scales. This limitation is not an internal inconsistency but rather an expected feature of the SM, as such unification would require embedding its gauge group $SU(3)_C \times SU(2)_L \times U(1)_Y$ into a larger, more symmetric gauge structure such as $SU(5)$ or $SO(10)$. These extended frameworks aim to combine the three gauge couplings at a single unification scale, offering a more comprehensive description of the fundamental forces.
The properties of neutrinos pose another challenge for the SM. Neutrino oscillations have demonstrated that neutrinos have mass, contrary to SM's original assumption of massless neutrinos [46–48]. The potential existence of sterile neutrinos lies beyond the SM's scope. Another issue is aesthetic and fine-tuning problems, such as the little hierarchy problem, which involves the apparent fine-tuning required to stabilise the Higgs boson mass. The inability of the SM to predict key parameters raises questions about its completeness as a fundamental theory.
Efforts to address these shortcomings include exploring BSM physics. SUSY, for example, proposes the existence of superpartners for every SM particle, offering solutions to

the hierarchy problem and a viable candidate for dark matter [49]. Despite these challenges, the SM remains a cornerstone of modern physics, providing a strong framework that guides ongoing efforts to explore new physics beyond its boundaries.

1.5 Multi-lepton anomalies at the LHC

The Higgs boson discovery completed the SM, however it also opened new avenues for exploration. Certain features and excesses observed in the LHC Run 1 data suggest potential deviations from SM predictions, hinting at the existence of additional scalar states. These findings motivate further investigation through precision measurements and searches for BSM physics. Such studies include measurements of the differential transverse momentum of the Higgs boson (p_{T}^{h}) [50–53], searches for di-Higgs boson resonances [54–57], $t\bar{t}H$ [58–61] and searches for resonances decaying into pairs of electroweak gauge bosons VV (where $V = Z, W^{\pm}$) [62–64].

1.5.1 The Simplified Model

To accommodate these excesses, a simplified model was formulated in 2015 [7], and its parameters were fixed in 2017 to avoid tuning to subsequent data; in particular, it predicted multi-lepton excesses that were later observed (already in Run 1 and with early Run 2 data) [8]. The model extends the SM by introducing a heavy scalar H and a lighter Higgs-like scalar S that couples to both H and h. To minimise free parameters, S is assumed to decay predominantly via $S \to W^{+}W^{-} \to \ell^{+}\ell^{-}\nu\bar{\nu}$ ($\ell = e, \mu$), while H decays almost exclusively as $H \to Sh$ with a 100% branching ratio. These anomalies, consistent across independent channels, motivated fixing the model parameters to $m_S = 150 \pm 5\,\mathrm{GeV}$ before the release of Run 2 results, in order to avoid fine-tuning and look-elsewhere biases. The model also predicted additional multi-lepton excesses in final states not originally used for its construction as a method of validation [11].

The total Lagrangian describing the simplified model that incorporates both H and S can be expressed as:

$$\mathcal{L} = \mathcal{L}_{\mathrm{SM}} + \mathcal{L}_{\mathrm{BSM}}, \tag{1.5.1}$$

where $\mathcal{L}_{\text{BSM}}$ contains all contributions from new physics, including additional interactions and particle state. This BSM component is further decomposed as:

$$\mathcal{L}_{\text{BSM}} = \mathcal{L}_H + \mathcal{L}_S. \tag{1.5.2}$$

The components of the Lagrangian are defined as follows:

$$\mathcal{L}_H = \frac{1}{2}\partial_\mu H \partial^\mu H - \frac{1}{2}m_H^2 H^2 + \mathcal{L}_G + \mathcal{L}_Y, \tag{1.5.3}$$

$$\mathcal{L}_G = -\frac{\beta_g k_{Hgg}^{\text{SM}}}{4} G^a_{\mu\nu} G^{a\mu\nu} H + \beta_V k_{hVV}^{\text{SM}} V_\mu V^\mu H, \tag{1.5.4}$$

$$\mathcal{L}_Y = -\frac{1}{\sqrt{2}}\left[y_{ttH}\bar{t}tH + y_{bbH}\bar{b}bH\right]. \tag{1.5.5}$$

The singlet scalar sector is expressed through the Lagrangian:

$$\mathcal{L}_S = \mathcal{L}_K + \mathcal{L}_{SVV} + \mathcal{L}_{Sf\bar{f}} + \mathcal{L}_{hHS}, \tag{1.5.6}$$

where the terms are defined as:

$$\mathcal{L}_K = -\frac{1}{2}\partial_\mu S \partial^\mu S - \frac{1}{2}m_S^2 S^2, \tag{1.5.7}$$

$$\begin{aligned}\mathcal{L}_{SVV} =& \frac{1}{4}k_{Sgg}\frac{\alpha_s}{12\pi v} S G^{a\mu\nu} G^a_{\mu\nu} + \frac{1}{4}k_{S\gamma\gamma}\frac{\alpha}{\pi v} S F_{\mu\nu} F^{\mu\nu} \\ &+ \frac{1}{4}k_{SZZ}\frac{\alpha}{\pi v} S Z_{\mu\nu} Z^{\mu\nu} + \frac{1}{4}k_{SZ\gamma}\frac{\alpha}{\pi v} S Z_{\mu\nu} F^{\mu\nu} \\ &+ \frac{1}{4}k_{SWW}\frac{\alpha}{\pi v} S W^{+\mu\nu} W^-_{\mu\nu},\end{aligned} \tag{1.5.8}$$

$$\mathcal{L}_{Sf\bar{f}} = -\sum_f K_{Sf}\frac{m_f}{v} S \bar{f} f, \tag{1.5.9}$$

$$\mathcal{L}_{HhS} = -\frac{1}{2}v\left[\lambda_{hhS} hhS + \lambda_{HHS} HHS + \lambda_{HSS} HSS + \lambda_{HhS} HhS\right]. \tag{1.5.10}$$

The neutral and charged weak bosons, Z and $W^\pm$, are collectively denoted by V, with their corresponding field-strength tensors expressed as $W^\pm_{\mu\nu} = D_\mu W^\pm_\nu - D_\nu W^\pm_\mu$,

where the covariant derivative is defined by $D_\mu W_\nu^\pm = [\partial_\mu \pm ieA_\mu]W_\nu^\pm$. In the gauge-field Lagrangian, $\mathcal{L}_G$, the first term describes the effective interaction between the gluons and the SM Higgs boson H, characterised by the coupling $k_{Hgg}^{\mathrm{SM}} = \alpha_s/(3\pi v)$ and modulated by the parameter β_g. Likewise, the term $\beta_V k_V^{\mathrm{SM}}$ in $\mathcal{L}_G$ corresponds to the Higgs coupling to vector bosons. The branching fraction for the process $H \to VV$ is governed by $k_V^{\mathrm{SM}} = m_V^2/v$. The Yukawa sector, represented by $\mathcal{L}_Y$, contains the top-quark Yukawa coupling in its first term, whereas the subsequent term encodes bottom-quark coupling. The decay $H \to b\bar{b}$, associated with the bottom Yukawa interaction y_{bbH}, is typically suppressed because bottom-quark production through ggF is relatively rare. Additionally, the decay channel $H \to Sh$ can yield final states comprising leptons, jets, photons and missing transverse energy (E_T^{miss}).

1.5.2 The 2HDM+S Model

This model allows for studies of S production and decay, and predicts nontrivial scalar interactions. An illustrative example is the process $gg \to H \to SS'$, where $S \to \gamma\gamma$ yields a $\gamma\gamma$ resonance, while S' produces lepton-rich final states. These signatures arise from the model's extended scalar sector and vacuum structure, distinguishing it from simpler SM extensions.

The particle spectrum of the 2HDM+S consists of three CP-even scalars, h, S', H and the singlet-like scalar S, one CP-odd scalar A, a charged Higgs boson $H^\pm$. Each state leads to characteristic experimental signals: $S \to \gamma\gamma$ generates the observed $\gamma\gamma$ excess, S' produces high-multiplicity lepton final states, and processes such as $H^\pm \to W^\pm S$ open additional discovery channels. The scalar potential extends the 2HDM by adding the singlet field φ_S, giving:

$$\begin{aligned} V(\varphi_1, \varphi_2, \varphi_S) = {} & m_{11}^2|\varphi_1|^2 + m_{22}^2|\varphi_2|^2 - m_{12}^2(\varphi_1^\dagger\varphi_2 + \text{h.c.}) \\ & + \frac{\lambda_1}{2}(\varphi_1^\dagger\varphi_1)^2 + \frac{\lambda_2}{2}(\varphi_2^\dagger\varphi_2)^2 + \lambda_3(\varphi_1^\dagger\varphi_1)(\varphi_2^\dagger\varphi_2) \\ & + \lambda_4(\varphi_1^\dagger\varphi_2)(\varphi_2^\dagger\varphi_1) + \frac{\lambda_5}{2}\left[(\varphi_1^\dagger\varphi_2)^2 + \text{h.c.}\right] \\ & + \frac{1}{2}m_S^2\varphi_S^2 + \frac{\lambda_6}{8}\varphi_S^4 + \frac{\lambda_7}{2}(\varphi_1^\dagger\varphi_1)\varphi_S^2 + \frac{\lambda_8}{2}(\varphi_2^\dagger\varphi_2)\varphi_S^2. \end{aligned} \tag{1.5.11}$$

The fields φ_1 and φ_2 correspond to the $SU(2)_L$ Higgs doublets, while φ_S denotes a real scalar singlet. The potential's first three components are associated with the

2HDM sector, whereas the last term introduces singlet-specific contributions. Flavour-changing neutral currents (FCNCs) are tree-level processes where a neutral Higgs boson mediates transitions between different fermion generations (e.g., $b \to s$), which are highly suppressed experimentally. To avoid such unwanted effects at tree level, a discrete Z_2 symmetry is imposed on the Higgs sector, under which $\varphi_1 \to +\varphi_1$ and $\varphi_2 \to -\varphi_2$. This symmetry is extended to the Yukawa sector, ensuring that each type of fermion couples with one of the two Higgs doublets. As a result, dangerous tree-level FCNCs are naturally forbidden. However, the Z_2 symmetry is allowed to be softly broken by the m_{12}^2 term, which introduces a bilinear coupling $\varphi_1^\dagger \varphi_2$ with dimensionful coefficient m_{12}^2, preserving the benefits of the symmetry at high energies while allowing for richer phenomenology. The singlet field φ_S, being a gauge singlet, does not couple directly to fermions and can acquire a vacuum expectation value (VEV) without affecting electroweak symmetry breaking dynamics. If an additional Z_2 symmetry (e.g., $\varphi_S \to -\varphi_S$) is imposed on the singlet, it remains stable and can serve as a viable dark matter candidate, provided it does not acquire a VEV and the symmetry remains unbroken.

We take $m_{12}^2 \neq 0$, corresponding to soft Z_2 breaking, and assume all λ_i are real (no explicit CP violation). Minimising the potential with $\varphi_1 \to v_1/\sqrt{2}$, $\varphi_2 \to v_2/\sqrt{2}$ and $\varphi_S \to v_S$ yields the conditions:

$$\frac{\partial V}{\partial [v_1, v_2, v_S]} = 0, \tag{1.5.12}$$

leading to

$$m_{11}^2 = -\frac{1}{2}\left(v_1^2\lambda_1 + v_2^2\lambda_{345} + v_S^2\lambda_7\right) + \frac{v_2}{v_1}m_{12}^2, \tag{1.5.13}$$

$$m_{22}^2 = -\frac{1}{2}\left(v_2^2\lambda_2 + v_1^2\lambda_{345} + v_S^2\lambda_8\right) + \frac{v_1}{v_2}m_{12}^2, \tag{1.5.14}$$

$$m_S^2 = -\frac{1}{2}\left(v_1^2\lambda_7 + v_2^2\lambda_8 + v_S^2\lambda_6\right), \tag{1.5.15}$$

where $\lambda_{345} = \lambda_3 + \lambda_4 + \lambda_5$.

The Yukawa interactions of the scalar mass eigenstates with SM fermions are:

$$-\mathcal{L}_{\text{Yukawa}}^{\text{2HDM+S}} = \sum_{f=u,d,\ell} \frac{m_f}{v}\left[y_f^h\, h\bar{f}f + y_f^H\, H\bar{f}f + y_f^S\, S\bar{f}f - i\, y_f^A\, A\bar{f}\gamma_5 f\right] + \sqrt{2}V_{ud}H^+\bar{u}\left(\frac{m_u}{v}y_u^A P_L + \frac{m_d}{v}y_d^A P_R\right) + \sqrt{2}\frac{m_\ell}{v}y_\ell^A\,\bar{\nu}P_R\ell + \text{h.c.} \tag{1.5.16}$$

Here, y_f^h, y_f^H, y_f^S and y_f^A are the normalised Yukawa couplings with the three CP-even scalars and the CP-odd pseudoscalar. The term proportional to γ_5 encodes pseudoscalar interactions, while the charged Higgs boson $H^\pm$ couples to quarks through the CKM matrix V_{ud} and to leptons via y_ℓ^A. Projection operators P_L and P_R isolate left and right-handed fermion components, and the Hermitian conjugate ensures the Lagrangian remains real.

Without additional constraints, the general potential from Equation 1.5.11 allows for tree-level FCNCs. To avoid these, fermions with identical quantum numbers must interact to one Higgs doublet, which can be enforced by imposing additional discrete Z_2 symmetries.

1.5.3 The Multi-lepton Anomalies

When searching for new physics at the LHC, one must control biases across the collider's vast, multi-dimensional phase space, where SM fluctuations can mimic 3–5σ excesses unless a procedure is fixed a priori. Guided by Run 1 features such as the Higgs p_{T} spectrum and hints in the hh, $t\bar{t}H$ and $b\bar{b}$ channels. The most prominent excess was found in $\ell^+\ell^- + (\text{jets}, b\text{-jets})$ events with $m_{\ell\ell} < 100\,\text{GeV}$, dominated by $t\bar{t}$ and $W^\pm t$ backgrounds, and exceeding 5σ significance. Additional anomalies included e^+e^- events without jets ($m_{\ell\ell} < 100\,\text{GeV}$, $\approx 3\sigma$), same-sign dileptons and trileptons with b-jets and moderate H_T ($> 3\sigma$), same-sign dileptons and trileptons without b-jets, often in association with h ($\approx 4\sigma$), and $Z(\to \ell^+\ell^-)\ell^\pm$ without b-jets and with $p_T^Z < 100\,\text{GeV}$ ($> 3\sigma$). Subsequent Run 2 analyses confirmed these predictions. The originally observed anomalies persisted, and new excesses appeared in the predicted

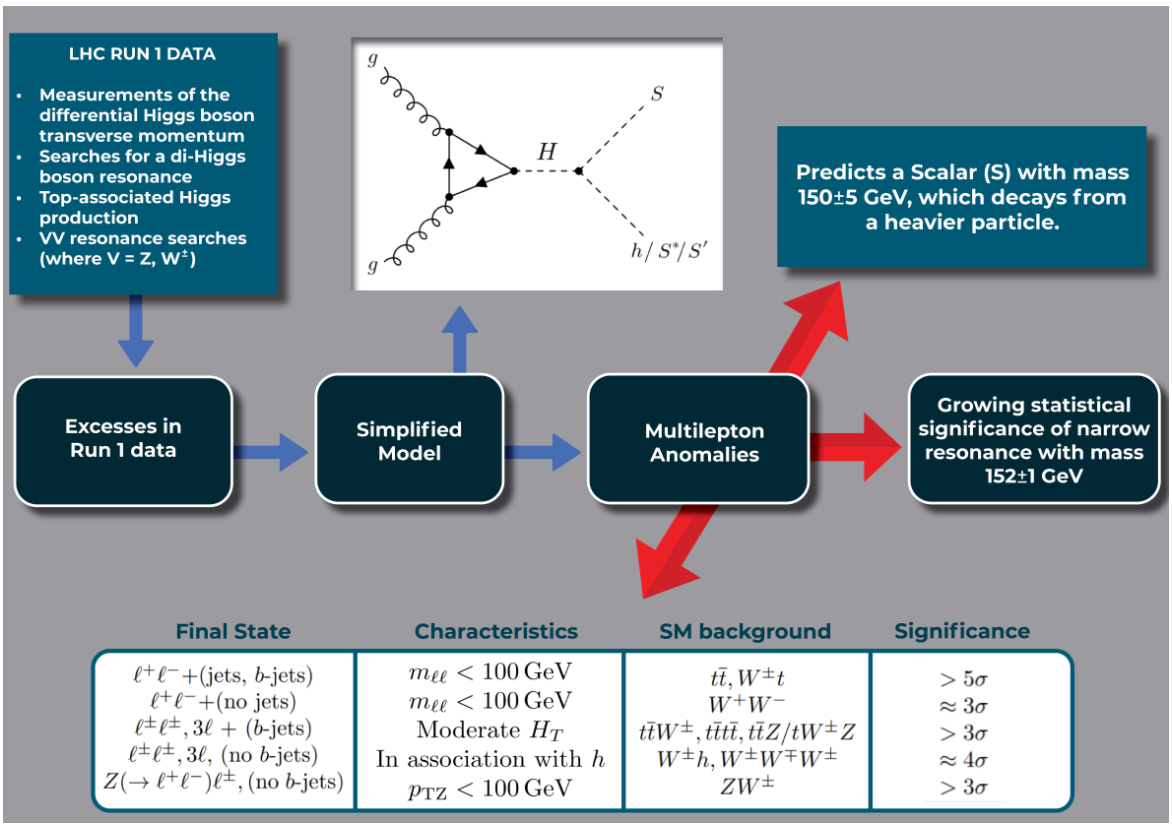


FIGURE 1.3: An overview of the chronological development of the multi-lepton anomalies, which ultimately led to the prediction of a narrow resonance with a mass of $m_S = 150 \pm 5$ GeV. The figure also contains a table summarising the corresponding final states, their main features, the dominant SM backgrounds, and the respective significances of the observed anomalies [14].

channels, with a combined global significance exceeding 8σ [9]. These anomalies predict the existence of a scalar boson with a mass of $m_S = 150 \pm 5$ GeV [8], which is summarised in Figure 1.3 and to be discussed in the next section.

1.5.4 The 152 GeV Scalar Candidate

An analysis of the invariant-mass distribution of $e\mu$ pairs in non-resonant WW events measured $m_S = 150 \pm 5$ GeV [8], motivating searches for S near this mass-especially in diphoton ($\gamma\gamma$) final states. Indeed, ATLAS and CMS Run 2 Higgs side-band studies [18–24] show hints of a narrow resonance around 150 GeV produced with leptons, missing energy, b-jets and electroweak bosons [65]. A 2021 search [65] in the

130–160 GeV window targeting $S \to \gamma\gamma$ and $S \to Z\gamma$ reported a global significance of 3.9σ at $m_S \approx 151.5$ GeV, and a subsequent Run 2 side-band analysis of $\gamma\gamma$, $Z\gamma$ and WW spectra identified a resonance at $m_S = 152 \pm 1$ GeV with a global significance of 5.3σ, while the ZZ channel remained consistent with the SM (no excess).

The statistical significance of the resonance has grown steadily with increasing integrated luminosity, scaling proportionally to the square root of the data, consistent with signal rather than a fluctuation. The evolution of the global significance follows a clear timeline: in 2021, an excess was observed at $m_S \simeq 151.5\,\text{GeV}$ with 3.9σ, primarily from final states such as $S \to Z(\ell^+\ell^-)\gamma + \ell$, $S \to h + E_T^{\text{miss}}$, $S \to \gamma\gamma + E_T^{\text{miss}}$, $S \to \gamma\gamma + b$-jet, and $S \to \gamma\gamma + W, Z$ (with some indications in $\gamma\gamma$ alone). By 2023, additional data and extended final states, including $S \to \gamma\gamma + \geq 4$ jets [66], $S \to WW^* + E_T^{\text{miss}}$ [67, 68] and $S \to \gamma\gamma + \geq 1\ell + 1b$-jet [66], raised the combined global significance to 4.7σ at $m_S \approx 151.5\,\text{GeV}$. In 2024, further updates including channels such as $S \to \gamma\gamma + \tau$ and $S \to \gamma\gamma + 2(\ell, \tau)$ increased the total global significance to 5.33σ at $m_S \approx 152.0\,\text{GeV}$ [65] (see Figure 1.4). This decay pattern aligns with the Real Higgs Triplet (RHT) model with hypercharge $Y = 0$, where S does not interact with ZZ at tree level; in such scenarios, triplet scalars can be Drell–Yan produced and decay to electroweak bosons, enhancing triboson signatures (WWZ, WZZ, WWW), where ATLAS and CMS have reported systematic excesses, including in VVZ and WWZ topologies [7, 9, 10, 69–71]. A summary of the final states selected by the aforementioned procedure from publicly available results provided in Table 1.4.

2021 (Group 1)	**2023 (Group 2)**	**2025 (Group 3)**
$\gamma\gamma + E_T^{\text{miss}}$ [22, 23]	$\gamma\gamma+ \geq (1\ell + 1b\text{-jet})$ [66]	$\gamma\gamma + \tau$ [72]
$\gamma\gamma + W$, Z [18, 73]	$\gamma\gamma+ \geq 4$ jets [66]	$\gamma\gamma + 2(\ell, \tau)$ [72]
$\gamma\gamma + b$-jet [20, 21]	$WW^* + E_T^{\text{miss}}$ [67, 68]	
$\gamma\gamma + 2b$-jets [74]		
$Z(\rightarrow \ell^+\ell^-)\gamma + \ell, jj$ [75]		

TABLE 1.4: List of final states predicted by the simplified model used to interpret the corresponding experimental results. The initial combination performed in 2021 incorporated all channels belonging to Group 1. The subsequent combination in 2023 extended to include channels from both Groups 1 and 2. The most recent combination in 2025 includes all channels from Groups 1, 2, and 3.

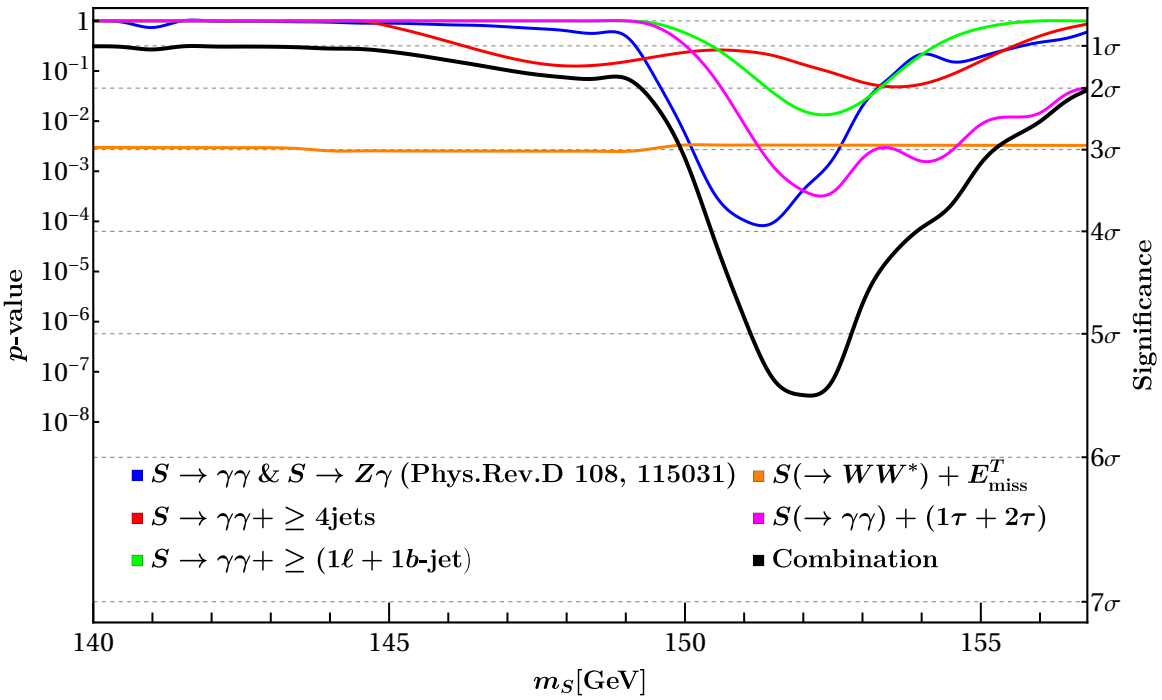


FIGURE 1.4: The p-values of the individual channels, together with their combined result and the corresponding local significance, are presented. The best-fit value is found at 152 GeV, corresponding to a global (local) significance of 5.33σ (5.6σ).

1.5.5 The Triplet Model

The absence of deviations in the ZZ spectrum motivates extending the SM scalar sector in a way that custodial symmetry is violated. A particularly well-suited model is the RHT model with hypercharge $Y = 0$ (hereafter ΔSM). This model extension naturally accommodates the W mass shift found in the current global electroweak fit and reproduces the observed pattern of collider excesses.

The ΔSM adds to the SM a real scalar $\mathrm{SU}(2)_L$ triplet whose spectrum has a CP-even neutral Higgs boson Δ^0 and two singly charged Higgs bosons $\Delta^\pm$, which are quasi-degenerate in mass. In the small-mixing limit with the SM Higgs, Δ^0 decays predominantly into W^+W^-, with loop effects inducing a potentially sizable branching fraction into $\gamma\gamma$. Notably, Δ^0 does not couple to ZZ at tree level, explaining why the ZZ spectrum remains SM-like even in the presence of other anomalies. The triplet scalars at the LHC are mainly produced via Drell-Yan processes: $pp \to \Delta^0\Delta^\pm, \quad pp \to \Delta^+\Delta^-$. Subsequent decays are $\Delta^0 \to W^+W^-$, ZZ, $b\bar{b}$, $\tau^+\tau^-$, $\quad \Delta^\pm \to W^\pm Z$, $t\bar{b}$, $c\bar{s}$, $\tau^\pm\nu$. In the low-mass regime, $\Delta^\pm$ decays predominantly into $\tau\nu$, producing $\tau^+\tau^- + \not{p}_T$ final states similar to supersymmetric $\tilde{\tau}$-pair signatures, leading to current ATLAS and CMS bounds of $m_{\Delta^\pm} \gtrsim 110\,\mathrm{GeV}$ at 95% C.L. In this model the multi-lepton final states arise from processes such as: $\gamma^* \to \Delta^+\Delta^- \to W^+W^-ZZ$ and $W^* \to \Delta^\pm\Delta^0 \to W^\pm Z\, W^+W^-$, and associated $\gamma\gamma$ production occurs via $pp \to W^* \to \Delta^\pm(\Delta^0 \to \gamma\gamma)$ [76–79].

The scalar triplet Δ and doublet φ are represented as:

$$\varphi = \begin{pmatrix} h_\varphi^+ \\ \frac{1}{\sqrt{2}}(v_\varphi + h_\varphi^0 + iG^0) \end{pmatrix}, \quad \Delta = \frac{1}{2}\begin{pmatrix} h_\Delta^+ & \sqrt{2}h_\Delta^{++} \\ \frac{v_\Delta + h_\Delta^0}{\sqrt{2}} & -h_\Delta^+ \end{pmatrix}, \tag{1.5.17}$$

where $h^0_{\varphi,\Delta}$ are real scalars, $h_\Delta^\pm = (h_\Delta^\mp)^*$, and v_φ, v_Δ are their VEVs, satisfying $v^2 = v_\varphi^2 + 2v_\Delta^2 = (246\ \mathrm{GeV})^2$. The scalar potential:

$$\begin{aligned} V = &-\mu_\varphi^2\Phi^\dagger\varphi + \frac{\lambda_\varphi}{4}(\varphi^\dagger\varphi)^2 - \mu_\Delta^2\mathrm{Tr}(\Delta^\dagger\Delta) + \frac{\lambda_\Delta}{4}[\mathrm{Tr}(\Delta^\dagger\Delta)]^2 \\ &+ A\varphi^\dagger\Delta\varphi + \lambda_{\varphi\Delta}\varphi^\dagger\varphi\mathrm{Tr}(\Delta^\dagger\Delta), \end{aligned} \tag{1.5.18}$$

leads to minimisation conditions for μ_φ^2 and μ_Δ^2. Substituting these into the Lagrangian gives the CP-even and charged mass matrices:

$$M_0^2 = \begin{pmatrix} \frac{\lambda_\varphi v_\varphi^2}{2} & \left(\lambda_{\varphi\Delta} v_\Delta - \frac{A}{2}\right) v_\varphi \\ \left(\lambda_{\varphi\Delta} v_\Delta - \frac{A}{2}\right) v_\varphi & \frac{\lambda_\Delta v_\Delta^2}{2} + \frac{A v_\varphi^2}{4 v_\Delta} \end{pmatrix}, \quad M_\pm^2 = \begin{pmatrix} \frac{A v_\varphi}{2} & \frac{A v_\varphi}{4 v_\Delta} \\ \frac{A v_\varphi}{4 v_\Delta} & \frac{A v_\varphi}{2} \end{pmatrix}.$$

Diagonalising with mixing angles α and β,

$$\begin{pmatrix} h \\ h^0 \end{pmatrix} = \mathcal{R}(\alpha) \begin{pmatrix} h_\varphi^0 \\ h_\Delta^0 \end{pmatrix}, \quad \begin{pmatrix} G^\pm \\ \Delta^\pm \end{pmatrix} = \mathcal{R}(\beta) \begin{pmatrix} h_\varphi^\pm \\ h_\Delta^\pm \end{pmatrix},$$

where $\mathcal{R}(\theta)$ is the rotation matrix, yields physical masses:

$$m_h^2 = \frac{\lambda_\varphi v_\varphi^2}{2} + \tan\alpha \left(\lambda_{\Phi\Delta} v_\Delta - \frac{A}{2}\right) v_\Phi, \tag{1.5.19}$$

$$m_{\Delta^0}^2 = \frac{\lambda_\Delta v_\Delta^2}{2} + \frac{A v_\varphi^2}{4 v_\Delta} - \tan\alpha \left(\lambda_{\varphi\Delta} v_\Delta - \frac{A}{2}\right) v_\varphi, \tag{1.5.20}$$

$$m_{\Delta^\pm}^2 = \frac{A v_\varphi^2 + 4 v_\Delta^2}{4 v_\Delta}, \tag{1.5.21}$$

and mixing angles:

$$\tan 2\alpha = \frac{4 v_\varphi v_\Delta (2\lambda_{\varphi\Delta} v_\Delta - A)}{2\lambda_\varphi v_\varphi^2 v_\Delta - 2\lambda_\Delta v_\Delta^3 - A v_\varphi^2}, \tag{1.5.22}$$

$$\tan 2\beta = -\frac{4 v_\varphi v_\Delta}{v_\varphi^2 - 4 v_\Delta^2}. \tag{1.5.23}$$

We identify h with the SM-like 125 GeV Higgs boson; $G^\pm$ and G^0 are Goldstone bosons. All Lagrangian parameters may be written as physical observables $(m_{\Delta^0}, m_{\Delta^\pm}, \alpha, v_\Delta)$:

$$\lambda_\varphi = \frac{2}{v_\varphi^2}\left(\cos^2\alpha\, m_h^2 + \sin^2\alpha\, m_{\Delta^0}^2\right), \tag{1.5.24}$$

$$\lambda_\Delta = \frac{2}{v_\Delta^2}\left[\sin^2\alpha\, m_h^2 + \cos^2\alpha\, m_{\Delta^0}^2 - \frac{v_\varphi^2}{v_\varphi^2 + 4 v_\Delta^2} m_{\Delta^\pm}^2\right], \tag{1.5.25}$$

$$\lambda_{\varphi\Delta} = \frac{1}{2 v_\varphi v_\Delta}\left[\sin 2\alpha \left(m_h^2 - m_{\Delta^0}^2\right) + \frac{4 v_\varphi v_\Delta}{v_\varphi^2 + 4 v_\Delta^2} m_{\Delta^\pm}^2\right], \tag{1.5.26}$$

$$A = \frac{4v_\Delta}{v_\varphi^2 + 4v_\Delta^2} m_{\Delta^\pm}^2. \tag{1.5.27}$$

Therefore, the model has four free parameters beyond the SM: $m_{\Delta^0}, m_{\Delta^\pm}, \alpha$, and v_Δ, and the electroweak precision data constrain v_Δ, favoring $v_\Delta = 3.4 \pm 1.0$ GeV [80–83] when including the CDF II resultt [84], or 2.3 ± 1.7 GeV otherwise. In the limit $\alpha, v_\Delta \to 0$, the neutral and charged triplet components (Δ^0, $\Delta^\pm$) are mass-degenerate, with perturbativity and stability limiting their mass splitting. The model provides a predictive and electroweak framework that simultaneously accounts for the W mass anomaly, the 152 GeV $\gamma\gamma$ excess, and the absence of deviations in the ZZ channel.

Chapter 2

The Large Hadron Collider and the ATLAS Experiment

The ATLAS experiment [5], located at CERN, is one of four main detectors at the LHC [27]. The LHC uses a state-of-the-art accelerator chain to produce high intensity proton or heavy ion beams at unprecedented energies, which collide at four specific points along the beamline. Each collision point is surrounded by advanced detectors, including ATLAS, which is designed to measure the properties of resulting particles with remarkable precision. This chapter provides the structure of the LHC's accelerator system along with a brief summary of the ATLAS experimental setup.

2.1 The Large Hadron Collider

The LHC operates as the world's leading high-energy particle accelerator. It was built by CERN and is situated about 100 m underground near the French-Swiss border in Geneva. This double-ring superconducting hadron collider has a circumference of 26.7 km and uses advanced superconducting magnets to accelerate particles to high energies and luminosities, making it crucial for modern particle physics.

The LHC primarily collides beams of protons or heavy ions at high $\sqrt{s}$ energies, allowing the exploration of fundamental physics phenomena. Proton beams are accelerated through a series of pre-accelerators and directed into two parallel beam pipes circulating in opposite directions. Collisions occur at four interaction points, each housing one of the LHC's major detectors: ATLAS, CMS [6], ALICE [85] and LHCb [86]. ATLAS and CMS are multipurpose detectors focused on precision measurements and searches for new particles BSM. ALICE investigates quark-gluon plasma, while LHCb studies

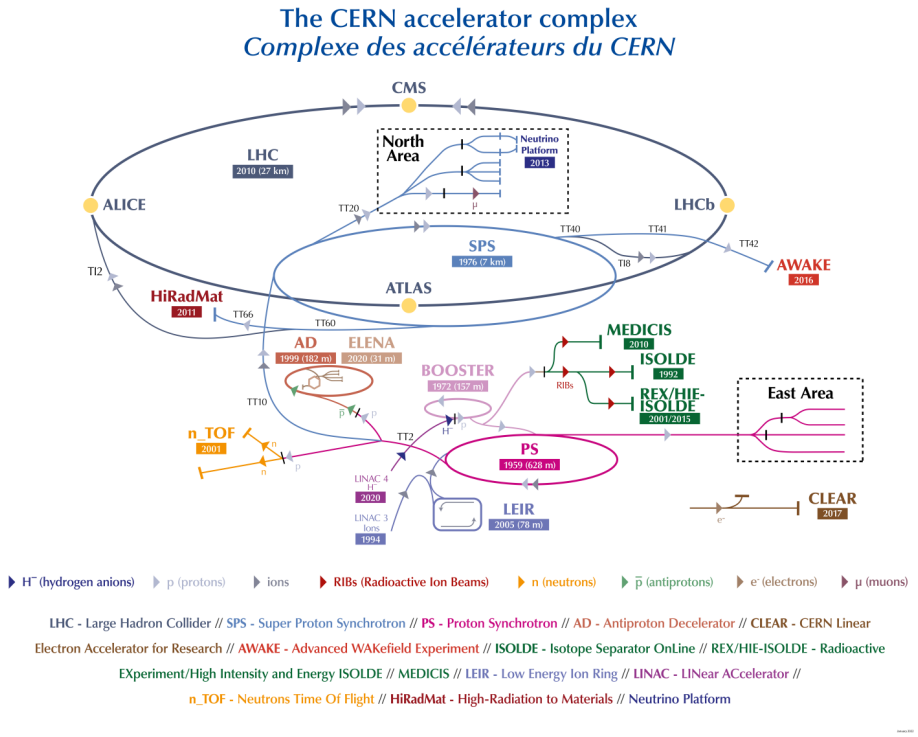


FIGURE 2.1: Sketch of CERN accelerator complex in 2022. Light (dark) grey arrows indicate the typical flight direction of protons (heavy ions) through the complex [87].

b-physics and CP violation to explore matter-antimatter asymmetry.

Protons are prepared through a complex chain of accelerators. Negatively charged hydrogen atoms are ionised to extract protons, which are first accelerated to an energy of 160 MeV using a linear accelerator known as LINAC 4. Then they are directed to LINAC 2, where their energy increases to 50 MeV. They then progress through the Proton Synchrotron Booster (PSB), Proton Synchrotron (PS) and Super Proton Synchrotron (SPS), reaching energies of 2 GeV, 26 GeV, and 450 GeV, respectively. Once injected into the LHC, protons are further accelerated to the TeV scale. The beams are organised into high density bunches, with each beam containing up to 2835 bunches spaced 25 ns apart, and each bunch holding approximately 10^{11} protons, enabling a collision rate of up to 40 MHz. The LHC's superconducting dipole magnets, operating below 2 K and cooled with superfluid helium, maintain the beams' circular

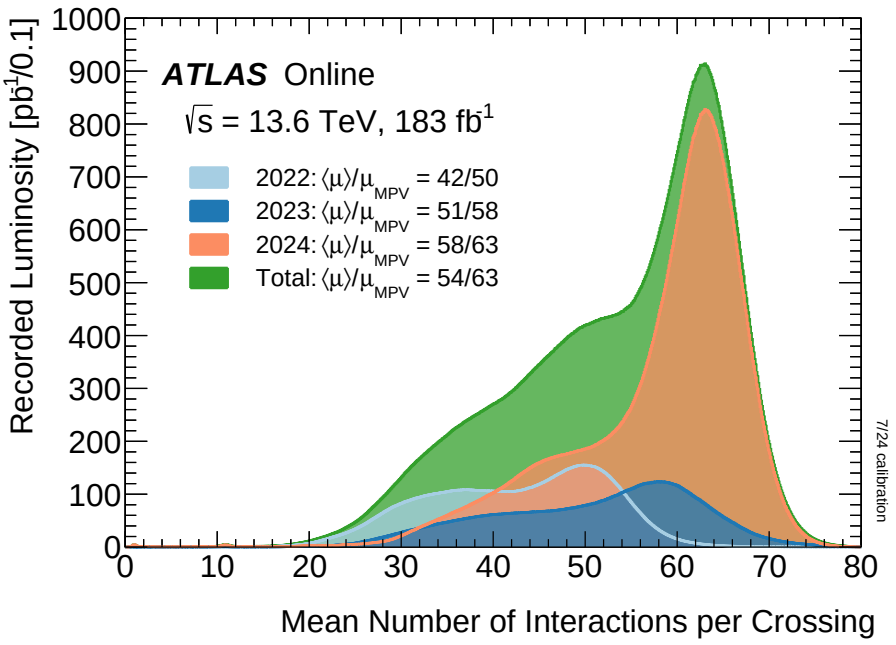


FIGURE 2.2: The mean number of interactions per bunch crossing for $\sqrt{s} = 13.6$ TeV pp collisions data from 2022–2024, weighted by luminosity [88].

paths by generating magnetic fields of up to 8.3 T. Additional quadrupole and higher-order magnets are used for beam focusing and stabilisation.

Integrated luminosity measures the total data collected by the experiments over time. The LHC has undergone several operational phases. During Run 1 (2010-2013), it delivered a total integrated luminosity $\mathcal{L} = 5.46$ fb^{-1} at $\sqrt{s} = 7$ TeV and an additional 22.8 fb^{-1} at $\sqrt{s} = 8$ TeV. After a maintenance period known as Long Shutdown 1 (LS1), the LHC resumed operations in 2015 at $\sqrt{s} = 13$ TeV, achieving its design luminosity and delivering 156 fb^{-1} by the end of Run 2 in 2018. Run 3 began in 2022, reaching $\sqrt{s} = 13.6$ TeV and targeting peak luminosities of 2×10^{34} cm^{-2}s^{-1}. Luminosity is calculated as:

$$\mathcal{L} = \frac{f N_1 N_2 n_b}{4\pi \sigma_x \sigma_y}, \tag{2.1.1}$$

where f is the collision frequency, N_1 and N_2 are the particle counts in each beam, n_b is the number of bunches, and σ_x and σ_y represent the beam dimensions.

Each bunch in the LHC contains approximately 10^{11} protons, essential for achieving the required luminosity (Equation 2.1.1). When two bunches collide at an interaction point, multiple proton-proton (pp) collisions occur. Pileup arises when these collisions happen simultaneously, generating additional particle debris that complicates the detection of primary events. This extra energy makes it challenging for detectors to identify relevant physics events. The pileup interactions are quantified by the average interactions per bunch crossing $\langle\mu\rangle$. During Run 3, the average $\langle\mu\rangle$ in ATLAS was 47.7. Figure 2.2 shows the luminosity-weighted average density $\langle\mu\rangle$. The mean interactions per crossing is calculated as $\mu = L_{\text{bunch}} \times \sigma_{\text{inel}} / f_{\text{r}}$, where L_{bunch} is the instantaneous luminosity per bunch, $\sigma_{\text{inel}} = 80\,\text{mb}$ is the inelastic cross-section, and f_{r} is the LHC revolution frequency.

The 2023 luminosity calibration is preliminary and based on van der Meer scans, a method in which the two beams are transversely displaced to measure their overlap and thus determine the absolute luminosity, while the 2024 data uses an initial online calibration. The integrated luminosity, mean μ and most probable value of μ are also reported. Future plans include the High Luminosity-LHC (HL-LHC) upgrade [89], set for completion in 2029, which aims to increase peak luminosity by a factor of 5 to 7.5 and deliver up to 4 ab^{-1} of integrated luminosity over 12 years, enhancing the LHC's capacity to address fundamental physics questions.

2.2 The ATLAS Experiment

The ATLAS (A Toroidal LHC ApparatuS) detector is one of the two general-purpose detectors at the LHC, aimed at exploring a broad spectrum of physics, from validating the SM to searching for new physics. With over 5500 scientists from 245 institutions across 42 countries, ATLAS is one of the largest scientific projects globally. The detector measures 25 m in diameter, 44 m in length, and weighs around 7000000 kg. Its design accommodates the detection of critical signals for new physics while enduring a harsh radiation environment. ATLAS's capability to measure particle properties with precision is enhanced by its nearly full 4π solid angle coverage, allowing for the reconstruction of most physics processes. This includes the study of the Higgs boson production and decay, and searches for BSM physics. The detector is designed to withstand radiation damage and includes powerful cooling and magnetic field generation

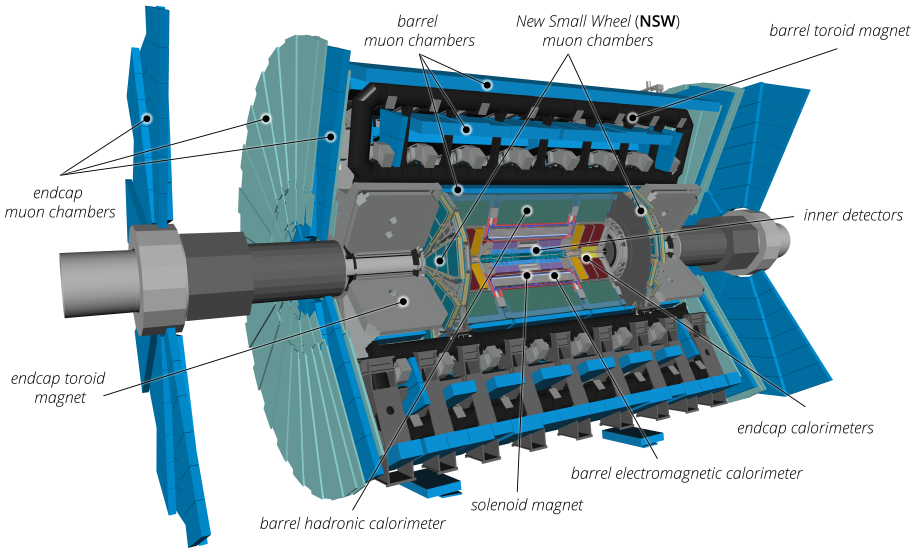


FIGURE 2.3: The layout of the ATLAS Experiment [90].

systems to ensure optimal performance.

ATLAS has concentric sub-detector systems arranged cylindrically around the proton collision point, each serving specific functions:

- **Inner Detector (ID):** Closest to the beam pipe, the ID identifies charged particles and reconstructs their trajectories which is essential for precise momentum measurements and secondary vertex reconstruction.
- **Calorimeters:** Surrounding the ID, these systems measure particle energy. The electromagnetic (EM) calorimeter targets photons and electrons, while the hadronic calorimeter focuses on hadrons.
- **Muon Spectrometer (MS):** The outermost sub-detector identifies and measures muon momenta while using a magnetic field from large superconducting magnets for high accuracy trajectory tracking.

A sophisticated trigger system selects relevant events from the high collision rate, ensuring that only applicable data is recorded. The detector captures all particles produced in pp collisions except neutrinos, which escape detection.

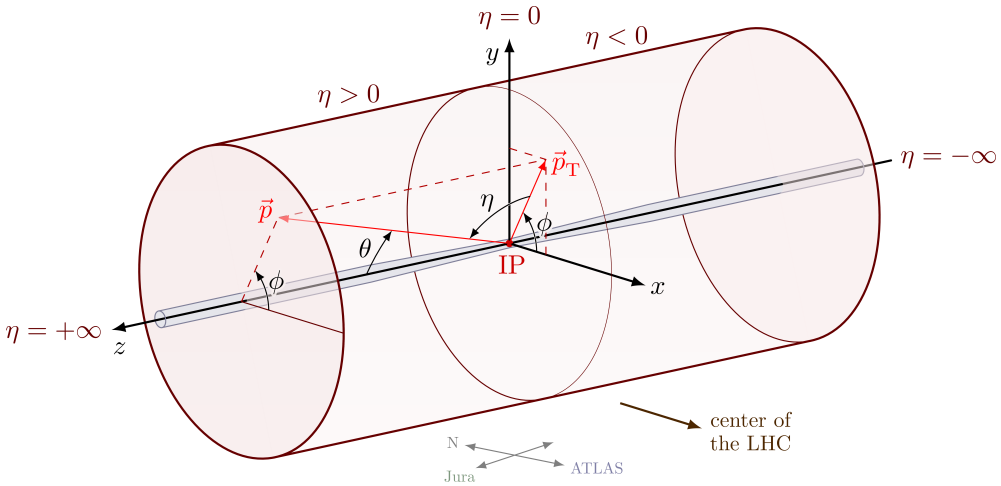


FIGURE 2.4: Sketch of the coordinate system used in ATLAS [91].

ATLAS uses a right-handed Cartesian coordinate system (Figure 2.4) for spatial measurements, with the interaction point being the origin. The cylindrical detector design facilitates cylindrical coordinates:

$$r = \sqrt{x^2 + y^2}, \qquad \phi = \tan^{-1}\left(\frac{y}{x}\right), \qquad \theta = \tan^{-1}\left(\frac{r}{z}\right). \tag{2.2.1}$$

The polar angle θ is sometimes used. The pseudorapidity η, however, is preferred for its Lorentz invariance under boosts along the beam direction:

$$\eta = -\ln\left(\tan\left(\frac{\theta}{2}\right)\right) \tag{2.2.2}$$

The angular separation between two objects is measured using the distance metric in $\eta - \phi$ space:

$$\Delta R = \sqrt{\Delta\eta^2 + \Delta\phi^2}. \tag{2.2.3}$$

As part of the LHC program, ATLAS has undergone significant upgrades during long shutdowns, improving sub-detectors and electronics to enhance data acquisition and analysis capabilities. These advancements keep ATLAS at the forefront of particle physics research as it delves deeper into the universe's mysteries.

2.2.1 The Inner Detector

The ID is the innermost component of the ATLAS experiment, designed to identify and track charged particles [92, 93]. It offers high precision momentum resolution and vertex measurements for particles with $p_T > 500$ MeV within the $|\eta| < 2.5$ pseudorapidity range. Particles with lower momentum cannot be reconstructed as they do not fully traverse the ID. The ID operates in a 2 T magnetic field generated by a superconducting solenoid, which bends the trajectories of charged particles for momentum measurement. The ID is housed in a cylindrical envelope measuring 3512 mm in length and 1150 mm in outer radius, comprising of three main sub-detectors:

- **Pixel Detector:** Located closest to the beam axis, this detector features four concentric layers of silicon pixel sensors, including the innermost Insertable B-Layer (IBL) installed during LS1 [94, 95]. It contains around 92 million pixels, with outer layers measuring $50\,\mu$m $\times$ $400\,\mu$m and the IBL measuring $50\,\mu$m $\times$ $250\,\mu$m. Charged particles ionise the silicon, generating electron-hole pairs that drift towards electrodes due to a voltage bias, where they are detected and amplified.

- **Semiconductor Tracker (SCT):** The SCT has four barrel layers and nine endcap discs, using narrow silicon strip sensors to detect charged particles [96–98]. Each strip is $80\,\mu$m wide and 120 mm long, providing a spatial resolution of $17\,\mu$m radially and $580\,\mu$m longitudinally. It features approximately 6 million readout channels for high granularity.

- **Transition Radiation Tracker (TRT):** The TRT is the outermost ID component, it consists of about 3×10^5 gas-filled straw tubes, each 4 mm in diameter with a gold-plated tungsten wire [99–101]. The tubes are aligned parallel to the beamline in the barrel and perpendicular in the endcap. The TRT detects charged particles by ionising a Xe/Ar gas mixture, and transition radiation from relativistic particles helps distinguish electrons from hadrons, with a spatial resolution of $130\,\mu$m in the $r - \phi$ direction.

Each sub-detector includes a barrel region with concentric cylindrical layers around the beam axis and endcap discs that extend coverage in η without increasing the detector's footprint. Materials in the ID are chosen to optimise radiation tolerance and

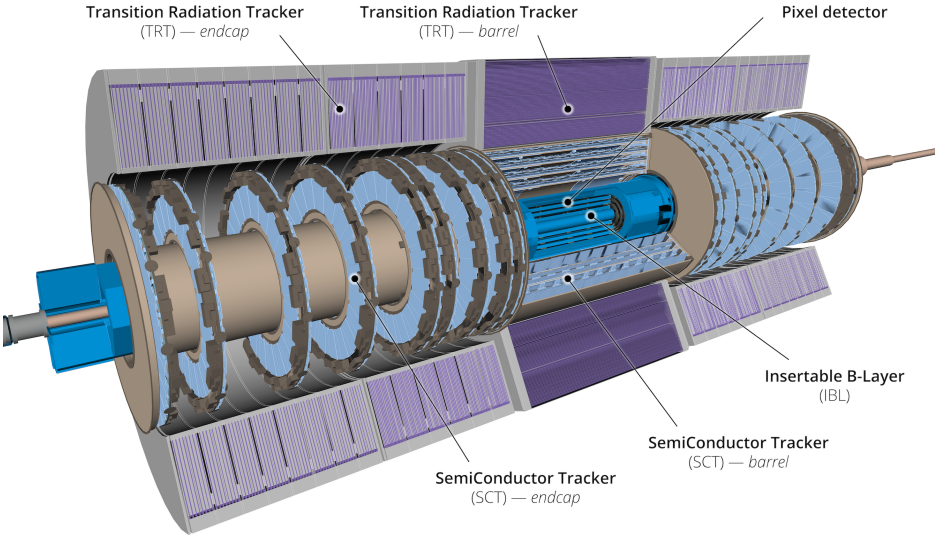


FIGURE 2.5: The Inner Detector of the ATLAS experiment [90].

minimise energy loss for traversing particles.

The overall resolution of the ID decreases with increasing p_T due to reduced track curvature, expressed as:

$$\frac{\sigma_{p_T}}{p_T} = 0.05\% \cdot p_T \oplus 1\%. \tag{2.2.4}$$

During LS3, the ID will be replaced by an all-silicon Inner Tracker, which will enhance the pixel system, introduce a more segmented strip detector, and ensure optimal performance under high-luminosity conditions at the HL-LHC.

2.2.2 The Calorimeter System

The ATLAS calorimeter system [102] measures hadrons, photons, and electrons energies within $|\eta| < 4.9$. It consists of multiple sampling calorimeters that use alternating layers of active and absorbing materials to determine particle energies and provide directional information. These calorimeters are categorised as EM or hadronic based on their design and function.

Sampling calorimeters feature high-density absorbers to enhance interaction probabilities and active materials that generate measurable electronic signals from deposited energy. This design allows compact structures with high granularity, facilitating precise energy measurements and particle identification. Compared to homogeneous calorimeters, sampling calorimeters offer superior lateral and longitudinal segmentation.

The ATLAS calorimeter system comprises four main components:

- **Electromagnetic Calorimeter (ECAL):** The ECAL is a lead/liquid argon (LAr) calorimeter divided into barrel (EMB) and endcap (EMEC) modules, covering $|\eta| < 3.2$ range. Its absorber layers range from 1.1 to 2.2 mm in thickness and is separated by 4 mm LAr gaps. The accordion geometry ensures rapid signal collection which is crucial for high collision rates. The ECAL's thickness is $\geq 22X_0$ across all regions, where X_0 is the radiation length. It provides a fine segmentation to distinguish photons and electrons from background processes, especially in the barrel region ($|\eta| < 1.475$).

- **Hadronic Calorimeter (HCAL):** The HCAL consists of the Tile Calorimeter (TileCal) and the Hadronic Endcap Calorimeter (HEC). The TileCal, using steel absorbers and scintillating tiles, covers $|\eta| < 1.7$ with granularity of $\Delta\eta \times \Delta\phi = 0.1 \times 0.1$. The HEC spans $1.5 < |\eta| < 3.2$, using copper and liquid argon with similar granularity. These calorimeters are essential for measuring hadronic showers, identifying jets, and assessing the missing transverse energy (E_T^{miss}).

- **Forward Calorimeter (FCal):** The FCal completes the pseudorapidity coverage up to $|\eta| < 4.9$. It consists of three modules with copper and tungsten absorbers, optimised for both EM and hadronic measurements, with a total depth of 10 interaction lengths (λ).

The calorimeter system's intrinsic energy resolution is parameterised as:

$$\frac{\Delta E}{E} = \frac{a}{\sqrt{E}} \oplus \frac{b}{E} \oplus c, \tag{2.2.5}$$

where a is the stochastic term, b is the noise term, and c is the constant term for calibration and uniformity. The ECAL achieves a resolution of $\sigma_E/E = 10\%/\sqrt{E} \oplus 0.7\%$, while the HCAL provides $\sigma_E/E = 50\%/\sqrt{E} \oplus 3\%$ in the barrel and endcap regions

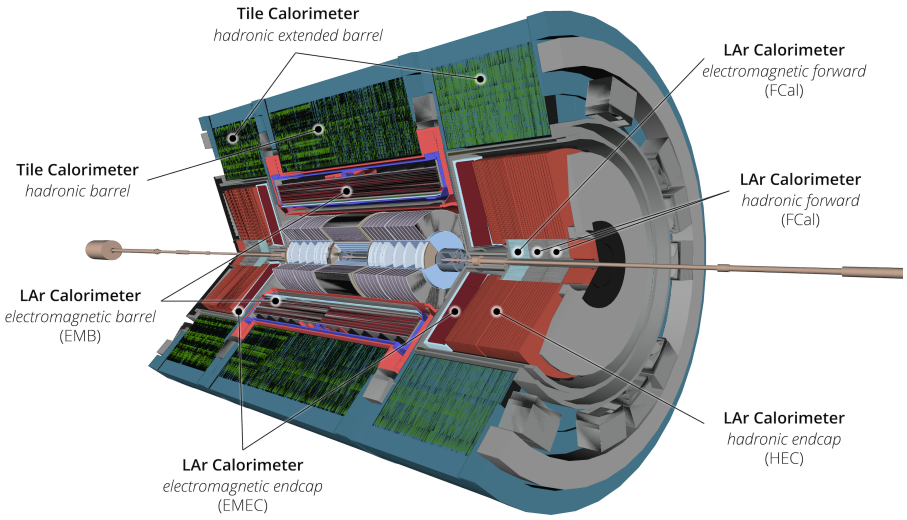


FIGURE 2.6: Cut away sketch of the ATLAS Calorimeter [90].

and $100\%/\sqrt{E} \oplus 10\%$ in the forward region. Surrounding the ID, the calorimeter system ensures accurate energy containment before particles reach the MS.

2.2.3 Muon Spectrometer

The MS is the outermost part of the ATLAS detector [103], and it detects and identifies muons produced in LHC collisions with energies from a few hundred MeV to several hundred GeV. With a mass about 200 times that of an electron, a long mean lifetime ($c\tau \approx 660\,\text{m}$), and weak interactions with matter, muons lose minimal energy while traversing the detector, making them ideal for momentum measurement using a magnetic spectrometer.

The MS spans a pseudorapidity range of $|\eta| < 2.7$ and includes a barrel region and two endcap regions. It operates within a toroidal magnetic field produced by eight large superconducting coils, offering bending powers between 1 and 7.5 Tm, facilitating high-resolution momentum measurements by deflecting muon tracks.

The MS uses various chambers for precision tracking and triggering, each optimised for specific detector regions:

- **Monitored Drift Tube Chambers (MDT):** These primary tracking devices measure muon track curvature with a spatial resolution of about 35 μm longitudinally. MDTs range from 0.85 to 6.5 m in length and 3 cm in diameter, covering most of the η range.
- **Cathode Strip Chambers (CSC):** Positioned in the forward region ($2.0 < |\eta| < 2.7$), CSCs offer higher granularity with a resolution of 40 $\mu\text{m} \times 5\,\text{mm}$ in the $z \times r$ direction which is crucial for high-luminosity environments.
- **Resistive Plate Chambers (RPC):** Used for trigger purposes in the barrel region ($|\eta| < 1.05$), RPCs provide fast responses and coarse position measurements.
- **Thin Gap Chambers (TGC):** Used for triggering in the endcap regions ($1.05 < |\eta| < 2.4$), TGCs deliver fast timing and sufficient position resolution.

The MS's toroidal magnetic field facilitates muon deflection, with a large barrel toroid in the barrel region ($|\eta| < 1.4$) and smaller toroids in the endcap regions ($1.4 < |\eta| < 2.7$). The transition region ($1.4 < |\eta| < 1.6$) benefits from combined fields of the barrel and endcap magnets, ensuring uniform bending power, minimising scattering, and maintaining resolution. The chamber layout provides nearly complete coverage, with barrel chambers arranged in three concentric cylinders (approximately 5 m, 7.5 m and 10 m in radius) and endcap chambers in four disks located at $|z| \approx 7.4$, 10.8, 14 and 21.5 m from the interaction point, covering $1 < |\eta| < 2.7$. Open spaces in the layout allow for cable routing and access to the ID and calorimeters. Chambers are classified as small or large, with small chambers near the barrel toroid coils and large chambers between them, optimising coverage and resolution.

During LS2, the Small Wheel in the MS was replaced with the New Small Wheel (NSW) [104, 105], which integrates Small-Strip Thin Gap Chambers (sTGC) and Micromegas detectors, achieving a position resolution of 50 μm and an angular resolution of 1 mrad. This upgrade enhances efficiency and resolution in the high-luminosity environment of the HL-LHC. The overall p_T resolution of the MS is p_T-dependent, approximately 10% for muons with $p_T = 1\,\text{TeV}$.

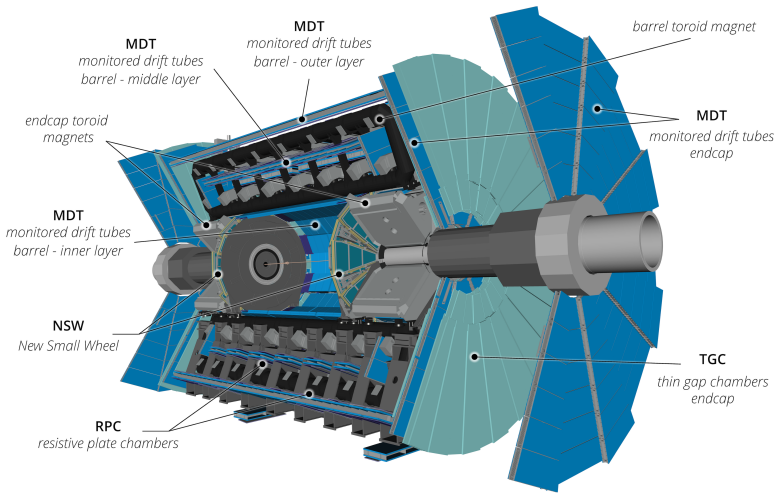


FIGURE 2.7: Cut away sketch of the ATLAS Muon system [90].

2.2.4 Forward Detectors

ATLAS is equipped with several forward systems that play a crucial role in enhancing both physics measurements and ongoing monitoring efforts [106]. Among these systems are the Minimum Bias Trigger Scintillators (MBTS), Zero-Degree Calorimeter (ZDC), Absolute Luminosity For ATLAS (ALFA) Roman pots and the advanced Luminosity measurement system, which uses the Cerenkov Integrating Detector known as LUCID.

The Minimum Bias Trigger Scintillators are designed with a configuration that includes 32 scintillation paddles, each with a thickness of 2 cm. These paddles are strategically arranged in two separate disks, positioned symmetrically on either side of the interaction point. The MBTS effectively covers an $|\eta|$ range that extends from $2.09 < |\eta| < 3.84$, allowing for high precision in detecting minimum bias events.

In terms of luminosity measurement, the LUCID detector functions as a specialised Cerenkov device. This detector spans $5.61 < |\eta| < 5.93$. Its primary function is to capture data from proton scattering events, which are essential for calculating both the integrated and instantaneous luminosity. This information is important for understanding and maintaining optimal conditions of the particle beams.

The ZDC is specifically designed to detect photons and neutrons that are produced in both *pp* and heavy-ion collisions [107]. It operates effectively within a range of

$|\eta| < 8.3$, which is particularly useful for searching neutral particles.

The ALFA system is comprised of four Roman pot [108] stations that are spaced at intervals of 4 m apart, with two stations positioned on either side of the collision point. These stations are installed roughly at $|z| = 240\,\text{m}$ downstream of the interaction point and are carefully placed just 1–1.5 mm from the LHC beams. This precise positioning of the detectors is vital for conducting accurate measurements of elastic scattering and beam optics, both of which are critical to understanding the underlying physics of the collisions.

The forward detectors are installed beyond the main ATLAS detector, located on both sides of the experimental setup. Their strategic positioning is intended to optimise the efficiency of their operation and maximise the measurement coverage they provide, ensuring that the data collected is as comprehensive and informative as possible.

2.2.5 The ATLAS Magnetic System

The ATLAS detector's magnetic system creates fields that bend charged particle trajectories, allowing for precise momentum measurements based on track curvature. This system measures 26 m in length and 22 m in diameter, generating a magnetic field in an approximately 12000 m^3 volume using four large superconducting magnets cooled to about 4.5 K with helium circulated through surrounding tubes. Comprising four superconducting coils arranged parallel to the beam line, the central solenoid provides an axial field of approximately 2 T for the ID, peaking at 2.6 T. The solenoid is designed with minimal material thickness to limit its impact on calorimeter energy measurements.

The toroidal magnet system has the central barrel magnet and two endcap magnets, located outside the calorimeters yet enclosed within the muon spectrometer. These magnets generate toroidal fields of 0.5 T for the barrel and 1 T for the endcap, covering pseudorapidity ranges of $|\eta| < 1.4$ and $1.6 < |\eta| < 2.7$, respectively. In the transition region $1.4 < |\eta| < 1.6$, the overlap of the barrel and endcap fields reduces bending power. This magnetic field configuration provides effective particle deflection, ensuring

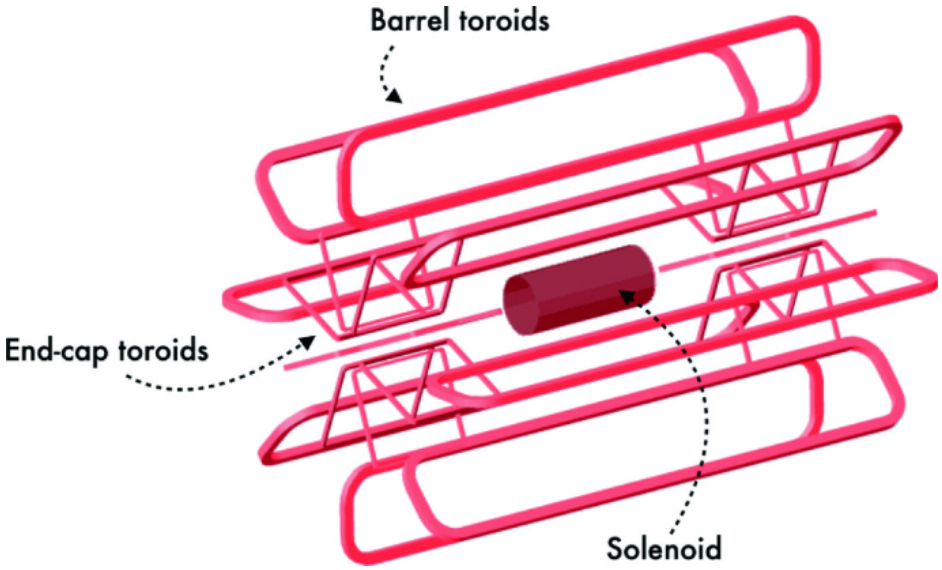


FIGURE 2.8: The ATLAS magnet configuration, displaying the central solenoid together with the barrel and end-cap toroids.

accurate momentum resolution while minimising interference with calorimeter energy measurements.

2.2.6 Trigger System

The LHC operates at a bunch crossing rate of 40 MHz, resulting in approximately 1.7 billion pp collisions per second, at an average of 33.7 interactions per bunch crossing from 2015 to 2018. Due to storage and processing constraints, it is impractical to retain all events, especially since many involve well-understood SM processes. To manage this data effectively, ATLAS uses a multi-level trigger system to filter unwanted events while preserving those of potential significance.

During Run 2, ATLAS used a two-level trigger system consisting of a hardware-based Level-1 (L1) trigger and a software-based High-Level Trigger (HLT) [109]. The L1 trigger, with a latency of 2.5 μs, decreases input rate from 40 MHz to 100 kHz by processing coarse data from the calorimeters and muon system to identify high p_T leptons, jets, and other Regions of Interest (ROIs). Events that pass this trigger are sent to the HLT for further analysis.

The HLT operates on approximately 40000 CPU units, reconstructing physics objects like photons, electrons and jets, similar to offline reconstruction. It maintains an optimal latency of 100 ms, imposing strict requirements on the presence of interesting physics objects. This system decreases event rate from 100 kHz to 1 kHz, allowing storage of only the most relevant events, generating an output stream of about 1 GB/s.

The trigger and data acquisition (TDAQ) system tackles a challenge of rare physics processes with low cross-sections by filtering vast amounts of data to identify significant events through three selection levels: L1, L2 and Event Filter (EF). The L1 trigger uses specialised electronics to quickly process detector data. The L2 refines these choices with more detailed criteria for the ROIs defined by L1. The EF, which integrates L2 and HLT, conducts a comprehensive analysis using complex algorithms, reducing event rates to approximately 200 Hz, making them suitable for storage.

This hierarchical method ensures that only events with notable physics relevance, such as those involving high p_T objects, are archived for further analysis. The system's efficiency allows ATLAS to document and investigate rare processes at the LHC's high-luminosity while effectively managing computational and storage limitations.

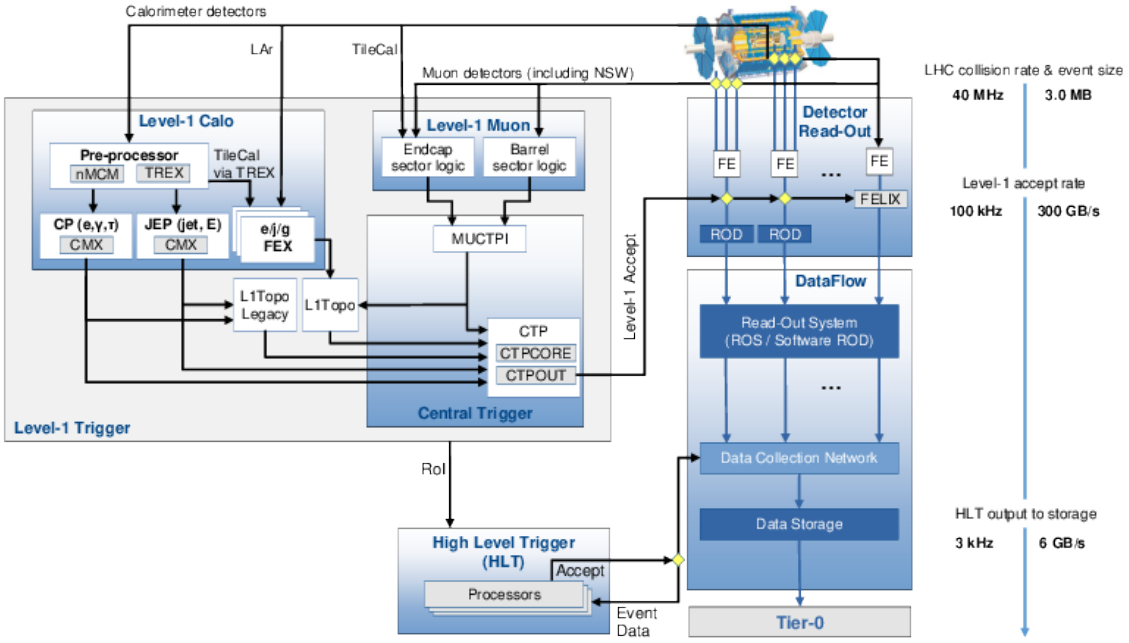


FIGURE 2.9: The ATLAS Trigger Systems with its interfaces to the detector and readout systems [90].

Chapter 3

Object Reconstruction

Proton-proton collisions at the LHC primarily involve interactions among the constituent quarks and gluons within the protons. These collisions can be categorised as either elastic or inelastic. In elastic collisions, the protons retain their initial energies, and no new particles are produced. In contrast, inelastic collisions result in changes to the protons' momenta and often lead to the creation of new particles, which are processes governed by QCD and electroweak theory [110, 111].

Inelastic collisions are significant in particle physics, as they provide the rich event data needed for most analyses. Experimental observations begin with raw detector signals such as track hits and energy measurements within calorimeters generated by the particles produced in these collisions. From this data, physicists reconstruct physical objects like electrons, muons and jets, applying specific selection criteria outlined in later sections.

A key step in this reconstruction is identifying the primary vertex of the collision. This is typically defined as the vertex with the highest sum of squared transverse momentum ($\sum p_T^2$) from associated tracks, where each track has $p_T > 0.4\,\text{GeV}$. Accurate vertex reconstruction is crucial for distinguishing the main collision interaction from additional overlapping collisions and for correctly associating reconstructed particles to their origin.

3.1 Photons and Electrons

The photon is reconstructed by using the supercluster method with the energy deposits in the EM calorimeter. The photon candidate is required to have $p_T > 25\,\text{GeV}$

and $|\eta| < 2.37$. Photons inside the transition region $1.37 < |\eta| < 1.52$ are rejected due to the overlapping geometric coverage and changing detector characteristics between the barrel and endcap subdetectors. This region presents reconstruction challenges as particles may traverse gaps or boundaries between detector components, such as the electromagnetic calorimeters, leading to reduced precision in tracking and energy measurements. The photon candidate must also pass the *Loose* cut-based photon identification selection which is based on the longitudinal and transverse shower profiles measured in the calorimeter. In addition, the photon candidate is required to be non-isolated and pass the FixedCutLoose working point (WP). A candidate event is required to have at least two good non-isolated photons. To match the trigger threshold, the leading photon muat have transverse energy $E_T > 35\,\text{GeV}$ and subleading photon with $E_T > 25\,\text{GeV}$. The diphoton triggers used in the 2022-2023 period can be found in [112]. They are carefully designed to balance signal efficiency and background rejection, taking into account pile-up effects and optimising for different experimental conditions. The use of varying energy thresholds, identification criteria, and Level-1 requirements ensures that the triggers are versatile and robust, capable of capturing a wide range of diphoton events while minimising noise.

Electron reconstruction is performed by matching ID tracks to energy clusters in the EM calorimeter. Electrons must be reconstructed within $|\eta| < 2.47$, excluding $1.37 < |\eta| < 1.52$, and have transverse momentum above 15 GeV. The identification of electrons relies on the MediumDNNLooseVarRad WP, which uses a deep neural network (DNN) that combines calorimeter shower-shape information with track-based variables from the ID. Additional non-isolated WP selections are applied to account for electrons in dense environments. Track-quality requirements impose that the transverse impact parameter significance, $|d_0|/\sigma(d_0)$, to be less than 5 and the longitudinal impact parameter, $|z_0 \sin\theta|$, to remain below 0.5 mm. These requirements help to ensure that selected electrons originate from the primary interaction vertex.

3.2 Hadronically decaying taus

Tau leptons decay via 1-prong and 3-prong topological modes. A 1-prong τ, decays into one charged hadron (such as a pion) along with neutrinos, resulting in a single track in the detector and missing energy. A 3-prong τ, on the other hand, decays into

three charged hadrons (typically pions) and a neutrino, producing a more complex but distinct signature with three visible tracks. We are only interested in the visible hadronic tau (τ_{had}) candidates, as they decay before reaching the detector. They are reconstructed from clusters in the calorimeters and associated ID tracks. We consider candidates with $p_T > 20\,\text{GeV}$ and $|\eta| < 2.5$, excluding $1.37 < |\eta| < 1.52$. We use the Recurrent Neural Network (RNN) loose identification because we want to include more τ_{had} candidates, aiming to maximise signal efficiency, even if it means accepting more background [113, 114]. Specifically, RNN was used because taus decay into prongs, and their decay products form a sequence of tracks that can be modeled sequentially. RNNs are good at capturing dependencies in sequences. The chosen WP used in $\gamma\gamma + ML$ channel has an efficiency of 85% (75%) for 1 (3) prong τ_{had} decays.

3.3 Muons

Muons are reconstructed by using track information from the ID and MS [115]. The candidates must lie within the well-instrumented detector region, corresponding to a pseudorapidity of $|\eta| < 2.5$, where tracking and trigger performance remain optimal. Each candidate must also have a transverse momentum exceeding 15 GeV. Identification of muons relies on the MediumPflowLooseVarRad WP, which applies a set of criteria involving the number of hits in the ID and MS subsystems and the level of agreement between the momentum measurements from both detectors. An additional isolation requirement is imposed, based on the characteristics of ID tracks in the vicinity of the muon, to ensure that the candidate is not produced within a jet. The track quality selections further demand that $|d_0|/\sigma(d_0) < 3$ and $|z_0 \sin\theta| < 0.5$ mm. These impact-parameter constraints suppress contributions from non-prompt muons and are defined consistently with those used for electron identification.

3.4 Jets and b-jets

Jets are reconstructed via the anti-k_t technique [116] with a radius parameter of $R = 0.4$, applied to inputs from the particle-flow (PFlow) reconstruction [117]. The PFlow algorithm combines information from both calorimeter energy deposits and charged-particle tracks to improve the overall jet resolution. Energy corrections are subsequently applied to account for residual effects from noise and the underlying

event, ensuring that the jet energy corresponds to the true particle-level scale. In this analysis, only jets with $p_T > 25$ GeV and $|\eta| < 4.4$ are included. To suppress the influence of multiple pp interactions within the same pile-up, candidates with $p_T < 120$ GeV and $|\eta| < 2.4$ must also pass a dedicated pile-up rejection algorithm based on the jet-vertex-tagger [118]. This requirement enhances the likelihood that selected jets originate from the primary hard-scattering vertex. Additional jet-quality selections are imposed to remove spurious jets arising from calorimeter noise, non-collision backgrounds, or reconstruction artefacts [119]. B-jet identification ("b-tagging") is achieved using the MV2C10 multivariate discriminant [120], which exploits data from track impact parameters and reconstructed secondary vertices.

3.5 Missing Transverse Momentum

Missing transverse momentum ($E_{\mathrm{T}}^{\mathrm{miss}}$), represents any imbalance in the total transverse momentum of an event. It is obtained by taking the negative vector sum of the transverse momenta of all calibrated and reconstructed physics objects, together with contributions from ID tracks that are not matched to these objects but are associated with the primary vertex [121]. Tracks used in this computation are required to have $p_T > 0.4$ MeV and must be linked to the hard scatter vertex. The $E_{\mathrm{T}}^{\mathrm{miss}}$ measurement covers $|\eta| < 2.5$, which is smaller than the calorimeter acceptance of $|\eta| < 4.9$.

Chapter 4

Diphoton studies in association with leptons

This chapter provides supporting material for the diphoton studies in association with leptons and taus using 35.7 fb^{-1} pp collision data at $\sqrt{s}$ = 13.6 TeV. The current data set and the MC samples relevant for this analysis are described in section 4.1. The event selections are summarised in subsection 4.1.4. The sensitivity of the various backgrounds and signal is discussed in section 4.2.

4.1 Data samples

This section introduces the channels: $S' \to 1\ell 1\tau_{\text{had}}$ and $S' \to 0\ell 1\tau_{\text{had}}$, along with the relevant MC samples. Since this study relies heavily on photon performance, it is performed using the $\gamma\gamma$ML package in the `easyjet` analysis framework with 2022 Run 3 ATLAS data corresponding to $\mathcal{L}$ = 35.7 fb^{-1} at $\sqrt{s}$ = 13.6 TeV.

4.1.1 Signal Sample

We used MadGraph5_aMC@NLO [122] for matrix element calculations and Pythia 8 [123] for parton showering and hadronisation. For event generation, we used version 23.6.23 AthGeneration release to obtain an EVNT File. At truth level, the signal sample was generated using Athena release version 25.0.9, with the `derivation_tf.py` algorithm used to produce the TRUTH1-level ROOT files. Details of the signal production process and simulation configuration are provided in Figure 4.1 and Table 4.1. The photon and tau filter criteria applied during event generation are summarised in Table 4.2. The signal was produced via the ggF production mode, with systematic

H **Mass** (GeV)	S **Mass** (GeV)	S' **Mass** (GeV)	**Cross-sections** (fb)	**Events**
250	150	95	1.15	120000
260	160	100	0.412	120000
300	175	125	0.053	120000
350	225	125	0.01	120000
400	275	125	0.004	120000

TABLE 4.1: Summary of the simulation parameters for different scalar masses and cross-sections for the $\gamma\gamma\tau^+\tau^-$ signal.

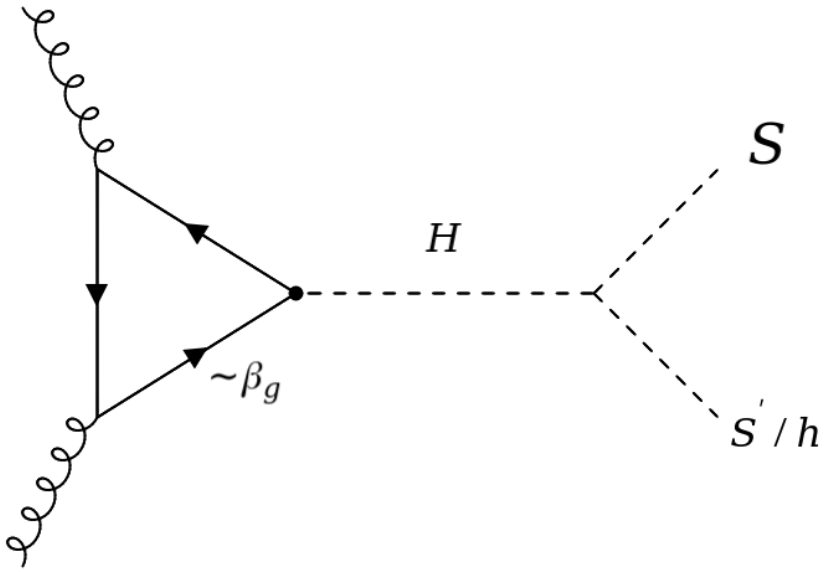


FIGURE 4.1: The $H \to SS'$ decay Feynman diagram, H $[250-400]$, S $[150-270]$ and S' $[95-125]$ GeV.

uncertainties included in the process. The centre-of-mass energy was set to 13.6 TeV, and a total of 120000 events were requested, divided into 20000 events for MC23a, 20000 for MC23d, and 80000 for MC23e. Following the generation of the job options, the total filter efficiency was determined, as illustrated in Figure 4.2.

Selection Criterion	Photon filter	Tau filter
Minimum Transverse Momentum (p_T)	25 GeV	$p_{T_{\ell=e,\mu}} = 12$ GeV, $p_{T_{\text{had}}} = 25$ GeV
Maximum Pseudorapidity (η)	2.5	2.7
Number of Objects Required	2 photons	2 visible taus
Identification	Loose	RNN Medium
Isolation Requirement	None	None

TABLE 4.2: The photon and tau Filters used in event pre-selection for the signal.

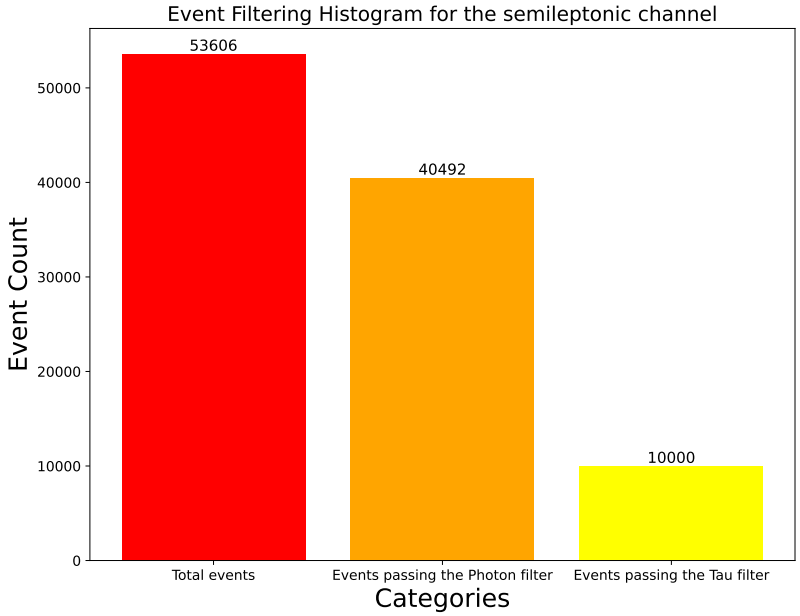


FIGURE 4.2: Event Filtering Histogram for $\gamma\gamma\tau^+\tau^-$ signal. Total Filter Efficiency = 0.187.

4.1.2 MC Background Samples

Continuum backgrounds considered in this analysis originate from the following processes: $\gamma\gamma$ + multijets, $V(VV) + \gamma\gamma$ and $\gamma\gamma t\bar{t}$. Events for $\gamma\gamma$ + multijets process are generated with SHERPA 2.2.4 [124] at NLO accuracy in QCD up to 1 additional parton and at LO accuracy up to 3 partons. Events are generated with NNPDF3.0NNLO PDF [125] along with the dedicated parton shower tuned parameters developed by the SHERPA authors. The multijets samples do not have real leptons in the channels, so these samples can be treated as a fake background since the lepton originates from

Description	$V\gamma\gamma$	$\gamma\gamma t\bar{t}$	$\gamma\gamma$ + **multijets**
Generated Events	523 302	396 278	977 820

TABLE 4.3: Number of events generated for the $V\gamma\gamma$, $\gamma\gamma t\bar{t}$, and $\gamma\gamma$ + multijets background samples.

a misidentified jet. As the misidentified component, the yield and the shape are not consistent with the data behavior. The total number of events for each background sample is given in Table 4.3. All MC samples used in this analysis are weighted and the reweighting procedure is explained in appendix A.1.

4.1.3 Overlap removal

Since different algorithms reconstruct physics objects in parallel, conditions are applied to remove objects that are spatially close to one another, thereby preventing double-counting. The overlap removal procedure is performed immediately after the full object definitions and the selection of two loose photons, ensuring consistency across all samples, including those produced with reverse identification or reverse isolation. The two leading photons are always kept in each event. Electrons within $\Delta R(e,\gamma) < 0.4$ are excluded, as are jets within $\Delta R(jj,\gamma) < 0.4$. Jets located within $\Delta R(jj,e) < 0.2$ are removed, while muons overlapping with photons or jets, defined by $\Delta R(\mu,\gamma) < 0.4$ or $\Delta R(\mu,jj) < 0.4$, are also rejected. In addition, electrons within $\Delta R(e,jj) < 0.4$ of a jet are excluded. The overlap removal criteria can be found in Ref [126].

4.1.4 Object Selection

After removing overlapping objects, a baseline preselection is applied to the relevant physics candidates — namely photons, hadronically decaying τ-leptons, electrons, and muons. These selection criteria are designed to suppress obvious background processes while retaining events most consistent with the targeted $\gamma\gamma + 1\ell\,1\tau_{\text{had}}$ and $\gamma\gamma + 0\ell\,1\tau_{\text{had}}$ final states.

For diphoton candidates, events are required to pass diphoton triggers and to contain two reconstructed photons that satisfy the Loose identification WP and are non-isolated. The leading and subleading photons must have transverse momenta of at least

Description	Background	Signal
Total Events	1897400	28692
Events Passing the Trigger	1897400	28692
Pass Photon WPs	1466317	25099
Pass Photon Selections	1466156	24792
Pass Electron Selections	203000	4792
Pass Muon Selections	198071	4723
Pass Hadronic Tau Selections	7617	3251
Pass 1 Lepton 1 Tau State	6906	2045

TABLE 4.4: The $\gamma\gamma$ + $1\ell 1\tau_{\text{had}}$ channel event selection for $\gamma\gamma t\bar{t}$, $\gamma\gamma$ + multijets, $V\gamma\gamma$ background and the $\gamma\gamma\tau^{+}\tau^{-}$ signal samples.

35 GeV and 25 GeV, respectively. In addition, photons falling within the calorimeter barrel–endcap transition region $1.37 < |\eta| < 1.52$ are excluded, and both photons must lie within $|\eta| \leq 2.37$.

Hadronic τ-lepton candidates are reconstructed using the RNN algorithm and must satisfy the Loose WP, have $p_T \geq 25$ GeV and exclude $1.37 < |\eta| < 1.52$, with an acceptance range of $|\eta| < 2.5$.

Electrons are selected using the MediumDNNLoose VarRad WP. They must have $p_T \geq 10$ GeV, satisfy $|\eta| \leq 2.5$, and are excluded if located in the transition region $1.37 < |\eta| < 1.52$. Muon candidates must pass the MediumPflow Loose VarRad WP, including $p_T \geq 10$ GeV and $|\eta| \leq 2.5$.

After applying baseline preselection, which ensures that all physics objects satisfy consistent quality, kinematic, and geometric acceptance criteria, the signal and background events that meet the channel requirements (Table 4.4 and Table 4.5) are used for the subsequent analysis.

Description	Background	Signal
Total Events	1897400	28692
Events Passing the Trigger	1897400	28692
Pass Photon WPs	1466317	25099
Pass Photon Selections	1466156	24792
Pass Hadronic Tau Selections	713815	17036
Pass 0 Lepton 1 Tau State	713815	17036

TABLE 4.5: The $\gamma\gamma$ + $0\ell 1\tau_{\text{had}}$ channel event selection for $\gamma\gamma t\bar{t}$, $\gamma\gamma$ + multijets, $V\gamma\gamma$ background and the $\gamma\gamma\tau^{+}\tau^{-}$ signal samples.

4.2 Multivariate Analysis Strategies

For the classification task, multiple discriminatory variables are chosen as inputs to train the Deep Neural Network to separate between signal and background. The DNN output, which reflects an optimal combination of these inputs, determines the signal regions of the two channels in order to have good significance

In order to improve this sensitivity with limited MC statistics, a 4-fold cross-validation training is used, which gives a better and smoother Receiver Operating Characteristics (ROC) curve. The training and testing samples are separated by the event number, which is reproducible for each simulation event. The whole dataset is split into 3 parts: training, testing and validation datasets.

These variables are described as follows, and their kinematic distributions are shown in appendix A.3:

- H_T^{all} : Transverse momentum scalar sum of jets, photons, leptons and hadronic taus.
- Sphericity$_T$: Transverse sphericity, an event-shape variable built from jet momentum.
- $\Delta\phi(\gamma_1, \gamma_2)$: Azimuthal angle separation between the two selected photons.
- $\Delta R(\gamma_1, \gamma_2)$: Angular separation between the two photons ($\sqrt{(\Delta\eta)^2 + (\Delta\phi)^2}$).

Variable	$\gamma\gamma + 1\ell 1\tau_{\text{had}}$	$\gamma\gamma + 0\ell 1\tau_{\text{had}}$
H_T^{all}	✓	✓
Sphericity_T	✓	✓
$\Delta\phi(\gamma_1, \gamma_2)$	✓	✓
$\Delta R(\gamma_1, \gamma_2)$	✓	✓
$\lvert y_{\gamma\gamma}\rvert$	✓	✓
$\cos\theta^*_{\gamma\gamma}$	✓	✓
$p_T^{\ell\text{Sys}}$	✓	
$\Delta\phi(\gamma\gamma, \tau_{\text{had}})$	✓	
$\eta(\gamma_1)$	✓	✓
$\eta(\gamma_2)$	✓	✓
$\Delta\phi(\gamma\gamma, \ell)$	✓	

TABLE 4.6: Input variables used for DNN training in the $\gamma\gamma + 1\ell 1\tau_{\text{had}}$ and $\gamma\gamma + 0\ell 1\tau_{\text{had}}$ channels.

- $|y_{\gamma\gamma}|$: Absolute rapidity of the diphoton system.
- $\cos\theta^*_{\gamma\gamma}$: Cosine of the scattering angle of the diphoton system in the Collins–Soper frame.
- $p_T^{\ell\text{Sys}}$: Lepton system transverse momentum ($\gamma\gamma + 1\ell 1\tau_{\text{had}}$).
- $\Delta\phi(\gamma\gamma, \tau_{\text{had}})$: Azimuthal angle difference between the diphoton system and the hadronic tau candidate.
- $\eta(\gamma_{1,2})$: The leading and subleading photon pseudorapidity.
- $\Delta\phi(\gamma\gamma, \ell)$: Azimuthal angle difference between the diphoton system and the lepton.

The variables used as input features for DNN in the $\gamma\gamma + 1\ell 1\tau_{\text{had}}$ and $\gamma\gamma + 0\ell 1\tau_{\text{had}}$ channels are listed in Table 4.6. Table 4.7 lists the separation power (ΔAUC) of DNN variables to separate signal and background. The correlation matrices of the two channels are shown in appendix A.2 and the hyperparameters used are explained in appendix A.3.

$\gamma\gamma + 1\ell 1\tau_{\text{had}}$			$\gamma\gamma + 0\ell 1\tau_{\text{had}}$		
Variable	**Rank**	**ΔAUC**	**Variable**	**Rank**	**ΔAUC**
$p_T^{\ell\text{Sys}}$	1	0.150	H_T^{all}	1	0.280
H_T^{all}	2	0.130	$\eta(\gamma_1)$	2	0.018
$\eta(\gamma_1)$	3	0.050	$\eta(\gamma_2)$	3	0.017
$\Delta\phi_{\gamma\gamma}$	4	0.032	$\lvert y_{\gamma\gamma}\rvert$	4	0.012
$\eta(\gamma_2)$	5	0.023	$\Delta R_{\gamma\gamma}$	5	0.011
$\Delta\phi(\gamma\gamma, \ell)$	6	0.030	$\Delta\phi_{\gamma\gamma}$	6	0.010
$\Delta\phi(\gamma\gamma, \tau_{\text{had}})$	7	0.021	Sphericity_T	7	0.007
$\Delta R_{\gamma\gamma}$	8	0.015	$\cos\theta^*_{\gamma\gamma}$	8	0.003
$\lvert y_{\gamma\gamma}\rvert$	9	0.013			
Sphericity_T	10	0.011			
$\cos\theta^*_{\gamma\gamma}$	11	0.002			

TABLE 4.7: The separation power of DNN variables for the $\gamma\gamma + 1\ell 1\tau_{\text{had}}$ and $\gamma\gamma + 0\ell 1\tau_{\text{had}}$ channels.

4.3 Estimation of Statistical Significance

To evaluate the expected significance Z, the DNN output distribution is divided into 10 bins and significance is computed in different regions of the DNN selection using Equation 4.3.1:

$$Z = \sqrt{2\left[(N_s + N_b)\ln\left(1 + \frac{N_s}{N_b}\right) - N_s\right]}, \tag{4.3.1}$$

where N_s and N_b are weighted signal and background yields (see Table 4.8 and Table 4.9). The resulting DNN output distributions and ROC curves are shown in Figure 4.3, Figure 4.4, and Figure 4.5. The AUC scores demonstrate good separation. For the $\gamma\gamma + 1\ell 1\tau_{\text{had}}$ channel, the AUC scores are 86.6% for the training and 86.0% for the testing. Similarly, for the $\gamma\gamma + 0\ell 1\tau_{\text{had}}$ channel, the corresponding AUC values are 79.2% and 79.0% for training and testing, respectively. For the $\gamma\gamma + 0\ell 1\tau_{\text{had}}$ channel, the best signal to background separation is best at $0.8 <$ DNN, as shown in Figure 4.3. However, due to the limited statistical precision in this region, a more conservative choice of $0.5 <$ DNN is used as the Tight DNN region. For the $\gamma\gamma + 1\ell 1\tau_{\text{had}}$ channel, the best separation is observed for $0.6 <$ DNN, as illustrated in Figure 4.4. The expected significances are found to be 2.04σ for the $\gamma\gamma + 1\ell 1\tau_{\text{had}}$ channel and 1.63σ for the $\gamma\gamma + 0\ell 1\tau_{\text{had}}$ channel, respectively.

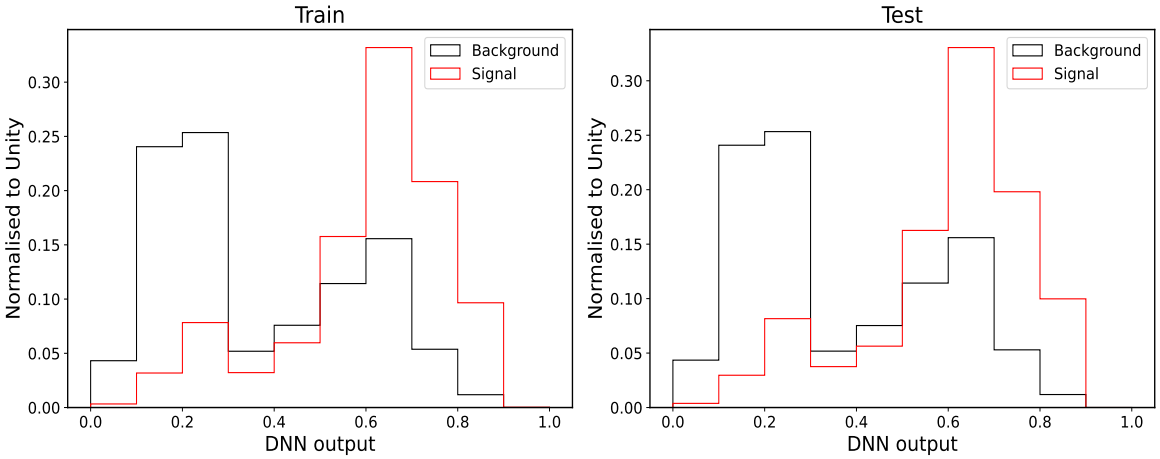


FIGURE 4.3: DNN response for the $\gamma\gamma + 0\ell 1\tau_{\text{had}}$ channel.

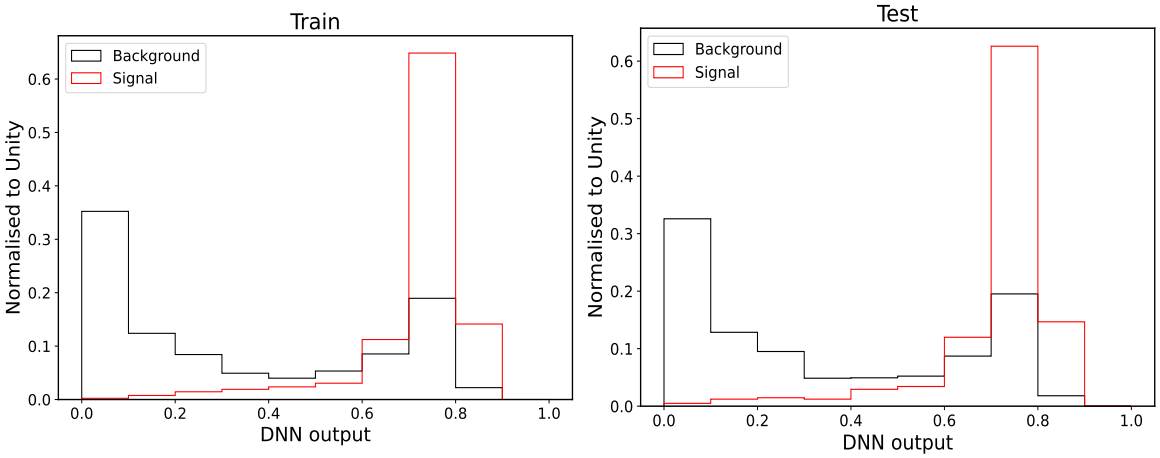


FIGURE 4.4: DNN response for the $\gamma\gamma + 1\ell 1\tau_{\text{had}}$ channel.

Process	$\geq \gamma\gamma \ + 1\ell 1\tau_{\text{had}}$	DNN Response > 0.6
Signal	40.28	36.5
Background	600.12	284.75

TABLE 4.8: Weighted signal and background yields after event selection and DNN response cut for the $\gamma\gamma \ + 1\ell 1\tau_{\text{had}}$ channel.

Process	$\geq \gamma\gamma \ + 0\ell 1\tau_{\text{had}}$	DNN Response > 0.5
Signal	560.17	521.75
Background	2.06×10^5	1.02×10^5

TABLE 4.9: Weighted signal and background yields after event selection and DNN response cut for the $\gamma\gamma \ + 0\ell 1\tau_{\text{had}}$ channel.

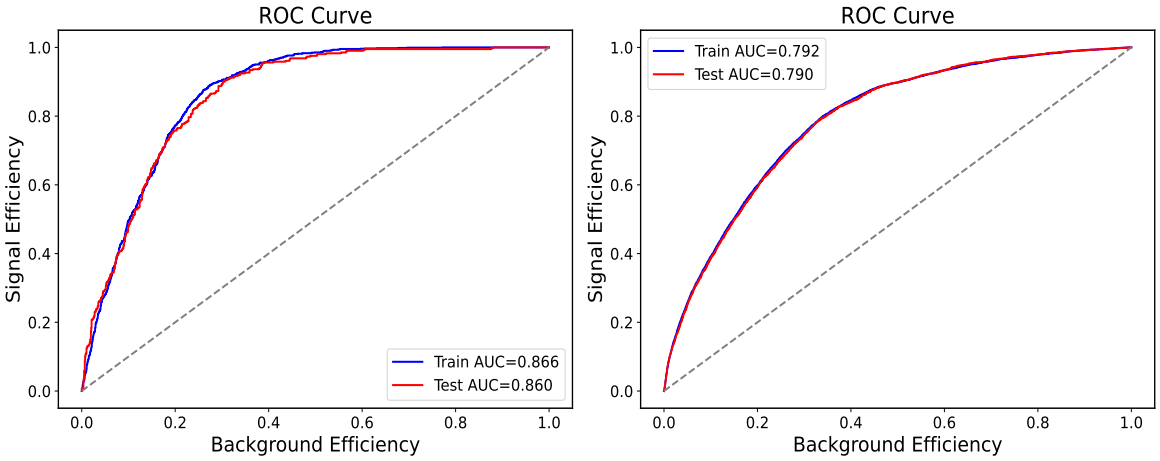


FIGURE 4.5: ROC curves for the $\gamma\gamma + 1\ell 1\tau_{\text{had}}$ (left) and $\gamma\gamma + 0\ell 1\tau_{\text{had}}$ (right) channels.

Chapter 5

Constraining SMEFT Wilson Coefficients in the $h \to Z\gamma$ decay at the LHC

As mentioned in chapter 1, the Higgs boson (h) [2–4] was discovered by the LHC in 2012 [5, 6] and this marked a cornerstone in our understanding of electroweak symmetry breaking and mass generation in the SM. Subsequent precision measurements of its mass, spin, and parity have confirmed consistency with SM expectations, with mass of $m_h = 125.09 \pm 0.21\ (\text{stat}) \pm 0.11\ (\text{syst})$ GeV [127]. Further analyses using Run 2 data [128–130] have refined these results, reinforcing the SM interpretation of the Higgs boson. However, several rare decay channels remain partially investigated, among them the loop-induced process $h \to Z\gamma$ (see Figure 5.1), which has not yet been observed with high statistical significance. This decay proceeds through quantum loops involving charged fermions and W bosons, making it particularly sensitive to virtual effects from heavy, BSM particles that could alter the coupling structure of the Higgs sector.

Within SM, $h \to Z\gamma$ branching ratio is predicted to be $\text{Br}(h \to Z\gamma) = (1.54 \pm 0.09) \times 10^{-3}$ at $m_h = 125.09$ GeV [131], which is set 3.6 times the SM prediction, while 2.6 times is expected in the presence of SM Higgs. Experimental searches by ATLAS and CMS using the full Run 2 pp collision data collected at $\sqrt{s} = 13$ TeV, with $\mathcal{L} = 139$ fb^{-1} and 137 fb^{-1} respectively, have not observed a statistically significant excess above the expected background. ATLAS observed (expected) significance of 1.9σ (1.6σ), while the CMS Collaboration found a similar significance of 1.9σ (2.0σ). ATLAS and CMS set upper limits on the production cross section times branching

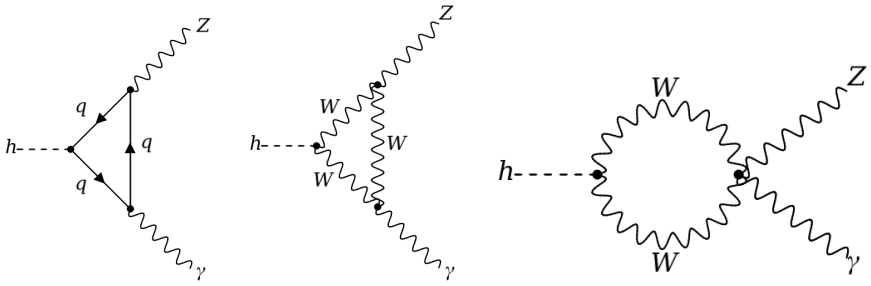


FIGURE 5.1: Feynman diagrams for the $h \to Z\gamma$ decay [75].

ratio of 6.6 (5.2) at 36.1 fb^{-1} and 7.4 (6.0) at 35.9 fb^{-1} times the SM prediction at the 95% confidence level (CL), respectively [132, 133]. Despite these null results, the sensitivity to this decay has reached a level where even small deviations from the SM could be probed, motivating a deeper theoretical investigation into possible new physics effects.

5.1 Model independent analysis in SMEFT

The $h \to Z\gamma$ process is a loop-induced decay in SM, making it particularly sensitive to effects from physics BSM. Its small branching ratio and dependence on heavy virtual particles make it a powerful probe for new interactions. To interpret potential deviations from SM predictions in a model-independent manner, this analysis adopts SMEFT framework [134].

SMEFT provides a systematic way to parameterise the effects of new physics appearing at an energy scale Λ much higher than that directly accessible at the LHC. In SMEFT, SM Lagrangian is augmented through the inclusion of higher-dimensional operators that respect SM gauge symmetries, with each operator suppressed by Λ. Each operator $\mathcal{O}_i^{(d)}$ is associated with a Wilson coefficient $C_i^{(d)}$ that quantifies the deviation from SM prediction:

$$\mathcal{L}_{\text{SMEFT}} = \mathcal{L}_{\text{SM}} + \sum_{d>4} \frac{C_i^{(d)}}{\Lambda^{d-4}} \mathcal{O}_i^{(d)}, \tag{5.1.1}$$

Deviations from SM values in Higgs decay can be expressed in terms of the signal strength:

$$\mu_{h\to X} = \frac{\Gamma(\text{SMEFT}, h \to X)}{\Gamma(\text{SM}, h \to X)} = 1 + \frac{\Gamma(\text{BSM}, h \to X)}{\Gamma(\text{SM}, h \to X)} = 1 + \delta R_{h\to X}, \tag{5.1.2}$$

where $\Gamma(\text{BSM})$ denotes the contribution to the decay width arising solely from new physics, and $\delta R_{h\to X}$ encodes SMEFT correction to SM prediction. New physics effects would therefore shift $\mu_{h\to X}$ from unity.

For the $h \to Z\gamma$ decay, the relevant SMEFT operators modify the Higgs couplings to electroweak gauge bosons, therefore affecting both the decay rate and associated kinematic distributions. Following the theoretical studies in Refs. [135–137], the leading dimension-six operators contributing to the $h \to Z\gamma$ decay are:

$$\mathcal{O}_{\phi B} = (\phi^\dagger \phi)\, B_{\mu\nu} B^{\mu\nu}, \quad \mathcal{O}_{\phi W} = (\phi^\dagger \phi)\, W^I_{\mu\nu} W^{I\,\mu\nu}, \quad \mathcal{O}_{\phi WB} = (\phi^\dagger \tau^I \phi)\, W^I_{\mu\nu} B^{\mu\nu}. \tag{5.1.3}$$

Here, ϕ denotes the Higgs doublet field, $B_{\mu\nu}$ and $W^I_{\mu\nu}$ are the field-strength tensors of $U(1)_Y$ and $SU(2)_L$ gauge symmetries, respectively, and τ^I are the Pauli matrices acting in $SU(2)_L$ space. These operators directly modify the $h \to Z\gamma$ vertices and are key to probing BSM effects in Higgs–gauge interactions. The ggF production process, another loop-induced mechanism in SM, the dominant SMEFT contribution arises from the operator:

$$\mathcal{O}_{\phi G} = (\phi^\dagger \phi)\, G^A_{\mu\nu} G^{A\,\mu\nu}, \tag{5.1.4}$$

where $G^A_{\mu\nu}$ is the field-strength tensor of $SU(3)_C$ gauge group and A runs over the adjoint color indices. The corresponding Wilson coefficient $C_{\phi G}$ modifies the effective Higgs–gluon coupling and directly affects the $gg \to h$ production rate.

Together, these operators form the dominant subset of SMEFT parameters relevant for constraining BSM effects in the $h \to Z\gamma$ and $gg \to h$ sectors. By comparing SMEFT predictions to experimental limits on $h \to Z\gamma$ and related Higgs observables, one can constrain combinations of Wilson coefficients and translate current experimental precision into quantitative bounds on new physics.

The model presented here uses one-loop corrections to the $h \to Z\gamma$ amplitude within the $\{G_F, M_W, M_Z\}$ input scheme [138–141], where the electroweak parameters are fixed to:

$$G_F = 1.166 \times 10^{-5}\ \text{GeV}^{-2}, M_W = 80.39\ \text{GeV}, M_Z = 91.19\ \text{GeV}. \tag{5.1.5}$$

Using these inputs, the amplitude is evaluated to extract bounds on the Wilson coefficients $\{C_{\phi B}, C_{\phi W}, C_{\phi WB}\}$ and associated third-generation quark operators that enter through loop corrections. The best-fit values are obtained through a global χ^2 minimisation incorporating both Higgs decay and production observables, as detailed in section 5.3.

5.2 Signal and Background Simulation

The MC samples were generated using tools such as MadGraph5_aMC@NLO [122], which computes matrix elements for $gg \to h$ production at NLO accuracy in QCD. Pile-up events were generated using Pythia 8.186 [123] with NNPDF2.3LO PDFs and A3 tune [142]. The detector simulation was incorporated via Delphes [143]. The model file was obtained using the `SMEFT@NLO` package, which automates SMEFT calculations through models generated with `FeynRules` [144]. The latter is a tool used to define particle interactions in the SM and its possible extensions.

The samples were normalised using the latest SM production cross-section calculations at $m_h = 125.09$ GeV for the ggF process [145–150]. The branching ratio was computed at leading order in QCD [145, 151, 152].

The $Z\gamma$ backgrounds ($pp \to Z\gamma$) were simulated using Sherpa v2.2.2 with a fast calorimeter simulation. The production modes analysed are summarised in Table 5.1, with the associated cross-sections and event weights provided in Table B.1 and Table B.2.

Production Mode	Signal	Background
ggF	$gg \to h \to Z(\ell^+\ell^-)\gamma$	$pp \to \ell^+\ell^-\gamma$ (leptonic)
	$gg \to h \to Z(jj)\gamma$	$pp \to jj\gamma$ (jet)
	$gg \to h \to Z(\nu\bar{\nu})\gamma$	$pp \to \nu\bar{\nu}\gamma$ (neutrino)

TABLE 5.1: The ggF production mode and its corresponding signal and background processes.

5.3 Constraining SMEFT Wilson Coefficients

To constrain SMEFT Wilson coefficients, we first identify the most sensitive kinematic variable using a Random Forest classifier (see appendix B.2). This variable, selected as the optimal feature, is then used to refine the resolution of the differential distributions by optimising the invariant mass window. Two complementary strategies are adopted: an inclusive approach, integrating over all relevant kinematic regions, and a bin-by-bin analysis, which examines individual bins of the differential distribution to enhance sensitivity to potential deviations from SM expectations. The differential distributions are subsequently reweighted using corrected cross sections obtained from the constrained Wilson coefficient values. The comparison between the theoretical predictions and experimental data is performed through a χ^2 minimisation procedure defined as:

$$\chi^2 = \sum_{k=1}^{n} \left(\frac{\sigma_k^{\text{BSM}}(C_i) - \sigma_k^{\text{SM}}}{\Delta\sigma_k} \right)^2, \tag{5.3.1}$$

$$\Delta\sigma_k = \sqrt{\frac{\sigma_k^{\text{SM+Bkg}}}{\mathcal{L}} + \left(\delta_s\, \sigma_k^{\text{SM+Bkg}}\right)^2}, \tag{5.3.2}$$

Here, σ_k represents the cross-section in the k-th bin, C_i are the Wilson coefficients and δ_s corresponds to the systematic uncertainty which is assumed to be 5%. The cross section in the presence of new physics can be expressed as [153–156]:

$$\sigma^{\text{BSM}} = \sigma^{\text{SM}} + \sum_i C_i A_i + \sum_{i,j} C_i C_j B_{ij}, \tag{5.3.3}$$

where A_i and B_{ij} represent the interference and quadratic BSM contributions, respectively.

A multi-parameter fit is then performed by simultaneously varying all relevant Wilson coefficients within the benchmark range $[-2, 2]$. The posterior distributions are obtained through a Markov Chain Monte Carlo scan. The GetDist package [157] is used to extract credible intervals, visualise parameter correlations, and determine 95% CL exclusion limits on the Wilson coefficients. The most sensitive observables identified for the $\ell\ell\gamma$, $jj\gamma$ and $\nu\bar{\nu}\gamma$ channels, respectively are shown in Figure B.1, Figure B.2 and Figure B.3. Using these observables, we obtain the two-dimensional 95% CL contours for different combinations of Wilson coefficients within SMEFT, as presented in Figure 5.2, Figure 5.3 and Figure 5.4 These contour plots illustrate the allowed parameter regions for the inclusive and multi-bin analyses. As expected in Figure 5.2, the inclusive and multi-bin are more or less the same in constraining the Wilson coeffiecnts. Meanwhile in Figure 5.3, the inclusive case provides tighter constraints on the coefficients and in Figure 5.4 the multi-bin approach provides tighter constraints on the coefficients.

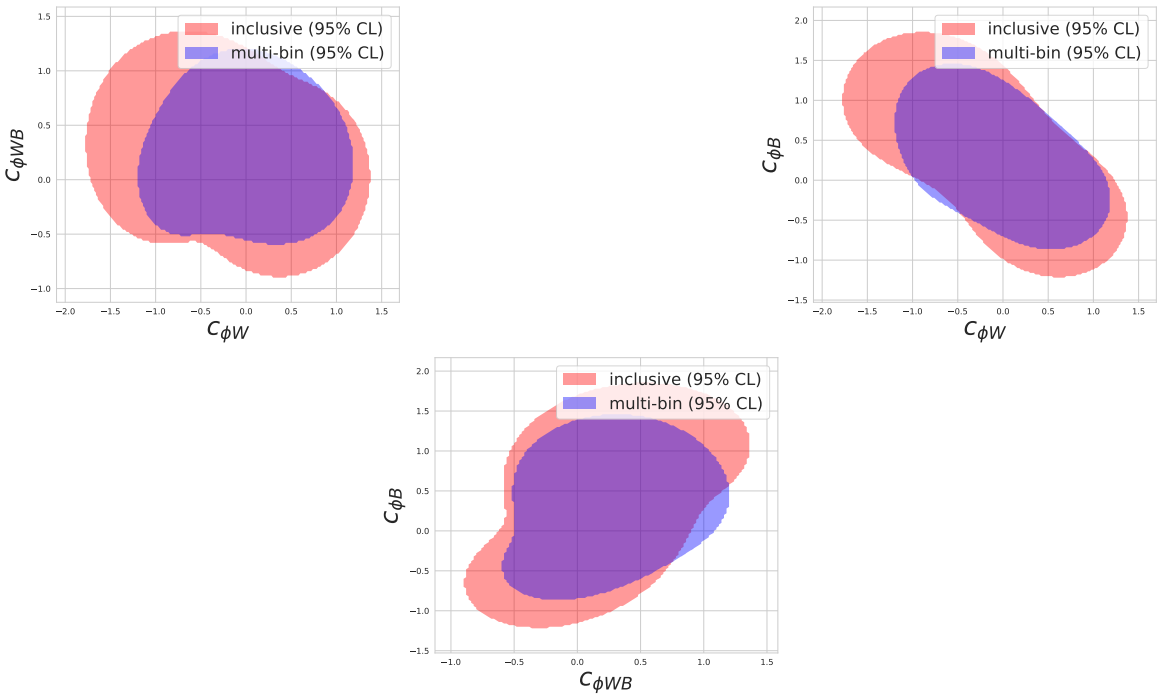


FIGURE 5.2: Two-dimensional 95% CL contours for the Wilson coefficients $C_{\phi W}$, $C_{\phi WB}$, and $C_{\phi B}$ obtained from the $\ell\ell\gamma$ channel using the dominant observable p_T^{γ}. The red regions correspond to the inclusive analysis, while the blue regions represent the multi-bin approach.

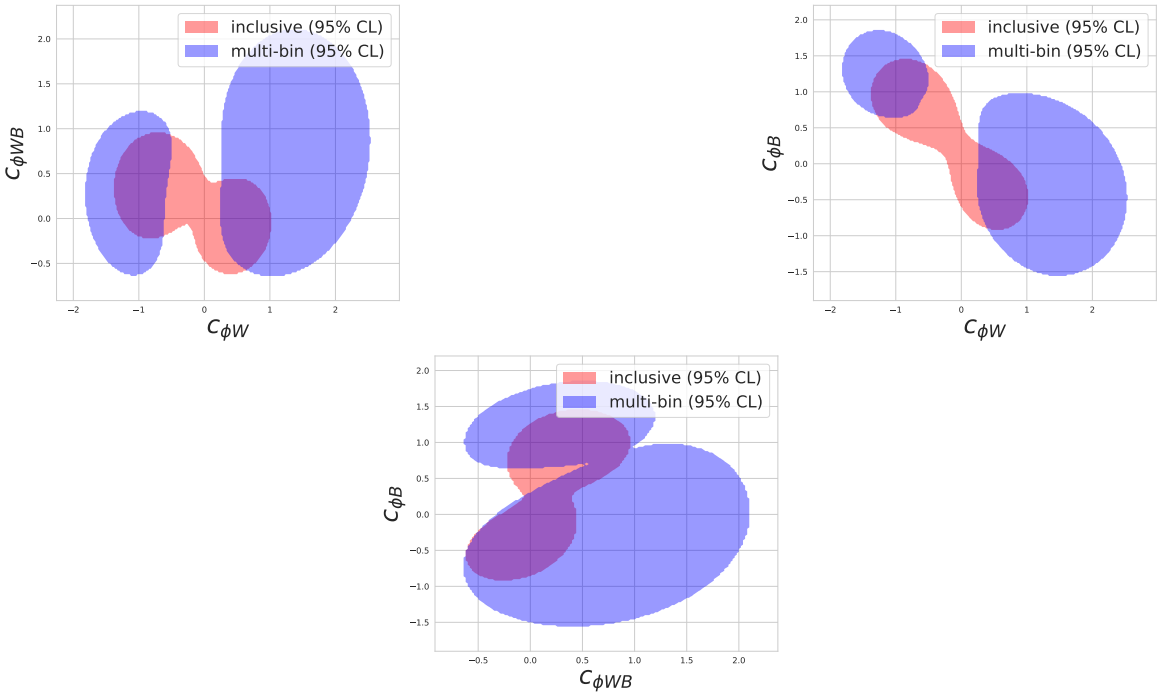


FIGURE 5.3: Two-dimensional 95% CL contours for the Wilson coefficients $C_{\phi W}$, $C_{\phi WB}$, and $C_{\phi B}$ obtained from the $jj\gamma$ channel using the dominant observable p_T^{γ}. The red regions correspond to the inclusive analysis, while the blue regions represent the multi-bin approach.

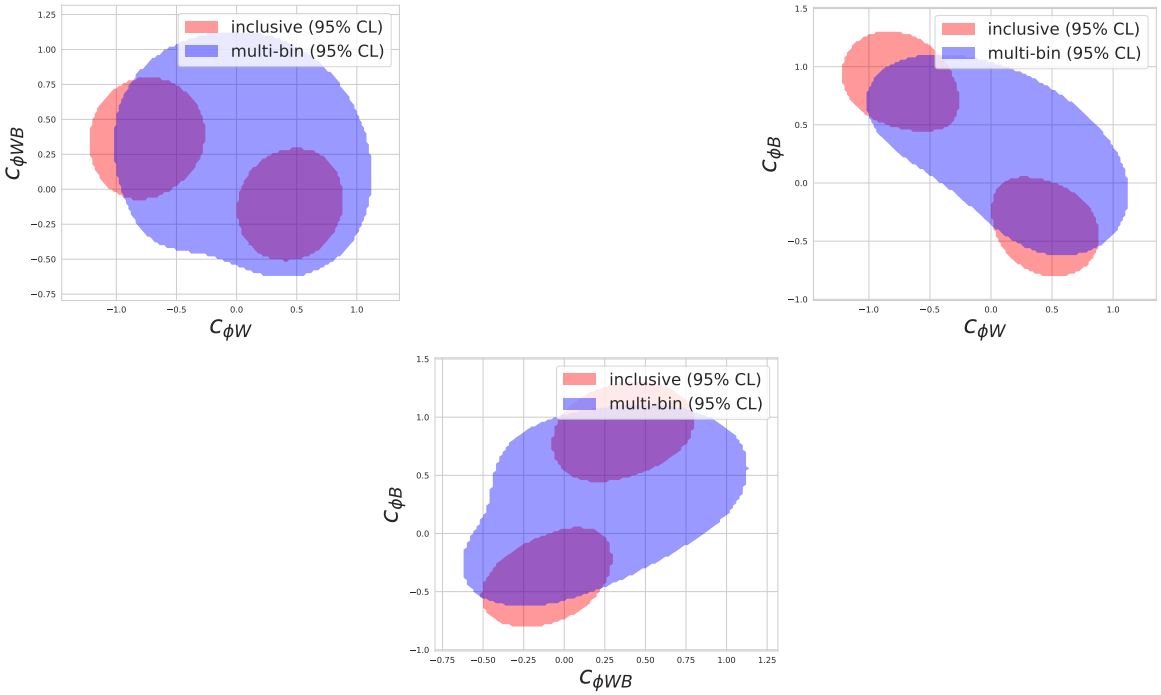


FIGURE 5.4: Two-dimensional 95% CL contours for the Wilson coefficients $C_{\phi W}$, $C_{\phi WB}$, and $C_{\phi B}$ obtained from the $\nu\bar{\nu}\gamma$ channel using the dominant observable $m_T^{(\gamma,\mathrm{MET})}$. The red regions correspond to the inclusive analysis, while the blue regions represent the multi-bin approach.

5.4 Signal and Background Discrimination using Machine Learning

To optimise the signal over background events, minimal cuts are applied, including object and channel-specific selections, based on transverse momentum , invariant masses, pseudorapidity, missing transverse energy and jet reconstruction. The event selections are summarised in Table 5.2.

From appendix B.1 we use the weighted signal and background yields, calculate significance and apply ML (see Figure 5.4). In appendix B.2, we present the feature importance and the correlation matrices of the input variables, with detailed explanations provided in Table B.3, Table B.4 and Table B.5. The normalised distributions that are used as input variables for this analysis and the procedure for hyperparameter

Selection	**Criteria**
Photon requirement	One photon (γ) candidate.
Lepton requirement (ℓ)	Two same-flavour opposite-charge leptons.
Muon (μ) selections	$\lvert\eta^{\mu^\pm}\rvert < 2.7$ and $p_T^{\mu^\pm} > 25$ GeV.
Electron (e) selections	$\lvert\eta^{e^\pm}\rvert < 2.47$, excluding $1.37 < \lvert\eta^{e^\pm}\rvert < 1.52$, with $p_T^{e^\pm} > 25$ GeV.
Photon selections	$\lvert\eta^{\gamma}\rvert < 2.47$, excluding $1.37 < \lvert\eta^{\gamma}\rvert < 1.52$, with $p_T^{\gamma} > 10$ GeV.
Jet reconstruction	anti-k_t algorithm, $R = 0.4$.
Jet–photon separation	Jets within $\Delta R < 0.4$ of any photon are excluded.
Dilepton ($\ell\ell$) mass window	$81 < m_{\ell^+\ell^-} < 101$ GeV.
$Z\gamma$ system	$p_T(Z\gamma) > 50$ GeV.
Photon–lepton separation	$\Delta R(\gamma, \ell) > 0.4$.
Missing transverse energy	$E_T^{\text{miss}} < 40$ GeV.
Channel-specific cuts	
Leptonic ($\ell^+\ell^-\gamma$)	$100 < m_{\ell^+\ell^-\gamma} < 140$ GeV, with $m_{\ell\ell} + m_{\ell^+\ell^-\gamma} > 182$ GeV.
Jet ($jj\gamma$)	$50 < m_{jj\gamma} < 200$ GeV.
Neutrino ($\nu\bar{\nu}\gamma$)	$30 < E_T^{\text{miss}} < 100$ GeV.

TABLE 5.2: Summary of object selections for the three ggF channels.

tuning are explained in appendix B.3.

For the ggF production channels we use the XGBoost classifier and the resulting XGBoost response and ROC curves are shown in Figure 5.5, Figure 5.6, and Figure 5.7. The AUC scores representing the XGboost's ability to separate signal and background events are found to be 92.6%, 93.5% and 96.0%, respectively. This shows that the XGBoost can distinguish the signal from the background without overfitting. From the XGBoost response of the three figures, we consider an XGBoost score of 0.8 to be the best score for separation. The aim is to compare the results obtained using XGBoost with those reported in Ref. [158].

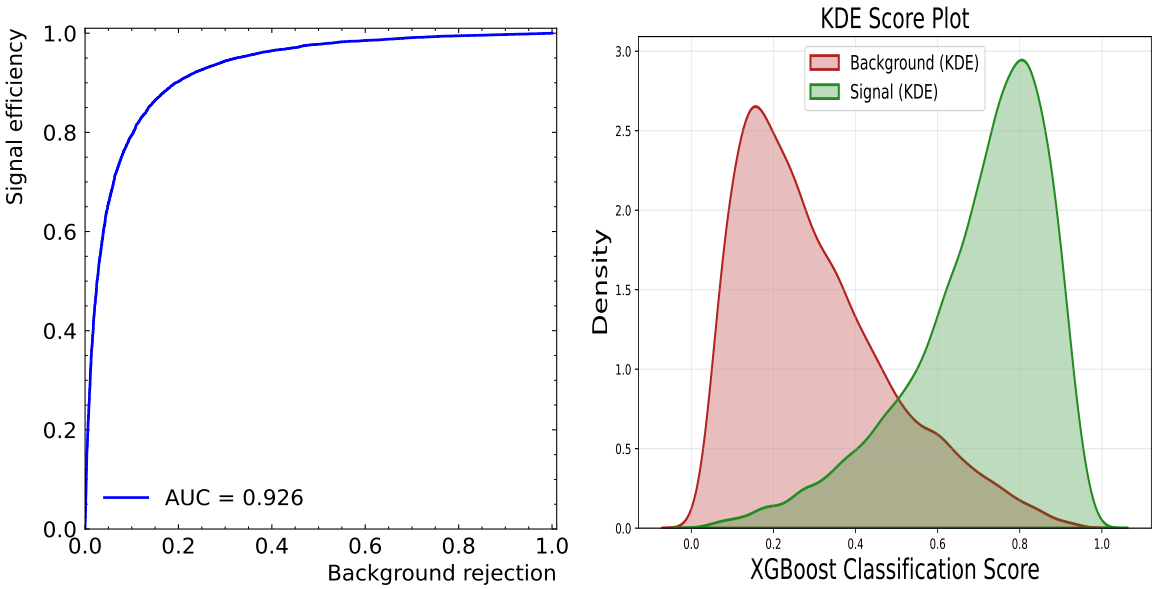


FIGURE 5.5: Comparison of the ROC Curve with its associated AUC score (left), and a KDE plot with XGBoost classification score (right) for the ggF production ($jj\gamma$) channel.

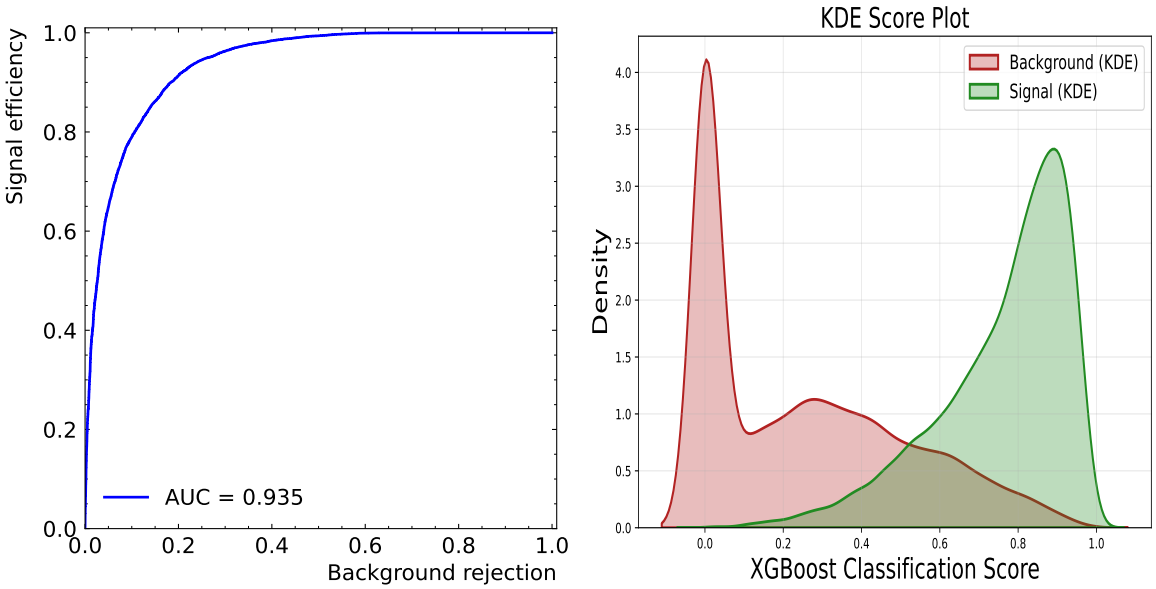


FIGURE 5.6: Comparison of the ROC Curve with its associated AUC score (left), XGBoost classification score (right) for ggF production ($\nu\bar{\nu}\gamma$) channel.

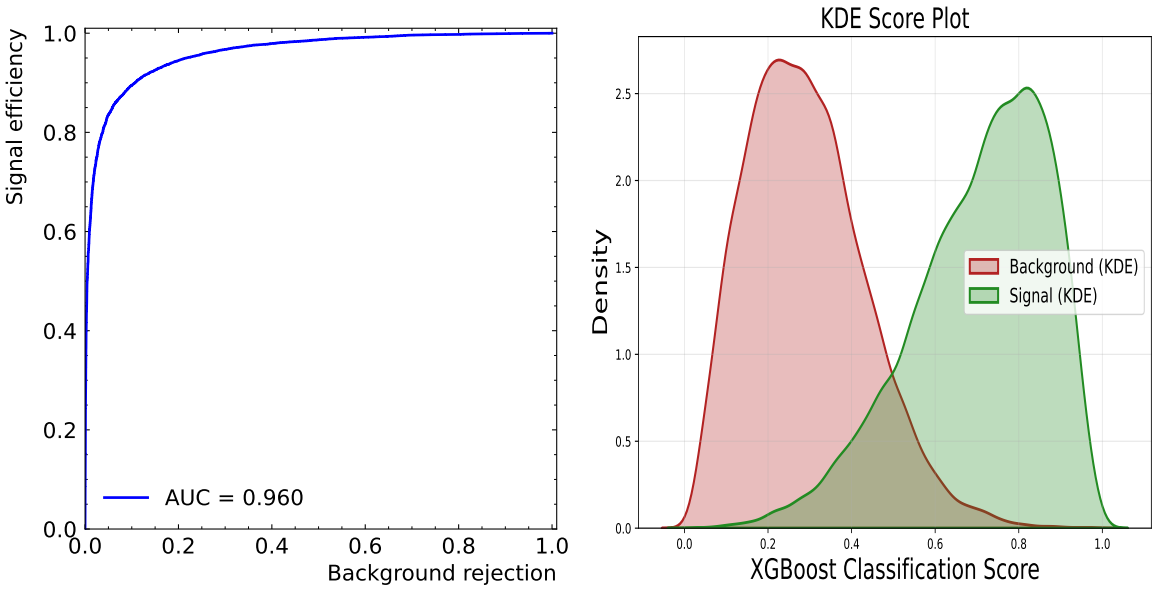


FIGURE 5.7: Comparison of the ROC Curve with its associated AUC score (left), and a KDE plot with XGBoost classification score (right) for the ggF production ($\ell^+\ell^-\gamma$) channel.

Machine Learning model: We calculate Z-scores using the Machine-Learned Likelihood (MLL) method [159, 160], which combines ML classification outputs with likelihood-based inference tests to estimate the experimental sensitivity of high-dimensional data sets. To improve the performance of the method, we further include Kernel Density Estimation (KDE) [161] technique, following the approach outlined in [159]. The MLL+KDE method provides a smooth and continuous approximation of both signal and background probability distributions from MC samples, without requiring explicit binning of classifier outputs. The smoothness of the approximation is controlled by the bandwidth parameter ϵ of the chosen kernel. In our implementation, we adopt the Epanechnikov kernel, defined as:

$$\kappa_\epsilon(u) = \begin{cases} \frac{3}{4\epsilon}\left(1 - \left(\frac{u}{\epsilon}\right)^2\right), & \text{if } |u| \leq \epsilon, \\ 0, & \text{otherwise,} \end{cases} \tag{5.4.1}$$

with $\epsilon = 0.1$ in line with [159]. In practice, bandwidth optimisation (e.g. via cross-validation) plays a crucial role: smaller ϵ values give finer resolution but risk overfitting, while larger values provide smoother approximations but may underfit. In our Python

	Jet	**Neutrino**	**Lepton**
Z (10 bins)	2.69	2.85	3.24
Z (25 bins)	2.81	2.93	3.26
Z (50 bins)	2.87	3.02	3.29
Z (100 bins)	2.95	3.09	3.37
Z (MLL+KDE)	3.22	3.41	3.72

TABLE 5.3: The Z-scores for ggF production channels obtained using binned likelihoods with different binning choices, compared with the MLL+KDE approach.

code, a fixed bandwidth ($\epsilon \approx 0.14$) was also tested, consistent with the methodology. For comparison, we also evaluate the classifier outputs using traditional binned likelihoods. The classifier score $o(x)$ is divided into N_{bins} uniform bins over the range $[0, 1]$, with edges:

$$x_i = \frac{i}{N_{\text{bins}}}, \quad i = 0, 1, \ldots, N_{\text{bins}}, \tag{5.4.2}$$

such that each bin has a width:

$$\Delta x = \frac{1}{N_{\text{bins}}}. \tag{5.4.3}$$

The expected background and signal histograms are normalised to the anticipated event counts (see appendix B.3), and the binned significance is then calculated as:

$$Z = \sqrt{2 \sum_i \left[(S_i + B_i) \ln\left(1 + \frac{S_i}{B_i}\right) - S_i \right]}, \tag{5.4.4}$$

where S_i and B_i denote the normalised bin counts of weighted signal and background yields in the ith bin, respectively. We evaluate Z for $N_{\text{bins}} = 10, 25, 50, 100$. The Z-scores obtained for the ggF production jet, neutrino and lepton channels are summarised in Table 5.3 . As expected, the binned likelihood method improves moderately with finer binning, but the MLL+KDE method consistently outperforms all binning choices by providing a continuous likelihood estimate. This behaviour is further stabilised by ensemble averaging over multiple ML trainings in our implementation, as also suggested in [159].

Chapter 6

Summary and Outlook

6.1 Summary

Building on the motivations discussed in chapter 1, this dissertation presents two complementary studies. The first study investigated diphoton studies in association with leptons and taus, while the second investigated constraining SMEFT Wilson coefficients in $h \to Z\gamma$ decay at the LHC.

The first part of the work explored possible BSM scalar resonances that decay into diphoton final states accompanied by leptons and hadronically decaying tau leptons. The analysis was done using `easyjet` analysis framework on the 2022 Run 3 ATLAS data corresponding to $\mathcal{L} = 35.7$ fb^{-1} at $\sqrt{s} = 13.6$ TeV. We examined the process $gg \to H \to SS'$, particularly on the channels $S \to \gamma\gamma$ and $S' \to [1\ell 1\tau_{\text{had}}, 0\ell 1\tau_{\text{had}}]$ which was motivated by the previously observed multi-lepton anomalies. The signal considered was $\gamma\gamma\tau^+\tau^-$, and the dominant background contributions were from $\gamma\gamma$+multijets, $V\gamma\gamma$ and $t\bar{t}\gamma\gamma$ processes. Standard object selection criteria were applied to isolate events consistent with the target channels (see Table 4.4 and Table 4.5).

After event selection, a multivariate analysis was performed to enhance signal sensitivity. We used correlation matrices to identify the most relevant kinematic variables to use as input features for DNN training to distinguish signal from background. To optimise the DNN performance we used feature ranking to assess the relative importance of each variable. The DNN output was subsequently used to maximise the signal significance and to evaluate potential excesses consistent with the new scalar in the ATLAS data, but ultimately, we did not reach a significance required for a conclusive discovery.

The second part of the dissertation examined the rare Higgs boson decay $h \to Z\gamma$, which occurs at NLO order in the SM. The XGboost classifier was used to improve separation of signal from background across multiple Higgs production modes, such as ggF leptonic, jet and neutrino channels. We used the KDE to quantify statistical differences between signal and background distributions within SMEFT, to constrain the six-dimensional Wilson coefficients and potential deviations from SM predictions. Overall, the work integrated theoretical modelling, simulation and modern ML methods to improve the understanding of Higgs boson properties. Our results indicate that the KDE improves with larger ensemble sizes because it avoids output binning, while the binning method benefits from increased bin counts; KDE consistently outperforms binning.

6.2 Future Work

Future developments of this work will focus on a comprehensive characterisation of the background and signal modelling. Several data-driven techniques will be compared for estimating the background contribution in signal region, including the two-dimensional (2D) sideband, template-fit, fake-factor, and TMVA-based multivariate methods. In regions where there is absence of a significant signal, fits will be performed to the sidebands. Normalisation factors will be derived from these regions, using alternative functional forms such as exponential and polynomial parameterisations to model the background. The most appropriate function will be chosen by evaluating the degrees of freedom and the size of any spurious signal. A χ^2 test may also be used to quantify the accuracy of fit. The goal is to select the simplest model that provides an adequate description of the data with minimal spurious signal.

The background characterisation will also involve determining the scale factors used to normalise individual background components. Multiple kinematic distributions, including p_T, $m_{\gamma\gamma}$, $V_{\gamma\gamma}$ and $\gamma\gamma$+jets variables, will be overlaid and compared between data and MC to validate these scale factors. This study will serve as an input to the final background model and its associated systematic uncertainty. To evaluate the impact of potential signal contamination in the background model, a spurious signal test will be performed. For each mass hypothesis between 130 and 200 GeV, in 5 GeV intervals, the fitted signal yield at a given mass point (e.g, 152 GeV) will be extracted

and treated as the spurious signal. The maximum spurious yield across the mass range will be taken as the systematic uncertainty.

For the signal modelling, a double-sided Crystal Ball function will be used. The evolution of the shape parameters, particularly α across the simulated mass points, will be studied, and functional forms for their analytical modelling will be investigated. Finally, dedicated control regions will be defined to constrain background normalisations and validate the modelling. The invariant-mass window around 125 GeVwill remain blinded during this stage of the study.

We will extend the second project to the VBF, $t\bar{t}H$ and VH production channels, assessing performance both before and after optimisation using each channel's key features. We also plan to compare the performance of a BDT classifier against XGBoost to explore operator structures not fully accessible in a single production mechanism. These steps will collectively provide a more comprehensive probe of electroweak interactions and possible new physics effects within SMEFT using the rare $h \to Z\gamma$ decay channel. The analyses will further benefit from the larger Run 3 datasets and improved detector calibrations, which are expected to enhance statistical precision and overall sensitivity to new scalar resonances and SMEFT effects.

Appendix A

Diphoton studies in association with leptons

A.1 MC Event Weighting

For each MC event e belonging to a simulated sample s, the total event weight w_e applied in the analysis is defined as:

$$w_e = w_e^{\text{gen}} \times w_e^{\text{PU}} \times w_e^{\text{JVT}}. \tag{A.1.1}$$

The factor w_e^{gen} corresponds to the generator weight assigned by the event generator and represents the per-event contribution to the theoretical cross section. In NLO samples, these weights may be either positive or negative due to the subtraction of higher-order corrections. The term w_e^{PU} accounts for pileup reweighting and is introduced to correct for differences in the number of simultaneous pp interactions between data and simulation. This correction ensures that the distribution of reconstructed vertices and other pileup-dependent observables in simulation accurately reflects the distributions observed in recorded data. The factor w_e^{JVT} represents the Jet Vertex Tagger (JVT) efficiency scale factor, which compensates for small residual mismodelling in the efficiency of identifying jets.

No explicit normalisation to the integrated luminosity or sample cross section is applied in this formulation, as the weighting is limited to event-level corrections rather than overall yield scaling. The weights are taken directly from the analysis trees through the branches `generatorWeight`, `PileupWeight`, and `jvt_effSF`, corresponding respectively to w_e^{gen}, w_e^{PU}, and w_e^{JVT}. The resulting per-event total weight can

therefore be expressed as:

$$w_e = w_e^{\text{gen}} \times w_e^{\text{PU}} \times w_e^{\text{JVT}} \tag{A.1.2}$$

and is stored as total weight in the output samples for use in histogram weighting and significance calculations.

A.2 Correlation Matrices

To optimise the DNN model and be able to choose the input features for the DNN we used the correlation between the variables and chose the least correlated variables. Figure A.1 and Figure A.2 show the correlation matrices for the $\gamma\gamma + 1\ell 1\tau_{\text{had}}$ and $\gamma\gamma + 0\ell 1\tau_{\text{had}}$ channels respectively.

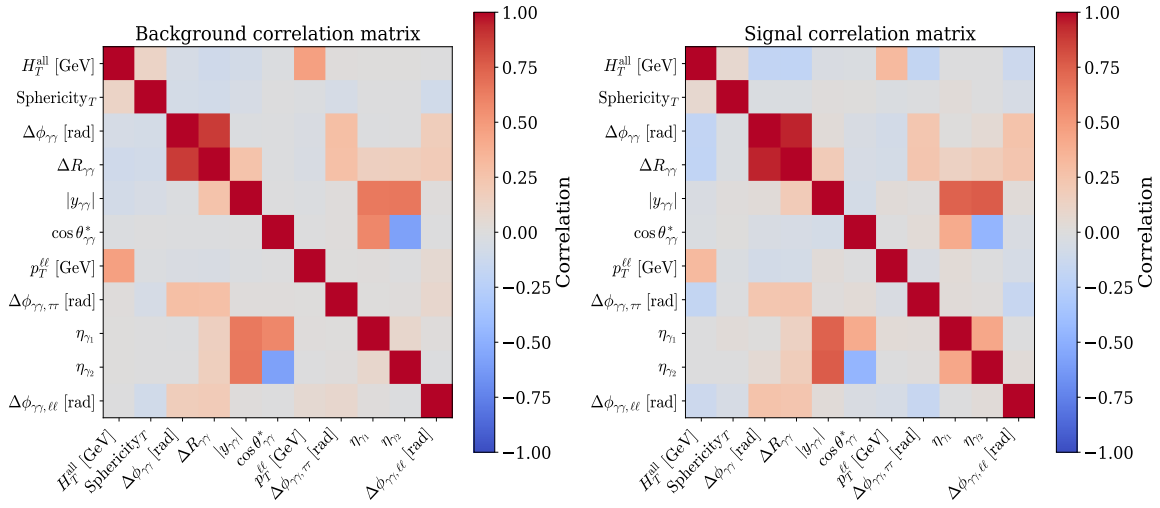


FIGURE A.1: Signal and Background correlation matrices for the $\gamma\gamma + 1\ell 1\tau_{\text{had}}$ channel.

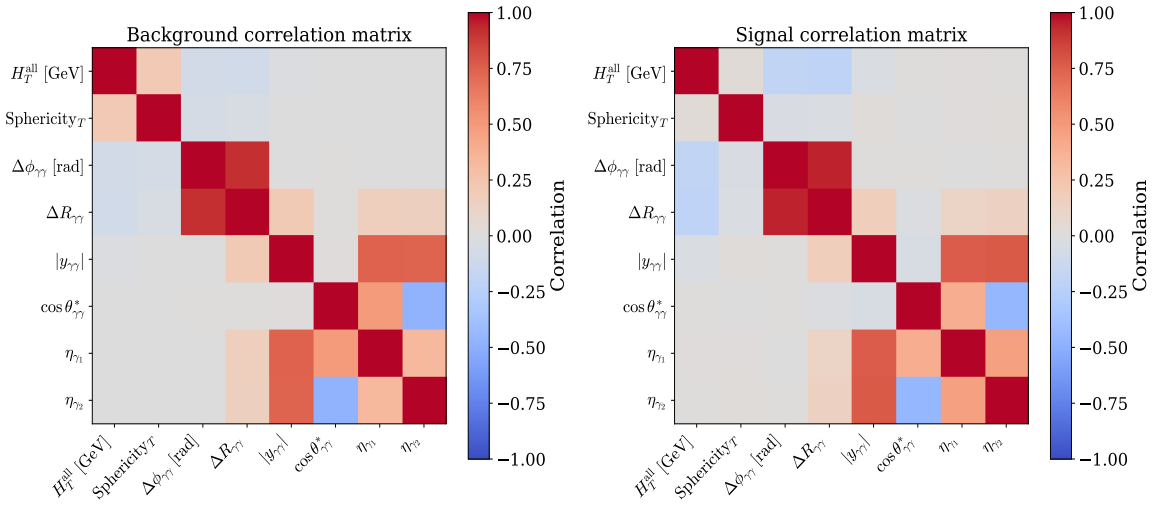


FIGURE A.2: Signal and Background correlation matrices for the $\gamma\gamma + 0\ell 1\tau_{\text{had}}$ channel.

A.3 Input Features for DNN

The DNN used in this analysis is implemented as a fully connected multilayer perceptron with an input dimension of d_{in}. The architecture consists of three hidden layers with 20, 15, and 10 neurons, respectively. Each layer applies a linear transformation followed by batch normalisation and a Rectified Linear Unit (ReLU) activation function [162]. To mitigate overfitting, we applied dropout after each hidden layer with rates of 0.2, 0.2, and 0.1. The output layer comprises a single node, providing a continuous output between 0 and 1 corresponding to an event being classified as signal or background.

The model is trained using the AdamW optimiser [163] for up to 100 epochs, with a mini-batch size of 128. The binary cross-entropy loss function [164] is defined as:

$$-f(y_{\text{true}}, y_{\text{pred}}) = y_{\text{true}} \log(y_{\text{pred}}) + (1 - y_{\text{true}}) \log(1 - y_{\text{pred}}), \tag{A.3.1}$$

where y_{pred} is the probability assigned by the DNN for an event being signal or background, and y_{true} is the actual class label (1 for signal, 0 for background). Early stopping is used to prevent overtraining by monitoring the validation loss, with a patience of five epochs. The model achieving the lowest validation loss is saved and used

for evaluation. The dataset is divided into 70% for training, 20% for testing, and 10% for validation. A grid search is performed to optimise the learning rate for each channel, yielding optimal values of 3×10^{-4} for the $\gamma\gamma + 0\ell 1\tau_{\text{had}}$ channel and 1×10^{-4} for the $\gamma\gamma + 1\ell 1\tau_{\text{had}}$ channel.

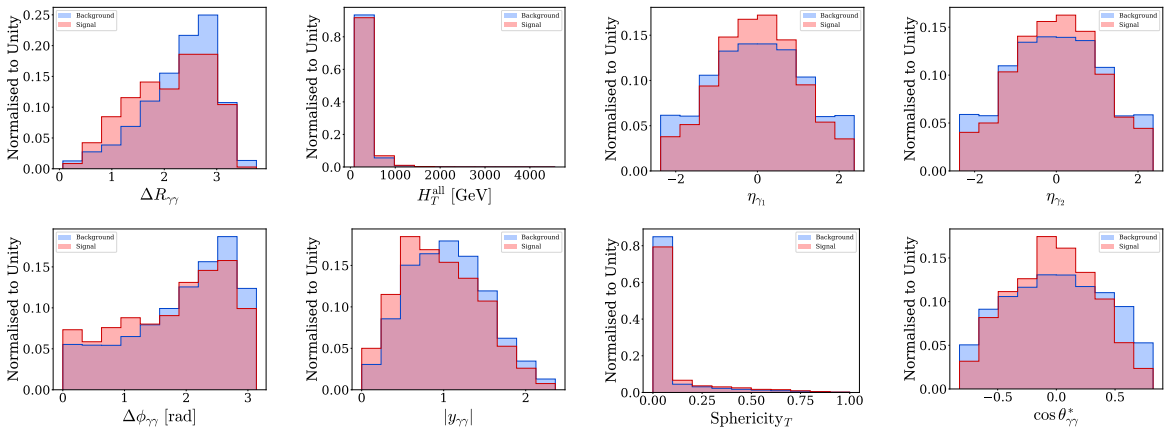


FIGURE A.3: Normalised distributions of key kinematic observables used in the $\gamma\gamma + 0\ell 1\tau_{\text{had}}$ channel.

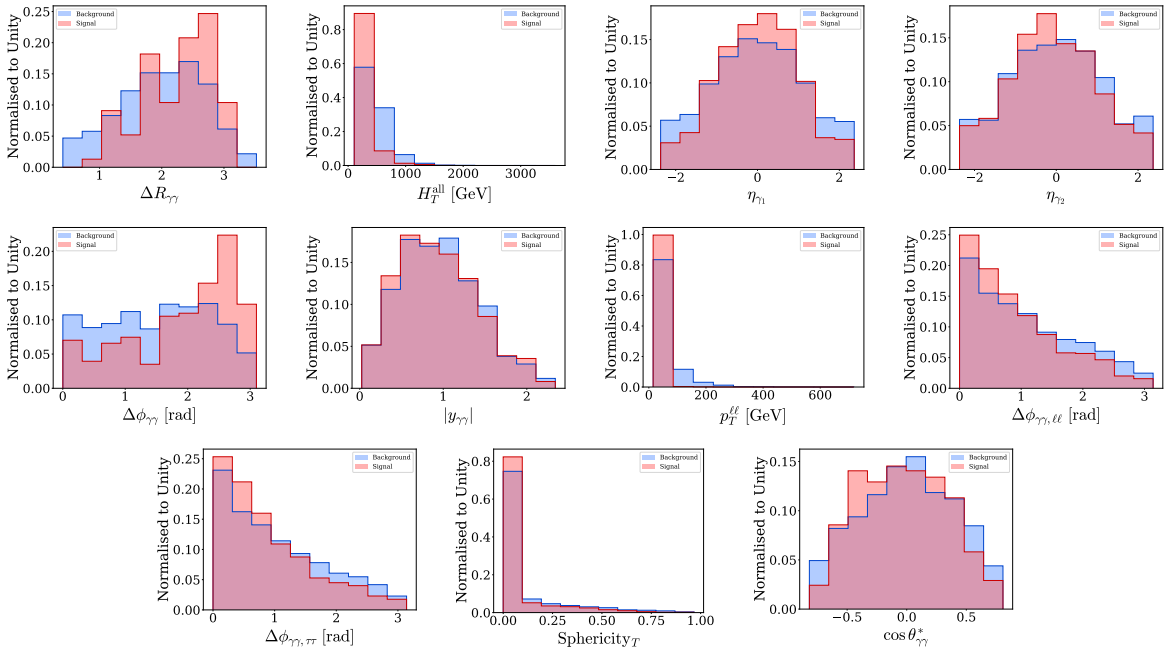


FIGURE A.4: Normalised distributions of key kinematic observables used in the $\gamma\gamma + 1\ell 1\tau_{\text{had}}$ channel.

Appendix B

Applications of Machine Learning Techniques in $h \to Z\gamma$

B.1 Cross-sections and weights

The generated samples are weighted to the corresponding cross-sections with integrated luminosity $\mathcal{L} = 140$ fb^{-1}. Table B.1 and Table B.2 summarise the cross-sections and weights used for the ggF production channels, respectively.
The event weights for the signal and background samples are calculated as follows:

$$w_{\text{bkg}} = \frac{\sigma_{\text{SM+bkg}} \times \mathcal{L}}{N_{\text{gen}}}, \tag{B.1.1}$$

and

$$w_{\text{sig}} = \frac{\sigma_{\text{sig}} \times \mathcal{L}}{N_{\text{gen}}}, \tag{B.1.2}$$

where $\sigma_{\text{SM+bkg}}$ and σ_{sig} are cross-sections for background and signal samples, respectively, and N_{gen} is the number of generated MC events.

Channel	Type	Cross-section (pb)
$\nu\bar{\nu}\gamma$	Signal	25.71
	SM	$0.0019 \pm 1.4 \times 10^{-6}$
	Background	13.97 ± 0.182
$\ell^+\ell^-\gamma$	Signal	8.605 ± 0.0032
	SM	$0.0006 \pm 6.942 \times 10^{-6}$
	Background	18.14 ± 0.0124
$jj\gamma$	Signal	86.19 ± 0.0323
	SM	$0.0049 \pm 4.074 \times 10^{-5}$
	Background	$7.934 \times 10^4 \pm 638.3$

TABLE B.1: Cross-section results for ggF production channels and their uncertainties.

	Leptonic	Jet	Neutrino
Background Events passing all cuts	428 010	210 125	192 425
Signal Events passing all cuts	80 000	92 000	95 000
Background Weights	25.442	13.001	1.474
Signal Weights	0.132	0.045	0.015
Weighted Background Events	10 889 387.62	2 731 751.08	283 567.10
Weighted Signal Events	10 520	4 134.48	1 425

TABLE B.2: Event counts, weights, and weighted event yields are summarised for the leptonic, jet and neutrino channels, with selection criteria detailed in Table 5.2.

B.2 Feature Importance and Correlation Matrices

After generating the MC samples, we used a random forest classifier (Figure B.3, Figure B.1 and Figure B.2) and correlation matrices (Figure B.4, Figure B.5 and Figure B.6) to choose the sensitive kinematics for our study and used the kinematics with the highest importance to optimise the model.

Variable	**Description**
n_{leps}	Number of leptons.
$m_{\ell\ell}$	Leptons invariant mass.
$p_T^{\ell\ell\gamma}$	The $\ell\ell\gamma$ system transverse momentum.
$p_T^{\ell_1}$, η_{ℓ_1}, ϕ_{ℓ_1}	Leading lepton transverse momentum, pseudorapity and azimuthal angle.
η_{ℓ_2}, $p_T^{\ell_2}$, ϕ_{ℓ_2}	Subleading lepton pseudorapidity, tranverse momentum and azithmutal angle.
$p_T$ratio	Transverse momentum ratio.
$\Delta\eta_{\ell\ell}$	Pseudorapidity separation between the two leptons.
$\Delta\phi_{\ell\ell}$	Azimuthal separation between the two leptons.
$\Delta R_{\gamma,\ell_1}$	Angular distance between the photon and the leading lepton.
$\Delta R_{\gamma,\ell_2}$	Angular distance between the photon and the subleading lepton.
$\Delta\phi_{Z,\gamma}$	Azimuthal separation between Z boson and photon.
$\Delta\eta_{Z,\gamma}$	Pseudorapidity separation between Z boson and photon.
p_{Tt}	Transverse thrust variable (component of p_T perpendicular to the $Z\gamma$ axis).
p_T^{γ}	Photon transverse momentum.
ϕ_{γ}	Photon azimuthal angle.
η_{γ}	Photon pseudorapidity.

TABLE B.3: Variables used as inputs to the XGBoost, with respect to Ref. [132] in $\ell^+\ell^-\gamma$ channel.

Variable	**Description**
m_{jj}	Jets invariant mass.
η_{j1}, ϕ_{j1}, p_T^{j1}	Pseudorapidity, azimuth and leading jet transverse momentum.
η_{j2}, ϕ_{j2}, p_T^{j2}	Pseudorapidity, azimuth and subleading jet transverse momentum.
p_T^{γ}, η_{γ}, ϕ_{γ}	Photon candidate: transverse momentum, pseudorapidity and azimuth.
$p_T$ratio	Event-level transverse momentum ratio (dimensionless.)
$p_T\text{ratio}^{jj}$	Dijet transverse momentum ratio (dimensionless).
p_T^{jj}	Dijet system transverse momentum.
$\Delta\eta_{jj}$	Pseudorapidity separation between jets.
$\Delta\phi_{jj}$	Azimuthal separation between jets.
$\Delta R_{\gamma,j1}$	Angular distance between photon and leading jet.
$\Delta R_{\gamma,j2}$	Angular distance between photon and subleading jet.
$\Delta\phi_{Z,\gamma}$	Azimuthal separation between Z system and photon.
$\Delta\eta_{Z,\gamma}$	Pseudorapidity separation between the Z system and the photon.
p_{Tt}	Transverse thrust-like variable: component of p_T perpendicular to the $Z\gamma$ axis.
$\cos\theta_Z$	Angular structure variable.

TABLE B.4: Variables used as XGboost inputs in $jj\gamma$ channel.

Variable (math)	Description
$\phi(E_T^{\text{miss}})$	Azimuthal angle of missing transverse energy $\vec{E}_T^{\text{miss}}$ (rad).
$\Delta\phi_{\gamma,\text{MET}}$	Azimuthal separation between leading photon and $\vec{E}_T^{\text{miss}}$ (rad).
$p_T^{\gamma_1}$	Leading photon transverse momentum (GeV).
ϕ_{γ_1}	Leading photon azimuthal angle (rad).
η_{γ_1}	Leading photon pseudorapidity.
E_T^{miss}	Magnitude of the missing transverse energy (GeV).
$p_T$ratio	Event–level transverse momentum ratio (dimensionless).
$p_T$balance	Transverse balance of γ and MET (dimensionless).
m_T^{recoil}	Recoil transverse mass built from $\vec{p}_T^{\gamma_1}$ and $\vec{E}_T^{\text{miss}}$ (GeV).
$m_{\nu\bar{\nu}}$	Invariant mass of the neutrino system (GeV); truth–level or reconstructed proxy depending on sample.
$\Delta\phi_{\nu\bar{\nu}}$	Azimuthal separation between the two neutrinos (rad); truth–level in MC.
$m_T^{(\gamma,\text{MET})}$	Transverse mass of the γ–MET system (GeV).

TABLE B.5: Variables used as XGboost inputs in $\nu\bar{\nu}\gamma$ channel.

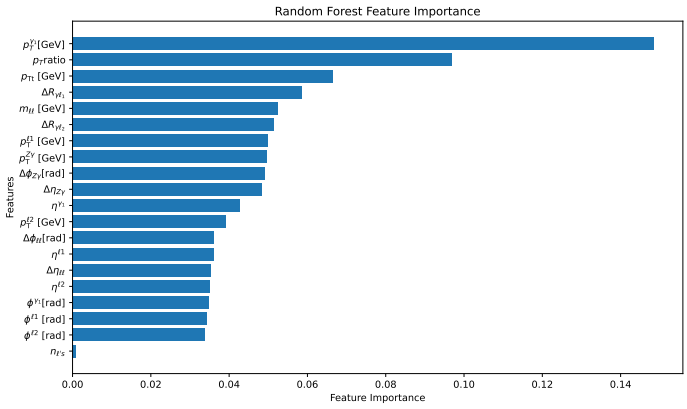


FIGURE B.1: Feature importance for ggF production ($\ell^+\ell^-\gamma$) channel.

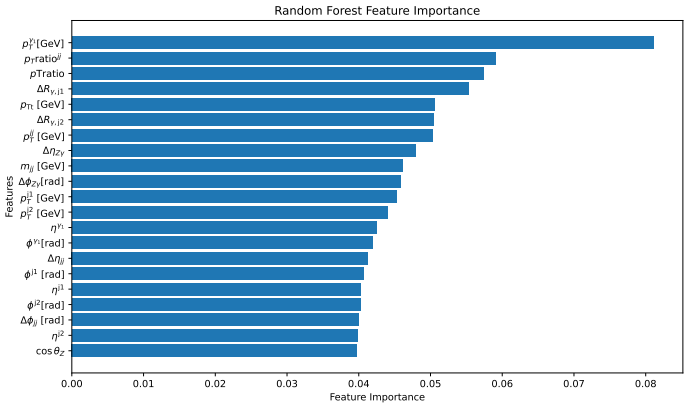


FIGURE B.2: Feature importance for ggF production ($jj\gamma$) channel.

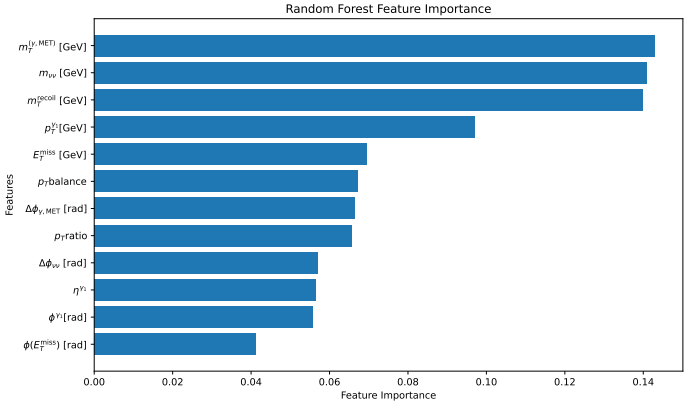


FIGURE B.3: Feature importance for ggF production ($\nu\bar{\nu}\gamma$) channel.

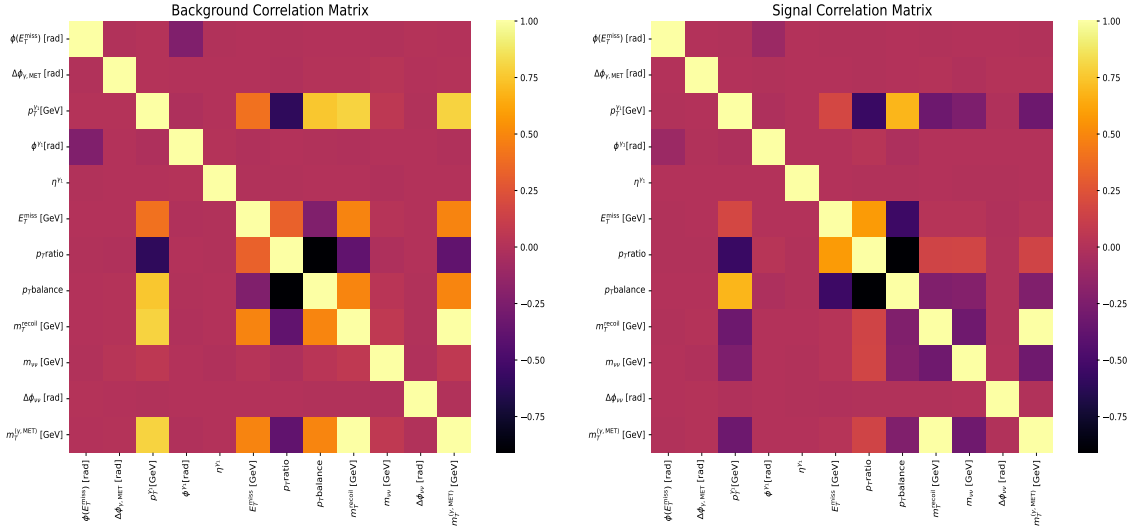


FIGURE B.4: Signal and Background correlation matrix of the ggF production ($\nu\bar{\nu}\gamma$) channel.

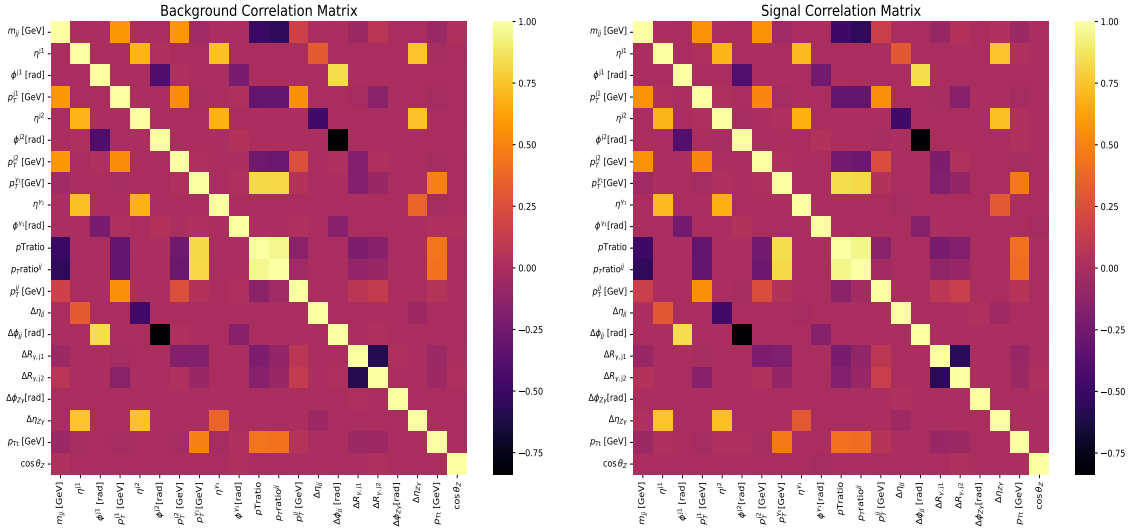


FIGURE B.5: Signal and Background correlation matrix of the ggF production ($jj\gamma$) channel.

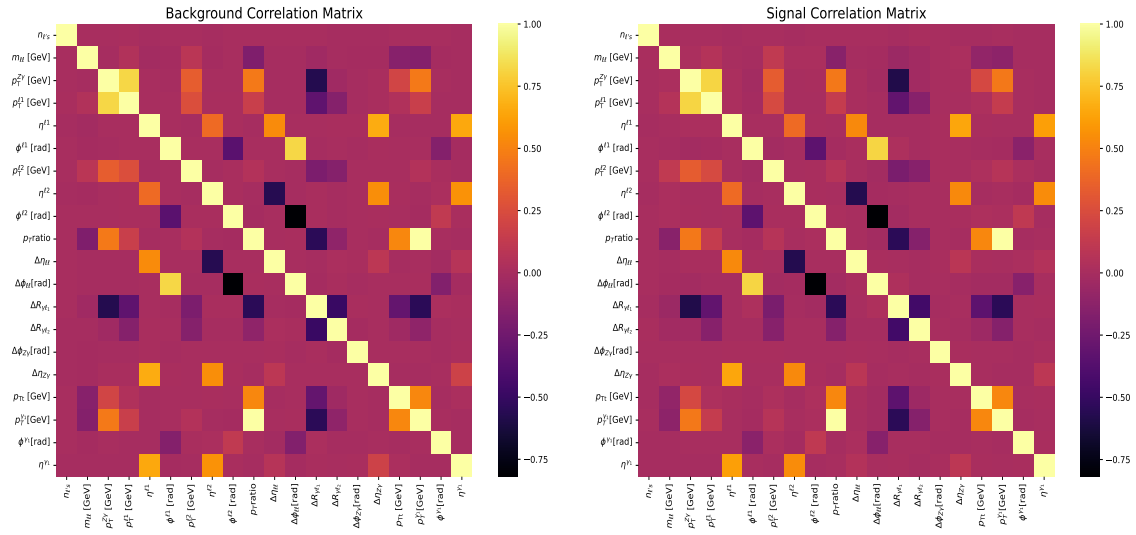


FIGURE B.6: Signal and Background correlation matrix of the ggF production ($\ell^+\ell^-\gamma$) channel.

B.3 XGboost training and Normalised Distributions

The XGBoost which is the implementation of the Boosted Decision Trees (BDT) model that uses second-order optimisation was used. Unlike traditional BDTs that only use first-order gradients, XGBoost takes advantage of both gradients and Hessians for better convergence. This method includes Lasso and Ridge regularisation set to 0.0001 to prevent overfitting. We have also added a `gamma` parameter to control the minimum reduction in loss required for making additional splits in the trees. The performance of the trained MC-simulated samples was assessed using the MLL+ KDE [161] and the normalised distributions used in the ggF production channels are shown in Figure B.7, Figure B.8 and Figure B.9.

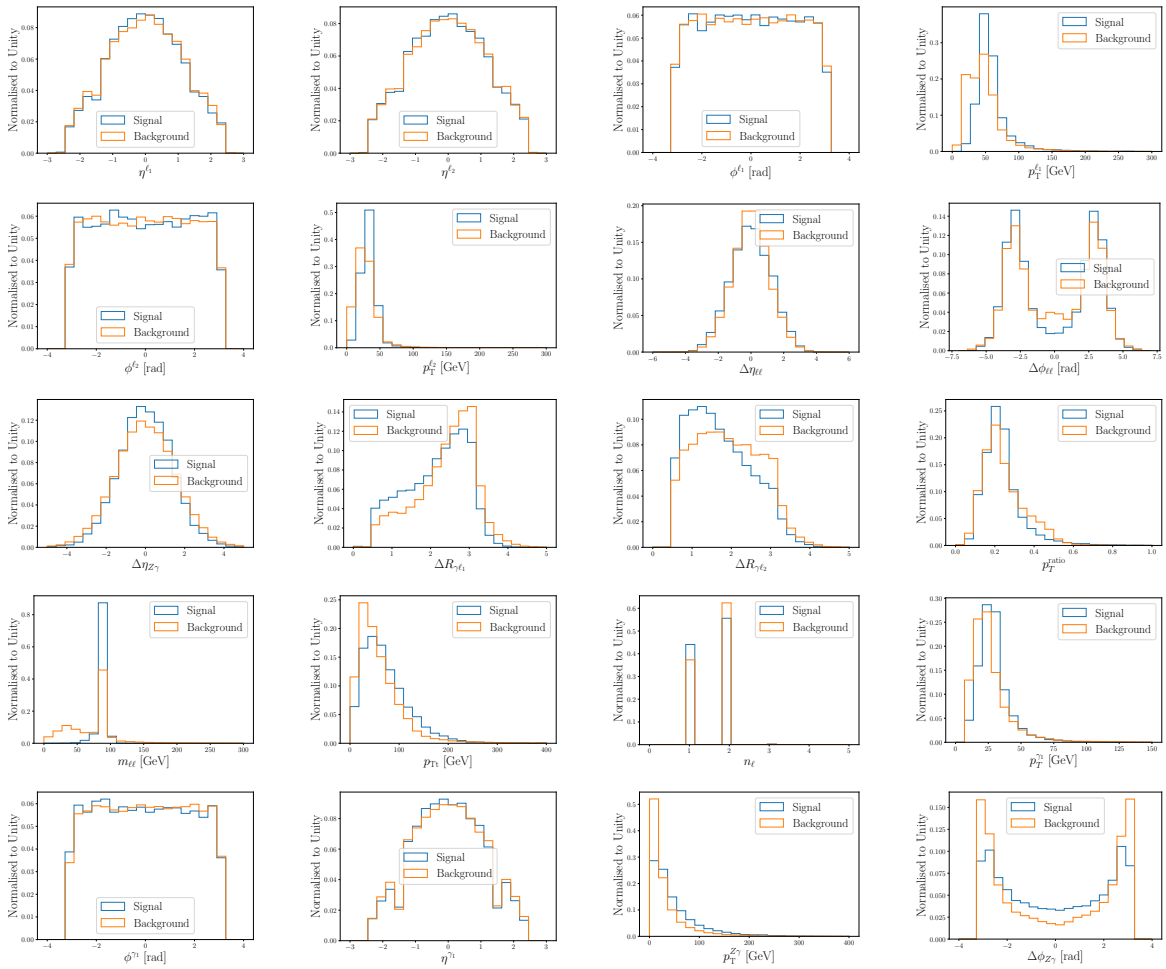


FIGURE B.7: Normalised distributions of key kinematic observables used in the ggF production ($\ell^+\ell^-\gamma$) channel to distinguish signal from background events.

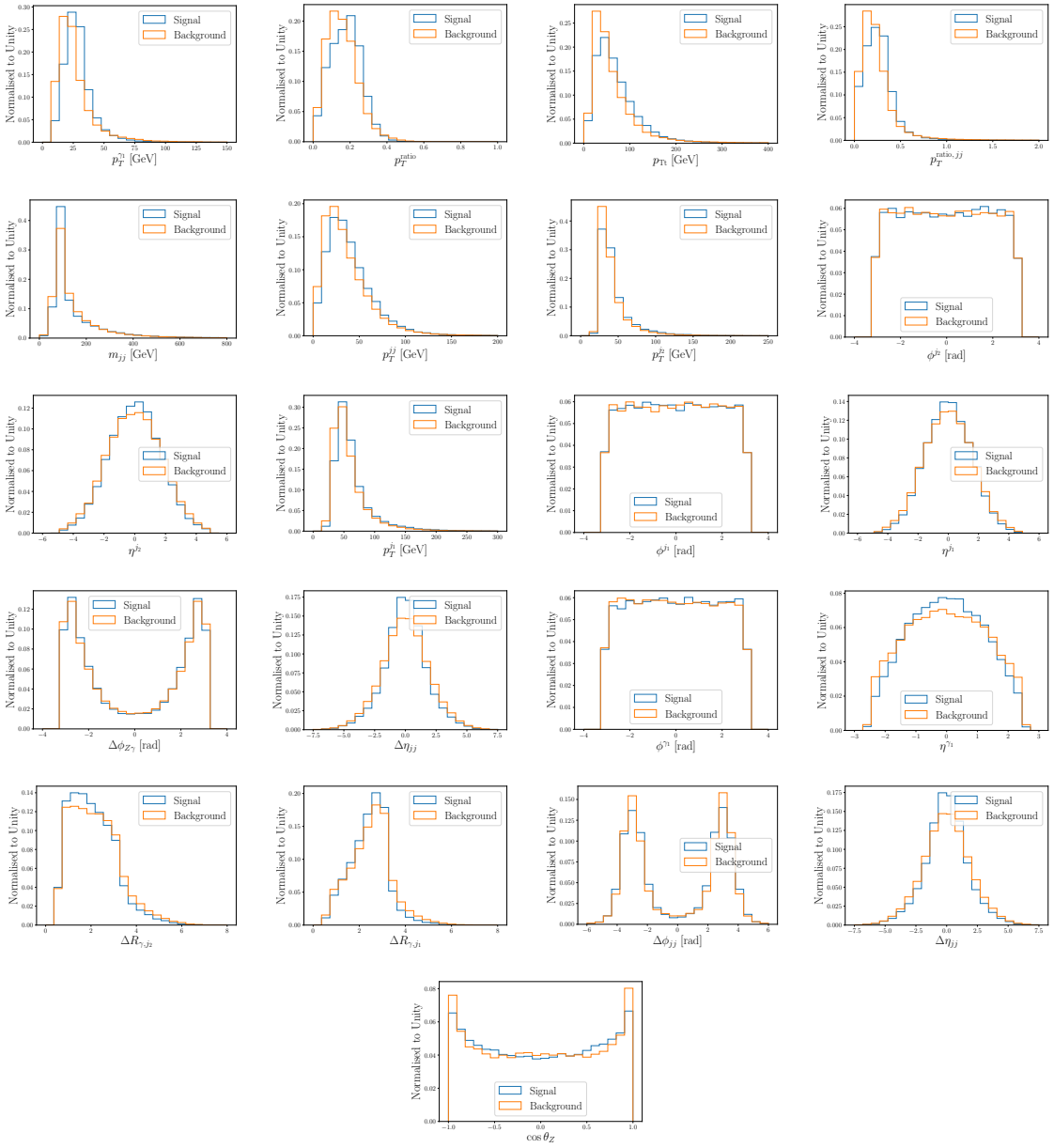


FIGURE B.8: Normalised distributions of key kinematic observables used in the ggF production ($jj\gamma$) channel to distinguish signal from background events.

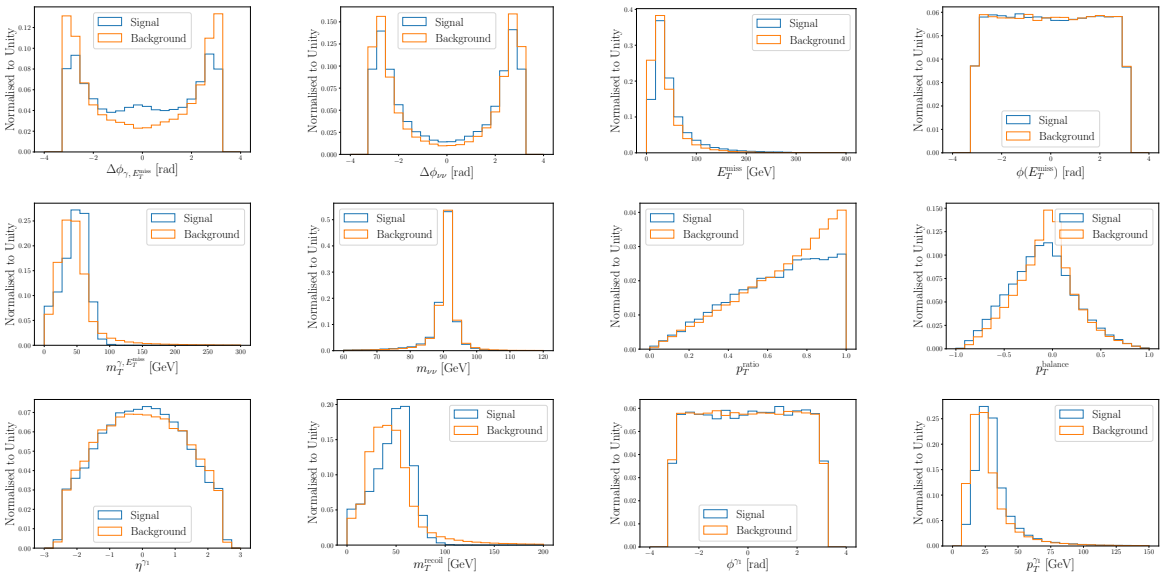


FIGURE B.9: Normalised distributions of key kinematic observables used in the ggF production ($\nu\bar{\nu}\gamma$) channel to distinguish signal from background events.

Bibliography

[1] Mary K. Gaillard, Paul D. Grannis, and Frank J. Sciulli. "The standard model of particle physics". In: *Rev. Mod. Phys.* 71 (2 Mar. 1999), S96–S111. DOI: 10.1103/RevModPhys.71.S96. URL: https://link.aps.org/doi/10.1103/RevModPhys.71.S96.

[2] Georges Aad et al. "Observation of a new particle in the search for the Standard Model Higgs boson with the ATLAS detector at the LHC". In: *Phys. Lett. B* 716 (2012), pp. 1–29. DOI: 10.1016/j.physletb.2012.08.020. arXiv: 1207.7214 [hep-ex].

[3] Serguei Chatrchyan et al. "Observation of a New Boson at a Mass of 125 GeV with the CMS Experiment at the LHC". In: *Phys. Lett. B* 716 (2012), pp. 30–61. DOI: 10.1016/j.physletb.2012.08.021. arXiv: 1207.7235 [hep-ex].

[4] Serguei Chatrchyan et al. "Observation of a New Boson with Mass Near 125 GeV in pp Collisions at $\sqrt{s} = 7$ and 8 TeV". In: *JHEP* 06 (2013), p. 081. DOI: 10.1007/JHEP06(2013)081. arXiv: 1303.4571 [hep-ex].

[5] ATLAS Collaboration. "The ATLAS Experiment at the CERN Large Hadron Collider". In: *Journal of Instrumentation* 3.08 (Aug. 2008), S08003. DOI: 10.1088/1748-0221/3/08/S08003. URL: https://doi.org/10.1088/1748-0221/3/08/S08003.

[6] CMS Collaboration. "The CMS Experiment at the CERN LHC". In: *Journal of Instrumentation* 3.08 (Aug. 2008), S08004. DOI: 10.1088/1748-0221/3/08/S08004. URL: https://doi.org/10.1088/1748-0221/3/08/S08004.

[7] Stefan von Buddenbrock et al. "Phenomenological signatures of additional scalar bosons at the LHC". In: *Eur. Phys. J. C* 76.10 (2016), p. 580. DOI: 10.1140/epjc/s10052-016-4435-8. arXiv: 1606.01674 [hep-ph].

[8] Stefan von Buddenbrock et al. "Multi-lepton signatures of additional scalar bosons beyond the Standard Model at the LHC". In: *J. Phys. G* 45.11 (2018), p. 115003. DOI: 10.1088/1361-6471/aae3d6. arXiv: 1711.07874 [hep-ph].

[9] Stefan Buddenbrock et al. "The emergence of multi-lepton anomalies at the LHC and their compatibility with new physics at the EW scale". In: *JHEP* 10 (2019), p. 157. DOI: 10.1007/JHEP10(2019)157. arXiv: 1901.05300 [hep-ph].

[10] Stefan von Buddenbrock, Richard Ruiz, and Bruce Mellado. "Anatomy of inclusive $t\bar{t}W$ production at hadron colliders". In: *Phys. Lett. B* 811 (2020), p. 135964. DOI: 10.1016/j.physletb.2020.135964. arXiv: 2009.00032 [hep-ph].

[11] Yesenia Hernandez et al. "The anomalous production of multi-lepton and its impact on the measurement of Wh production at the LHC". In: *Eur. Phys. J. C* 81.4 (2021), p. 365. DOI: 10.1140/epjc/s10052-021-09137-1. arXiv: 1912.00699 [hep-ph].

[12] Sumit Banik et al. "Uncovering new Higgses in the LHC analyses of differential $t\bar{t}$ cross sections". In: *JHEP* 01 (2025), p. 155. DOI: 10.1007/JHEP01(2025)155. arXiv: 2308.07953 [hep-ph].

[13] Guglielmo Coloretti, Andreas Crivellin, and Bruce Mellado. "Combined explanation of LHC multilepton, diphoton, and top-quark excesses". In: *Phys. Rev. D* 110.7 (2024), p. 073001. DOI: 10.1103/PhysRevD.110.073001. arXiv: 2312.17314 [hep-ph].

[14] Andreas Crivellin and Bruce Mellado. "Anomalies in particle physics and their implications for physics beyond the standard model". In: *Nature Rev. Phys.* 6.5 (2024), pp. 294–309. DOI: 10.1038/s42254-024-00703-6. arXiv: 2309.03870 [hep-ph].

[15] Andreas Crivellin et al. "Accumulating evidence for the associated production of a new Higgs boson at the LHC". In: *Phys. Rev. D* 108.11 (2023), p. 115031. DOI: 10.1103/PhysRevD.108.115031. arXiv: 2109.02650 [hep-ph].

[16] Srimoy Bhattacharya et al. "Growing Excesses of New Scalars at the Electroweak Scale". In: (June 2023). arXiv: 2306.17209 [hep-ph].

[17] Srimoy Bhattacharya et al. “Emerging Excess Consistent with a Narrow Resonance at 152 GeV in High-Energy Proton-Proton Collisions”. In: (Mar. 2025). arXiv: 2503.16245 [hep-ph].

[18] Albert M Sirunyan et al. “Measurements of Higgs boson production cross sections and couplings in the diphoton decay channel at $\sqrt{s} = 13$ TeV”. In: *JHEP* 07 (2021), p. 027. DOI: 10.1007/JHEP07(2021)027. arXiv: 2103.06956 [hep-ex].

[19] Georges Aad et al. “Measurement of the properties of Higgs boson production at $\sqrt{s} = 13$ TeV in the $H \to \gamma\gamma$ channel using 139 fb^{-1} of pp collision data with the ATLAS experiment”. In: *JHEP* 07 (2023), p. 088. DOI: 10.1007/JHEP07(2023)088. arXiv: 2207.00348 [hep-ex].

[20] Georges Aad et al. “CP Properties of Higgs Boson Interactions with Top Quarks in the $t\bar{t}H$ and tH Processes Using $H \to \gamma\gamma$ with the ATLAS Detector”. In: *Phys. Rev. Lett.* 125.6 (2020), p. 061802. DOI: 10.1103/PhysRevLett.125.061802. arXiv: 2004.04545 [hep-ex].

[21] Albert M Sirunyan et al. “Measurements of $\mathrm{t\bar{t}}H$ Production and the CP Structure of the Yukawa Interaction between the Higgs Boson and Top Quark in the Diphoton Decay Channel”. In: *Phys. Rev. Lett.* 125.6 (2020), p. 061801. DOI: 10.1103/PhysRevLett.125.061801. arXiv: 2003.10866 [hep-ex].

[22] Georges Aad et al. “Search for dark matter in events with missing transverse momentum and a Higgs boson decaying into two photons in pp collisions at $\sqrt{s} = 13$ TeV with the ATLAS detector”. In: *JHEP* 10 (2021), p. 013. DOI: 10.1007/JHEP10(2021)013. arXiv: 2104.13240 [hep-ex].

[23] Albert M. Sirunyan et al. “Search for dark matter produced in association with a Higgs boson decaying to $\gamma\gamma$ or $\tau^+\tau^-$ at $\sqrt{s} = 13$ TeV”. In: *JHEP* 09 (2018), p. 046. DOI: 10.1007/JHEP09(2018)046. arXiv: 1806.04771 [hep-ex].

[24] Albert M. Sirunyan et al. “Search for the decay of a Higgs boson in the $\ell\ell\gamma$ channel in proton-proton collisions at $\sqrt{s} = 13$ TeV”. In: *JHEP* 11 (2018), p. 152. DOI: 10.1007/JHEP11(2018)152. arXiv: 1806.05996 [hep-ex].

[25] Georges Aad et al. "Measurements of WH and ZH production in the $H \to b\bar{b}$ decay channel in pp collisions at 13 TeV with the ATLAS detector". In: *Eur. Phys. J. C* 81.2 (2021), p. 178. DOI: 10.1140/epjc/s10052-020-08677-2. arXiv: 2007.02873 [hep-ex].

[26] Guglielmo Coloretti et al. "Searching for low-mass resonances decaying into W bosons". In: *Phys. Rev. D* 108.3 (2023), p. 035026. DOI: 10.1103/PhysRevD.108.035026. arXiv: 2302.07276 [hep-ph].

[27] Lyndon Evans and Philip Bryant. "LHC Machine". In: *Journal of Instrumentation* 3.08 (Aug. 2008), S08001. DOI: 10.1088/1748-0221/3/08/S08001. URL: https://dx.doi.org/10.1088/1748-0221/3/08/S08001.

[28] C. Burgard. *Example: Standard Model of Physics*. URL: https://texample.net/tikz/examples/model-physics/.

[29] S. Navas et al. "Review of particle physics". In: *Phys. Rev. D* 110.3 (2024), p. 030001. DOI: 10.1103/PhysRevD.110.030001.

[30] Georges Aad et al. "Observation of a new particle in the search for the Standard Model Higgs boson with the ATLAS detector at the LHC". In: *Physics Letters B* 716.1 (Sept. 2012), pp. 1–29. ISSN: 0370-2693. DOI: 10.1016/j.physletb.2012.08.020. URL: http://dx.doi.org/10.1016/j.physletb.2012.08.020.

[31] Serguei Chatrchyan et al. "Observation of a new boson at a mass of 125 GeV with the CMS experiment at the LHC". In: *Physics Letters B* 716.1 (Sept. 2012), pp. 30–61. ISSN: 0370-2693. DOI: 10.1016/j.physletb.2012.08.021. URL: http://dx.doi.org/10.1016/j.physletb.2012.08.021.

[32] F. Englert and R. Brout. "Broken Symmetry and the Mass of Gauge Vector Mesons". In: *Phys. Rev. Lett.* 13 (9 Aug. 1964), pp. 321–323. DOI: 10.1103/PhysRevLett.13.321. URL: https://link.aps.org/doi/10.1103/PhysRevLett.13.321.

[33] G. S. Guralnik, C. R. Hagen, and T. W. B. Kibble. "Global Conservation Laws and Massless Particles". In: *Phys. Rev. Lett.* 13 (20 Nov. 1964), pp. 585–587. DOI: 10.1103/PhysRevLett.13.585. URL: https://link.aps.org/doi/10.1103/PhysRevLett.13.585.

[34] Steven Weinberg. "A Model of Leptons". In: *Phys. Rev. Lett.* 19 (21 Nov. 1967), pp. 1264–1266. DOI: 10.1103/PhysRevLett.19.1264. URL: https://link.aps.org/doi/10.1103/PhysRevLett.19.1264.

[35] Leon Lederman and Dick Teresi. *The God Particle: If the Universe Is the Answer, What Is the Question?* New York: Dell Publishing, 1993. URL: https://www.crisrieder.org/thejourney/storage/2024/08/the-god-particle-if-the-universe-is-the-answer-what-is-the-question-copy-1.pdf.

[36] P.W. Higgs. "Broken symmetries, massless particles and gauge fields". In: *Physics Letters* 12.2 (1964), pp. 132–133. ISSN: 0031-9163. DOI: https://doi.org/10.1016/0031-9163(64)91136-9. URL: https://www.sciencedirect.com/science/article/pii/0031916364911369.

[37] Peter W. Higgs. "Broken Symmetries and the Masses of Gauge Bosons". In: *Phys. Rev. Lett.* 13 (16 Oct. 1964), pp. 508–509. DOI: 10.1103/PhysRevLett.13.508. URL: https://link.aps.org/doi/10.1103/PhysRevLett.13.508.

[38] P. W. Anderson. "Plasmons, Gauge Invariance, and Mass". In: *Phys. Rev.* 130 (1 Apr. 1963), pp. 439–442. DOI: 10.1103/PhysRev.130.439. URL: https://link.aps.org/doi/10.1103/PhysRev.130.439.

[39] Joshua Falco Beirer. "Novel Approaches to the Fast Simulation of the ATLAS Calorimeter and Performance Studies of Track-Assisted Reclustered Jets for Searches for Resonant $X \to SH \to b\bar{b}WW^*$ Production with the ATLAS Detector". PhD thesis. Gottingen U., 2023. DOI: 10.53846/goediss-9900.

[40] Morad Aaboud et al. "Measurement of VH, H $\to$ b$\bar{\text{b}}$ production as a function of the vector-boson transverse momentum in 13 TeV pp collisions with the ATLAS detector". In: *JHEP* 05 (2019), p. 141. DOI: 10.1007/JHEP05(2019)141. arXiv: 1903.04618 [hep-ex].

[41] Ben Allanach and Howard E. Haber. "Supersymmetry, Part I (Theory)". In: (Jan. 2024). arXiv: 2401.03827 [hep-ph].

[42] Georges Aad et al. "Higgs boson production cross-section measurements and their EFT interpretation in the 4ℓ decay channel at $\sqrt{s}$ =13 TeV with the ATLAS detector". In: *Eur. Phys. J. C* 80.10 (2020). [Erratum: Eur.Phys.J.C 81, 29 (2021), Erratum: Eur.Phys.J.C 81, 398 (2021)], p. 957. DOI: 10.1140/epjc/s10052-020-8227-9. arXiv: 2004.03447 [hep-ex].

[43] Planck Collaboration et al. “Planck 2015 results: I. Overview of products and scientific results”. In: *Astronomy & Astrophysics* 594 (2015), pp. 1–38. DOI: https://doi.org/10.1051/0004-6361/201527101.

[44] Adam G. Riess et al. “Observational Evidence from Supernovae for an Accelerating Universe and a Cosmological Constant”. In: *The Astronomical Journal* 116.3 (Sept. 1998), p. 1009. DOI: 10.1086/300499. URL: https://dx.doi.org/10.1086/300499.

[45] Andrei D Sakharov. “Violation of CP invariance, C asymmetry, and baryon asymmetry of the universe”. In: *Soviet Physics Uspekhi* 34.5 (May 1991), p. 392. DOI: 10.1070/PU1991v034n05ABEH002497. URL: https://dx.doi.org/10.1070/PU1991v034n05ABEH002497.

[46] Y. Fukuda et al. “Evidence for Oscillation of Atmospheric Neutrinos”. In: *Phys. Rev. Lett.* 81 (8 Aug. 1998), pp. 1562–1567. DOI: 10.1103/PhysRevLett.81.1562. URL: https://link.aps.org/doi/10.1103/PhysRevLett.81.1562.

[47] Q. R. Ahmad et al. “Measurement of the Rate of $\nu_e + d \rightarrow p + p + e^-$ Interactions Produced by ^8B Solar Neutrinos at the Sudbury Neutrino Observatory”. In: *Phys. Rev. Lett.* 87 (7 July 2001), p. 071301. DOI: 10.1103/PhysRevLett.87.071301. URL: https://link.aps.org/doi/10.1103/PhysRevLett.87.071301.

[48] S. Abe et al. “Precision Measurement of Neutrino Oscillation Parameters with KamLAND”. In: *Phys. Rev. Lett.* 100 (22 June 2008), p. 221803. DOI: 10.1103/PhysRevLett.100.221803. URL: https://link.aps.org/doi/10.1103/PhysRevLett.100.221803.

[49] Stephen P. Martin. “A Supersymmetry primer”. In: *Adv. Ser. Direct. High Energy Phys.* 18 (1998). Ed. by Gordon L. Kane, pp. 1–98. DOI: 10.1142/9789812839657_0001. arXiv: hep-ph/9709356.

[50] Georges Aad et al. “Measurements of fiducial and differential cross sections for Higgs boson production in the diphoton decay channel at $\sqrt{s} = 8$ TeV with ATLAS”. In: *JHEP* 09 (2014), p. 112. DOI: 10.1007/JHEP09(2014)112. arXiv: 1407.4222 [hep-ex].

[51] Georges Aad et al. "Fiducial and differential cross sections of Higgs boson production measured in the four-lepton decay channel in pp collisions at $\sqrt{s}$=8 TeV with the ATLAS detector". In: *Phys. Lett. B* 738 (2014), pp. 234–253. DOI: 10.1016/j.physletb.2014.09.054. arXiv: 1408.3226 [hep-ex].

[52] Vardan Khachatryan et al. "Measurement of differential cross sections for Higgs boson production in the diphoton decay channel in pp collisions at $\sqrt{s} = 8$ TeV". In: *Eur. Phys. J. C* 76.1 (2016), p. 13. DOI: 10.1140/epjc/s10052-015-3853-3. arXiv: 1508.07819 [hep-ex].

[53] *Measurement of inclusive and differential fiducial cross sections for Higgs boson production in the H-to-4l decay channel in p-p collisions at 7 TeV and 8 TeV*. Tech. rep. Geneva: CERN, 2015. URL: https://cds.cern.ch/record/2040210.

[54] Georges Aad et al. "Searches for Higgs boson pair production in the $hh \to bb\tau\tau, \gamma\gamma WW^*, \gamma\gamma bb, bbbb$ channels with the ATLAS detector". In: *Phys. Rev. D* 92 (2015), p. 092004. DOI: 10.1103/PhysRevD.92.092004. arXiv: 1509.04670 [hep-ex].

[55] *Search for resonant HH production in 2gamma+2b channel*. Tech. rep. Geneva: CERN, 2014. URL: https://cds.cern.ch/record/1697512.

[56] Vardan Khachatryan et al. "Searches for a heavy scalar boson H decaying to a pair of 125 GeV Higgs bosons hh or for a heavy pseudoscalar boson A decaying to Zh, in the final states with $h \to \tau\tau$". In: *Phys. Lett. B* 755 (2016), pp. 217–244. DOI: 10.1016/j.physletb.2016.01.056. arXiv: 1510.01181 [hep-ex].

[57] Vardan Khachatryan et al. "Searches for heavy Higgs bosons in two-Higgs-doublet models and for $t\bar{b}ch$ decay using multilepton and diphoton final states in pp collisions at 8 TeV". In: *Phys. Rev. D* 90 (2014), p. 112013. DOI: 10.1103/PhysRevD.90.112013. arXiv: 1410.2751 [hep-ex].

[58] Georges Aad et al. "Search for $H \to \gamma\gamma$ produced in association with top quarks and constraints on the Yukawa coupling between the top quark and the Higgs boson using data taken at 7 TeV and 8 TeV with the ATLAS detector". In: *Phys. Lett. B* 740 (2015), pp. 222–242. DOI: 10.1016/j.physletb.2014.11.049. arXiv: 1409.3122 [hep-ex].

[59] Georges Aad et al. “Search for the associated production of the Higgs boson with a top quark pair in multilepton final states with the ATLAS detector”. In: *Phys. Lett. B* 749 (2015), pp. 519–541. DOI: 10.1016/j.physletb.2015.07.079. arXiv: 1506.05988 [hep-ex].

[60] Georges Aad et al. “Search for the Standard Model Higgs boson produced in association with top quarks and decaying into $b\bar{b}$ in pp collisions at $\sqrt{s} = 8$ TeV with the ATLAS detector”. In: *Eur. Phys. J. C* 75.7 (2015), p. 349. DOI: 10.1140/epjc/s10052-015-3543-1. arXiv: 1503.05066 [hep-ex].

[61] Vardan Khachatryan et al. “Search for the associated production of the Higgs boson with a top-quark pair”. In: *JHEP* 09 (2014). [Erratum: JHEP 10, 106 (2014)], p. 087. DOI: 10.1007/JHEP09(2014)087. arXiv: 1408.1682 [hep-ex].

[62] Georges Aad et al. “Search for a high-mass Higgs boson decaying to a W boson pair in pp collisions at $\sqrt{s} = 8$ TeV with the ATLAS detector”. In: *JHEP* 01 (2016), p. 032. DOI: 10.1007/JHEP01(2016)032. arXiv: 1509.00389 [hep-ex].

[63] Georges Aad et al. “Search for an additional, heavy Higgs boson in the $H \to ZZ$ decay channel at $\sqrt{s} = 8$ TeV in pp collision data with the ATLAS detector”. In: *Eur. Phys. J. C* 76.1 (2016), p. 45. DOI: 10.1140/epjc/s10052-015-3820-z. arXiv: 1507.05930 [hep-ex].

[64] Vardan Khachatryan et al. “Search for a Higgs boson in the mass range from 145 to 1000 GeV decaying to a pair of W or Z bosons”. In: *JHEP* 10 (2015), p. 144. DOI: 10.1007/JHEP10(2015)144. arXiv: 1504.00936 [hep-ex].

[65] Andreas Crivellin et al. *Accumulating Evidence for the Associated Production of a New Higgs Boson at the Large Hadron Collider*. 2023. arXiv: 2109.02650 [hep-ph]. URL: https://arxiv.org/abs/2109.02650.

[66] Georges Aad et al. “Model-independent search for the presence of new physics in events including $H \to \gamma\gamma$ with $\sqrt{s} = 13$ TeV pp data recorded by the ATLAS detector at the LHC”. In: *JHEP* 07 (2023), p. 176. DOI: 10.1007/JHEP07(2023)176. arXiv: 2301.10486 [hep-ex].

[67] Armen Tumasyan et al. “Measurements of the Higgs boson production cross section and couplings in the W boson pair decay channel in proton-proton collisions at $\sqrt{s} = 13\,\text{TeV}$”. In: *Eur. Phys. J. C* 83.7 (2023), p. 667. DOI: 10.1140/epjc/s10052-023-11632-6. arXiv: 2206.09466 [hep-ex].

[68] Georges Aad et al. "Measurements of Higgs boson production by gluon-gluon fusion and vector-boson fusion using $H \to WW^* \to e\nu\mu\nu$ decays in pp collisions at $\sqrt{s} = 13$ TeV with the ATLAS detector". In: *Phys. Rev. D* 108 (2023), p. 032005. DOI: 10.1103/PhysRevD.108.032005. arXiv: 2207.00338 [hep-ex].

[69] Fischer et al. "Unveiling hidden physics at the LHC". In: *The European Physical Journal C* 82.8 (Aug. 2022). ISSN: 1434-6052. DOI: 10.1140/epjc/s10052-022-10541-4. URL: http://dx.doi.org/10.1140/epjc/s10052-022-10541-4.

[70] Andreas Crivellin and Bruce Mellado. "Anomalies in particle physics and their implications for physics beyond the standard model". In: *Nature Reviews Physics* 6.5 (Mar. 2024), pp. 294–309. ISSN: 2522-5820. DOI: 10.1038/s42254-024-00703-6. URL: http://dx.doi.org/10.1038/s42254-024-00703-6.

[71] Sumit Banik et al. *Uncovering New Higgses in the LHC Analyses of Differential $t\bar{t}$ Cross Sections*. 2025. arXiv: 2308.07953 [hep-ph]. URL: https://arxiv.org/abs/2308.07953.

[72] Georges Aad et al. "Search for non-resonant Higgs boson pair production in final states with leptons, taus, and photons in pp collisions at $\sqrt{s} = 13$ TeV with the ATLAS detector". In: *JHEP* 08 (2024), p. 164. DOI: 10.1007/JHEP08(2024)164. arXiv: 2405.20040 [hep-ex].

[73] *Measurement of the properties of Higgs boson production at $\sqrt{s}$=13 TeV in the $H \to \gamma\gamma$ channel using 139 fb^1 of pp collision data with the ATLAS experiment*. Tech. rep. All figures including auxiliary figures are available at https://atlas.web.cern.ch/Atlas/GROUPS/PHYSICS/CONFNOTES/ATLAS-CONF-2020-026. Geneva: CERN, 2020. URL: https://cds.cern.ch/record/2725727.

[74] Georges Aad et al. "Search for Higgs boson pair production in the two bottom quarks plus two photons final state in pp collisions at $\sqrt{s} = 13$ TeV with the ATLAS detector". In: *Phys. Rev. D* 106.5 (2022), p. 052001. DOI: 10.1103/PhysRevD.106.052001. arXiv: 2112.11876 [hep-ex].

[75] Armen Tumasyan et al. "Search for Higgs boson decays to a Z boson and a photon in proton-proton collisions at $\sqrt{s} = 13$ TeV". In: *JHEP* 05 (2023), p. 233. DOI: 10.1007/JHEP05(2023)233. arXiv: 2204.12945 [hep-ex].

[76] Georges Aad et al. "Search for direct stau production in events with two hadronic τ-leptons in $\sqrt{s} = 13$ TeV pp collisions with the ATLAS detector". In: *Phys. Rev. D* 101.3 (2020), p. 032009. DOI: 10.1103/PhysRevD.101.032009. arXiv: 1911.06660 [hep-ex].

[77] Albert M Sirunyan et al. "Search for direct pair production of supersymmetric partners to the τ lepton in proton-proton collisions at $\sqrt{s} = 13$ TeV". In: *Eur. Phys. J. C* 80.3 (2020), p. 189. DOI: 10.1140/epjc/s10052-020-7739-7. arXiv: 1907.13179 [hep-ex].

[78] Armen Tumasyan et al. "Search for direct pair production of supersymmetric partners of τ leptons in the final state with two hadronically decaying τ leptons and missing transverse momentum in proton-proton collisions at $\sqrt{s} = 13$ TeV". In: *Phys. Rev. D* 108.1 (2023), p. 012011. DOI: 10.1103/PhysRevD.108.012011. arXiv: 2207.02254 [hep-ex].

[79] Georges Aad et al. "Search for electroweak production of supersymmetric particles in final states with two τ-leptons in $\sqrt{s} = 13$ TeV pp collisions with the ATLAS detector". In: *JHEP* 05 (2024), p. 150. DOI: 10.1007/JHEP05(2024)150. arXiv: 2402.00603 [hep-ex].

[80] R. L. Workman et al. Particle Data Group Collaboration. "Review of Particle Physics". In: *Progress of Theoretical and Experimental Physics* 2022.8 (Aug. 2022), p. 083C01. DOI: 10.1093/ptep/ptac097. URL: https://doi.org/10.1093/ptep/ptac097.

[81] Yu Cheng et al. "Electroweak precision tests for triplet scalars". In: *Nucl. Phys. B* 989 (2023), p. 116118. DOI: 10.1016/j.nuclphysb.2023.116118. arXiv: 2208.06760 [hep-ph].

[82] Pavel Fileviez Perez et al. "Triplet Scalars and Dark Matter at the LHC". In: *Phys. Rev. D* 79 (2009), p. 055024. DOI: 10.1103/PhysRevD.79.055024. arXiv: 0811.3957 [hep-ph].

[83] Shinya Kanemura and Kei Yagyu. "Radiative corrections to electroweak parameters in the Higgs triplet model and implication with the recent Higgs boson searches". In: *Phys. Rev. D* 85 (2012), p. 115009. DOI: 10.1103/PhysRevD.85.115009. arXiv: 1201.6287 [hep-ph].

[84] Saiyad Ashanujjaman et al. “Searching for a Charged Higgs Boson in Top-Quark Decays via the WZ Mode”. In: (Sept. 2025). arXiv: 2509.07094 [hep-ph].

[85] K Aamodt et al. “The ALICE experiment at the CERN LHC”. In: *JINST* 3 (2008). Also published by CERN Geneva in 2010, S08002. DOI: 10.1088/1748-0221/3/08/S08002. URL: https://cds.cern.ch/record/1129812.

[86] The LHCb Collaboration. “The LHCb Detector at the LHC”. In: *Journal of Instrumentation* 3.08 (Aug. 2008), S08005. DOI: 10.1088/1748-0221/3/08/S08005. URL: https://dx.doi.org/10.1088/1748-0221/3/08/S08005.

[87] Ewa Lopienska. “The CERN accelerator complex, layout in 2022”. In: (2022). General Photo. URL: https://cds.cern.ch/record/2800984.

[88] ATLAS Collaboration. *Luminosity Public Results for Run 3*. https://twiki.cern.ch/twiki/bin/view/AtlasPublic/LuminosityPublicResultsRun3. Accessed: 2025-04-05. 2025.

[89] O. Aberle et al. *High-Luminosity Large Hadron Collider (HL-LHC): Technical design report*. CERN Yellow Reports: Monographs. Geneva: CERN, 2020. DOI: 10.23731/CYRM-2020-0010. URL: https://cds.cern.ch/record/2749422.

[90] Georges Aad et al. “The ATLAS experiment at the CERN Large Hadron Collider: a description of the detector configuration for Run 3”. In: *JINST* 19.20 (2024), P05063. DOI: 10.1088/1748-0221/19/05/P05063. arXiv: 2305.16623 [physics.ins-det].

[91] Izaak Neutelings. *CMS Coordinate System*. https://tikz.net/axis3d_cms/. https://tikz.net/axis3d_cms/. 2017.

[92] *ATLAS inner detector*. Technical design report. ATLAS. Geneva: CERN, 1997. URL: https://cds.cern.ch/record/331063.

[93] S Haywood et al. *ATLAS inner detector*. Technical design report. ATLAS. Geneva: CERN, 1997. URL: https://cds.cern.ch/record/331064.

[94] *Technical Design Report for the ATLAS Inner Tracker Strip Detector*. Tech. rep. Geneva: CERN, 2017. URL: https://cds.cern.ch/record/2257755.

[95] *Technical Design Report for the ATLAS Inner Tracker Pixel Detector*. Tech. rep. Geneva: CERN, 2017. DOI: 10.17181/CERN.FOZZ.ZP3Q. URL: https://cds.cern.ch/record/2285585.

[96] A. Abdesselam et al. “The ATLAS semiconductor tracker end-cap module”. In: *Nucl. Instrum. Meth. A* 575 (2007), pp. 353–389. DOI: 10.1016/j.nima.2007.02.019.

[97] A. Abdesselam et al. “The barrel modules of the ATLAS semiconductor tracker”. In: *Nucl. Instrum. Meth. A* 568 (2006), pp. 642–671. DOI: 10.1016/j.nima.2006.08.036.

[98] A. Ahmad et al. “The Silicon microstrip sensors of the ATLAS semiconductor tracker”. In: *Nucl. Instrum. Meth. A* 578 (2007), pp. 98–118. DOI: 10.1016/j.nima.2007.04.157.

[99] E. Abat et al. “The ATLAS TRT barrel detector”. In: *JINST* 3 (2008), P02014. DOI: 10.1088/1748-0221/3/02/P02014.

[100] E. Abat et al. “The ATLAS TRT end-cap detectors”. In: *JINST* 3 (2008), P10003. DOI: 10.1088/1748-0221/3/10/P10003.

[101] E. Abat et al. “The ATLAS Transition Radiation Tracker (TRT) proportional drift tube: Design and performance”. In: *JINST* 3 (2008), P02013. DOI: 10.1088/1748-0221/3/02/P02013.

[102] *ATLAS tile calorimeter*. Technical design report. ATLAS. Geneva: CERN, 1996. DOI: 10.17181/CERN.JRBJ.7028. URL: https://cds.cern.ch/record/331062.

[103] *ATLAS muon spectrometer*. Technical design report. ATLAS. Geneva: CERN, 1997. URL: https://cds.cern.ch/record/331068.

[104] T Kawamoto et al. *New Small Wheel Technical Design Report*. Tech. rep. ATLAS New Small Wheel Technical Design Report. 2013. URL: https://cds.cern.ch/record/1552862.

[105] L. Martinelli. “ATLAS New Small Wheel performance studies after first year of operation”. In: *Nucl. Instrum. Meth. A* 1063 (2024), p. 169290. DOI: 10.1016/j.nima.2024.169290.

[106] L Adamczyk et al. *Technical Design Report for the ATLAS Forward Proton Detector*. Tech. rep. 2015. URL: https://cds.cern.ch/record/2017378.

[107] Georges Aad et al. “Luminosity Determination in pp Collisions at $\sqrt{s} = 7$ TeV Using the ATLAS Detector at the LHC”. In: *Eur. Phys. J. C* 71 (2011), p. 1630. DOI: 10.1140/epjc/s10052-011-1630-5. arXiv: 1101.2185 [hep-ex].

[108] Stefan Ask. “Status of the Forward Physics Projects in ATLAS”. In: *15th International Workshop on Deep-Inelastic Scattering and Related Subjects*. June 2007, pp. 747–750. DOI: 10.3204/proc07-01/131. arXiv: 0706.0644 [hep-ex].

[109] The ATLAS collaboration. “Operation of the ATLAS trigger system in Run 2”. In: *Journal of Instrumentation* 15.10 (Oct. 2020), P10004. DOI: 10.1088/1748-0221/15/10/P10004. URL: https://dx.doi.org/10.1088/1748-0221/15/10/P10004.

[110] Deepak Kar. *Experimental Particle Physics: Understanding the Measurements and Searches at the Large Hadron Collider*. IOP Expanding Physics. Bristol: IOP Publishing, 2019. URL: https://cds.cern.ch/record/2683715.

[111] C. N. Yang and R. L. Mills. “Conservation of Isotopic Spin and Isotopic Gauge Invariance”. In: *Phys. Rev.* 96 (1 Oct. 1954), pp. 191–195. DOI: 10.1103/PhysRev.96.191. URL: https://link.aps.org/doi/10.1103/PhysRev.96.191.

[112] ATLAS Collaboration. *TrigEgamma Recommendations Run 3*. https://twiki.cern.ch/twiki/bin/view/Atlas/TrigEgammaRecommendationsRun3. 2023.

[113] *Identification of hadronic tau lepton decays using neural networks in the ATLAS experiment*. Tech. rep. Geneva: CERN, 2019. URL: https://cds.cern.ch/record/2688062.

[114] Georges Aad et al. “Identification and energy calibration of hadronically decaying tau leptons with the ATLAS experiment in pp collisions at $\sqrt{s}$=8 TeV”. In: *Eur. Phys. J. C* 75 (2015), p. 303. DOI: 10.1140/epjc/s10052-015-3500-z. arXiv: 1412.7086. URL: https://cds.cern.ch/record/1978197.

[115] Georges Aad et al. “Muon reconstruction performance of the ATLAS detector in proton–proton collision data at $\sqrt{s}$ =13 TeV”. In: *Eur. Phys. J. C* 76.5 (2016), p. 292. DOI: 10.1140/epjc/s10052-016-4120-y. arXiv: 1603.05598 [hep-ex].

[116] Matteo Cacciari, Gavin P. Salam, and Gregory Soyez. "The anti-k_t jet clustering algorithm". In: *JHEP* 04 (2008), p. 063. DOI: 10.1088/1126-6708/2008/04/063. arXiv: 0802.1189 [hep-ph].

[117] Georges Aad et al. "Topological cell clustering in the ATLAS calorimeters and its performance in LHC Run 1". In: *Eur. Phys. J. C* 77 (2017), p. 490. DOI: 10.1140/epjc/s10052-017-5004-5. arXiv: 1603.02934 [hep-ex].

[118] Georges Aad et al. "Performance of pile-up mitigation techniques for jets in pp collisions at $\sqrt{s} = 8$ TeV using the ATLAS detector". In: *Eur. Phys. J. C* 76 (2016), p. 581. DOI: 10.1140/epjc/s10052-016-4395-z. arXiv: 1510.03823. URL: https://cds.cern.ch/record/2058295.

[119] ATLAS collaboration et al. *Selection of jets produced in 13TeV proton-proton collisions with the ATLAS detector*. Tech. rep. Geneva: CERN, 2015. URL: https://cds.cern.ch/record/2037702.

[120] Georges Aad et al. "ATLAS b-jet identification performance and efficiency measurement with $t\bar{t}$ events in pp collisions at $\sqrt{s} = 13$ TeV". In: *Eur. Phys. J. C* 79.11 (2019), p. 970. DOI: 10.1140/epjc/s10052-019-7450-8. arXiv: 1907.05120 [hep-ex].

[121] Morad Aaboud et al. "Performance of missing transverse momentum reconstruction with the ATLAS detector using proton-proton collisions at $\sqrt{s} = 13$ TeV". In: *Eur. Phys. J. C* 78.11 (2018), p. 903. DOI: 10.1140/epjc/s10052-018-6288-9. arXiv: 1802.08168 [hep-ex].

[122] J. Alwall et al. "The automated computation of tree-level and next-to-leading order differential cross sections, and their matching to parton shower simulations". In: *JHEP* 07 (2014), p. 079. DOI: 10.1007/JHEP07(2014)079. arXiv: 1405.0301 [hep-ph].

[123] Richard D. Ball et al. "Parton distributions with LHC data". In: *Nucl. Phys. B* 867 (2013), pp. 244–289. DOI: 10.1016/j.nuclphysb.2012.10.003. arXiv: 1207.1303 [hep-ph].

[124] Enrico Bothmann et al. "Event Generation with Sherpa 2.2". In: *SciPost Phys.* 7.3 (2019), p. 034. DOI: 10.21468/SciPostPhys.7.3.034. arXiv: 1905.09127 [hep-ph].

[125] Richard D. Ball et al. "Parton distributions for the LHC Run II". In: *JHEP* 04 (2015), p. 040. DOI: 10.1007/JHEP04(2015)040. arXiv: 1410.8849 [hep-ph].

[126] Cerda Alberich et al. *Supporting note: Selection and performance for the H→ and H→Z analyses*. Tech. rep. Geneva: CERN, 2016. URL: https://cds.cern.ch/record/2196102.

[127] Georges Aad et al. "Combined Measurement of the Higgs Boson Mass in pp Collisions at $\sqrt{s} = 7$ and 8 TeV with the ATLAS and CMS Experiments". In: *Phys. Rev. Lett.* 114 (2015), p. 191803. DOI: 10.1103/PhysRevLett.114.191803. arXiv: 1503.07589 [hep-ex].

[128] ATLAS Collaboration. "Measurement of the Higgs boson mass in the $H \to ZZ^* \to 4\ell$ and $H \to \gamma\gamma$ channels with $\sqrt{s} = 13$ TeV pp collisions using the ATLAS detector". In: *Physics Letters B* 784 (2018), pp. 345–366. ISSN: 0370-2693. DOI: 10.1016/j.physletb.2018.07.050. URL: https://www.sciencedirect.com/science/article/pii/S0370269318305884.

[129] CMS Collaboration. "Measurements of properties of the Higgs boson decaying into the four-lepton final state in pp collisions at $\sqrt{s} = 13$ TeV". In: *Journal of High Energy Physics* 2017.11 (Nov. 2017), p. 47. ISSN: 1029-8479. DOI: 10.1007/JHEP11(2017)047. URL: https://doi.org/10.1007/JHEP11(2017)047.

[130] Albert M Sirunyan et al. "A measurement of the Higgs boson mass in the diphoton decay channel". In: *Phys. Lett. B* 805 (2020), p. 135425. DOI: 10.1016/j.physletb.2020.135425. arXiv: 2002.06398 [hep-ex].

[131] D. de Florian and C. Grojean and F. Maltoni and C. Mariotti and A. Nikitenko and M. Pieri and P. Savard and M. Schumacher and R. Aggleton and M. Ahmad and others. *CERN Yellow Reports: Monographs, Vol. 2 (2017) — Handbook of LHC Higgs Cross Sections: 4. Deciphering the Nature of the Higgs Sector*. Vol. 2. CERN Yellow Reports: Monographs. CERN, 2017. DOI: 10.23731/CYRM-2017-002. URL: https://doi.org/10.23731/CYRM-2017-002.

[132] M. Aaboud et al. "Searches for the $Z\gamma$ decay mode of the Higgs boson and for new high-mass resonances in pp collisions at $\sqrt{s} = 13$ TeV with the ATLAS detector". In: *JHEP* 10 (2017), p. 112. DOI: 10.1007/JHEP10(2017)112. arXiv: 1708.00212 [hep-ex].

[133] CMS Collaboration. "Search for the decay of a Higgs boson in the $\ell\ell\gamma$ channel in proton-proton collisions at $\sqrt{s} = 13$ TeV". In: *Journal of High Energy Physics* 2018.11 (2018). DOI: 10.1007/JHEP11(2018)152. URL: https://doi.org/10.1007/JHEP11(2018)152.

[134] Ilaria Brivio and Michael Trott. "The Standard Model as an Effective Field Theory". In: *Phys. Rept.* 793 (2019), pp. 1–98. DOI: 10.1016/j.physrep.2018.11.002. arXiv: 1706.08945 [hep-ph].

[135] Sally Dawson and Pier Paolo Giardino. "Higgs decays to ZZ and $Z\gamma$ in the standard model effective field theory: An NLO analysis". In: *Phys. Rev. D* 97.9 (2018), p. 093003. DOI: 10.1103/PhysRevD.97.093003. arXiv: 1801.01136 [hep-ph].

[136] J. Elias-Miro et al. "Higgs windows to new physics through d=6 operators: constraints and one-loop anomalous dimensions". In: *JHEP* 11 (2013), p. 066. DOI: 10.1007/JHEP11(2013)066. arXiv: 1308.1879 [hep-ph].

[137] Rodrigo Alonso et al. "Renormalization Group Evolution of the Standard Model Dimension Six Operators III: Gauge Coupling Dependence and Phenomenology". In: *JHEP* 04 (2014), p. 159. DOI: 10.1007/JHEP04(2014)159. arXiv: 1312.2014 [hep-ph].

[138] A. Dedes et al. "The decay $h \to \gamma\gamma$ in the Standard-Model Effective Field Theory". In: *JHEP* 08 (2018), p. 103. DOI: 10.1007/JHEP08(2018)103. arXiv: 1805.00302 [hep-ph].

[139] A. Dedes, K. Suxho, and L. Trifyllis. "The decay $h \to Z\gamma$ in the Standard-Model Effective Field Theory". In: *JHEP* 06 (2019), p. 115. DOI: 10.1007/JHEP06(2019)115. arXiv: 1903.12046 [hep-ph].

[140] Sébastien Descotes-Genon et al. "The CKM parameters in the SMEFT". In: *JHEP* 05 (2019), p. 172. DOI: 10.1007/JHEP05(2019)172. arXiv: 1812.08163 [hep-ph].

[141] Supratim Das Bakshi et al. "Relevance of one-loop SMEFT matching in the 2HDM". In: *Phys. Rev. D* 109.7 (2024), p. 075022. DOI: 10.1103/PhysRevD.109.075022. arXiv: 2401.12279 [hep-ph].

[142] *The Pythia 8 A3 tune description of ATLAS minimum bias and inelastic measurements incorporating the Donnachie-Landshoff diffractive model*. Tech. rep. Geneva: CERN, 2016. URL: https://cds.cern.ch/record/2206965.

[143] J. de Favereau et al. "DELPHES 3, A modular framework for fast simulation of a generic collider experiment". In: *JHEP* 02 (2014), p. 057. DOI: 10.1007/JHEP02(2014)057. arXiv: 1307.6346 [hep-ex].

[144] Adam Alloul et al. "FeynRules 2.0 - A complete toolbox for tree-level phenomenology". In: *Comput. Phys. Commun.* 185 (2014), pp. 2250–2300. DOI: 10.1016/j.cpc.2014.04.012. arXiv: 1310.1921 [hep-ph].

[145] D. de Florian et al. "Handbook of LHC Higgs Cross Sections: 4. Deciphering the Nature of the Higgs Sector". In: *CERN Yellow Rep. Monogr.* 2 (2017), pp. 1–869. DOI: 10.23731/CYRM-2017-002. arXiv: 1610.07922 [hep-ph].

[146] Charalampos Anastasiou et al. "Higgs Boson Gluon-Fusion Production in QCD at Three Loops". In: *Phys. Rev. Lett.* 114 (21 May 2015), p. 212001. DOI: 10.1103/PhysRevLett.114.212001. URL: https://link.aps.org/doi/10.1103/PhysRevLett.114.212001.

[147] Charalampos Anastasiou et al. "High precision determination of the gluon fusion Higgs boson cross-section at the LHC". In: *JHEP* 05 (2016), p. 058. DOI: 10.1007/JHEP05(2016)058. arXiv: 1602.00695 [hep-ph].

[148] Falko Dulat, Achilleas Lazopoulos, and Bernhard Mistlberger. "iHixs 2 — Inclusive Higgs cross sections". In: *Comput. Phys. Commun.* 233 (2018), pp. 243–260. DOI: 10.1016/j.cpc.2018.06.025. arXiv: 1802.00827 [hep-ph].

[149] Robert V. Harlander and Kemal J. Ozeren. "Finite top mass effects for hadronic Higgs production at next-to-next-to-leading order". In: *JHEP* 11 (2009), p. 088. DOI: 10.1088/1126-6708/2009/11/088. arXiv: 0909.3420 [hep-ph].

[150] M. Ciccolini, Ansgar Denner, and S. Dittmaier. "Strong and electroweak corrections to the production of Higgs + 2jets via weak interactions at the LHC". In: *Phys. Rev. Lett.* 99 (2007), p. 161803. DOI: 10.1103/PhysRevLett.99.161803. arXiv: 0707.0381 [hep-ph].

[151] A. Djouadi, J. Kalinowski, and M. Spira. "HDECAY: A Program for Higgs boson decays in the standard model and its supersymmetric extension". In: *Comput. Phys. Commun.* 108 (1998), pp. 56–74. DOI: 10.1016/S0010-4655(97)00123-9. arXiv: hep-ph/9704448.

[152] Michael Spira. "QCD effects in Higgs physics". In: *Fortsch. Phys.* 46 (1998), pp. 203–284. DOI: 10.1002/(SICI)1521-3978(199804)46:3<203::AID-PROP203>3.0.CO;2-4. arXiv: hep-ph/9705337.

[153] Rafiqul Rahaman. "On two-body and three-body spin correlations in leptonic $t\bar{t}Z$ production and anomalous couplings at the LHC". In: *JHEP* 02 (2023), p. 077. DOI: 10.1007/JHEP02(2023)077. arXiv: 2204.12152 [hep-ph].

[154] Karabo Mosala et al. "Axion-like particles at future e^-p collider". In: *Eur. Phys. J. C* 84.1 (2024), p. 44. DOI: 10.1140/epjc/s10052-024-12401-9. arXiv: 2307.00394 [hep-ph].

[155] Rafiqul Rahaman and Ritesh K. Singh. "Unravelling the anomalous gauge boson couplings in $ZW^{\pm}$ production at the LHC and the role of spin-1 polarizations". In: *JHEP* 04 (2020), p. 075. DOI: 10.1007/JHEP04(2020)075. arXiv: 1911.03111 [hep-ph].

[156] Baptiste Ravina, Ethan Simpson, and James Howarth. "Observing $t\bar{t}Z$ spin correlations at the LHC". In: *Eur. Phys. J. C* 81.9 (2021), p. 809. DOI: 10.1140/epjc/s10052-021-09605-8. arXiv: 2106.09690 [hep-ph].

[157] Antony Lewis. "GetDist: a Python package for analysing Monte Carlo samples". In: (Oct. 2019). arXiv: 1910.13970 [astro-ph.IM].

[158] Pierre Baldi, Peter Sadowski, and Daniel Whiteson. "Searching for Exotic Particles in High-Energy Physics with Deep Learning". In: *Nature Commun.* 5 (2014), p. 4308. DOI: 10.1038/ncomms5308. arXiv: 1402.4735 [hep-ph].

[159] Ernesto Arganda et al. "A method for approximating optimal statistical significances with machine-learned likelihoods". In: *Eur. Phys. J. C* 82.11 (2022), p. 993. DOI: 10.1140/epjc/s10052-022-10944-3. arXiv: 2205.05952 [hep-ph].

[160] Ernesto Arganda et al. "Imposing exclusion limits on new physics with machine-learned likelihoods". In: *PoS* ICHEP2022 (2022), p. 1226. DOI: 10.22323/1.414.1226.

[161] JooSeuk Kim and Clayton D. Scott. *Robust Kernel Density Estimation*. 2011. arXiv: 1107.3133 [stat.ML]. URL: https://arxiv.org/abs/1107.3133.

[162] Abien Fred Agarap. "Deep Learning using Rectified Linear Units (ReLU)". In: (Mar. 2018). arXiv: 1803.08375 [cs.NE].

[163] Diederik P. Kingma and Jimmy Ba. "Adam: A Method for Stochastic Optimization". In: Dec. 2014. arXiv: 1412.6980 [cs.LG].

[164] Anqi Mao, Mehryar Mohri, and Yutao Zhong. *Cross-Entropy Loss Functions: Theoretical Analysis and Applications*. 2023. arXiv: 2304.07288 [cs.LG]. URL: https://arxiv.org/abs/2304.07288.